MSc Thesis Applied Mathematics

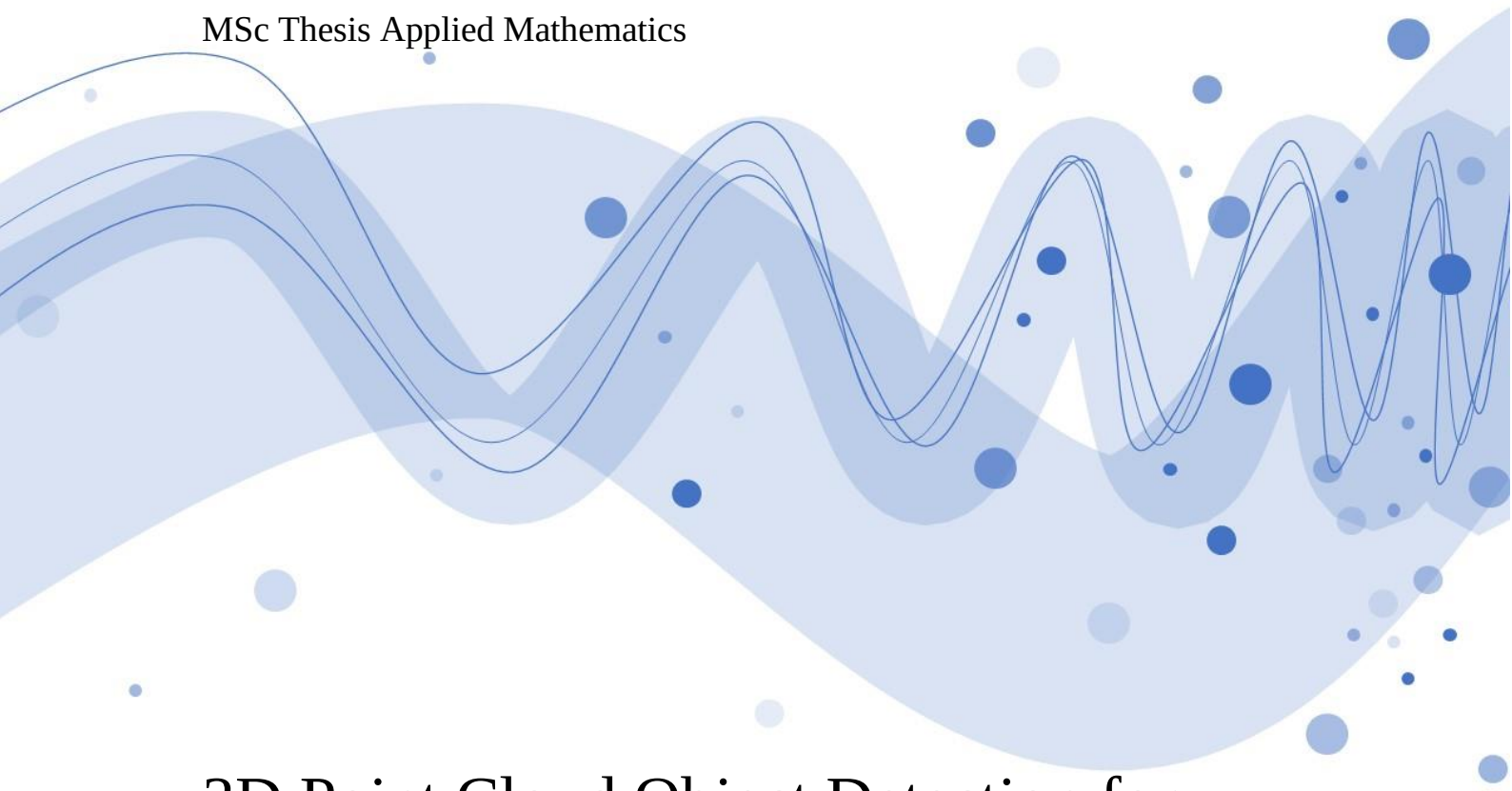

3D Point Cloud Object Detection for Millimeter Wave Radar: a Synthesis Study

I.G. van de Zande

September 2023

Graduation Committee:
Prof.dr. C. Brune (UT)
Dr. M. Guo (UT)
Dr. H. Hang (UT)
Dr. F.T. Markus (Nedap Healthcare)

Systems, Analysis and Computational Sciences
Faculty of Electrical Engineering, Mathematics and Computer Science

nedap

UNIVERSITY OF TWENTE.

Abstract

FMCW mmWave radar has suitable characteristics to monitor patients at home in an unobtrusive way. However, difficulties are encountered for 3D point cloud generation due to limited detection performance for crowded realistic indoor environments such as living rooms. Therefore the detection process needs to become more robust. This thesis provides a complete overview of the CFAR object detection method, including the steps and theory behind them. The interdependent relation of computation of the scaling factor with other steps is also clarified. Additionally, an implementation has been developed from radar signal to point cloud, including signal processing, object detection, and a proposed informatively improved post-processing step. Furthermore, to demonstrate the performance of the different interference estimators of the CFAR method for various realistic situations, an experiment has been designed and conducted.

Keywords: MmWave radar, FMCW, Signal processing, CFAR object detection, 3D point clouds, Scaling factor.

Contents

Notation List

Tx	transmitter antenna
Rx	receiver antenna
IF	intermediate frequency
$s(t)$	electromagnetic wave signal
t	time
τ	time delay
f	frequency
S	slope of a chirp
B	bandwidth of a chirp
T_c	time duration of a chirp
ϕ	phase shift
R	range
c	speed of light
λ	wavelength
v	velocity
θ	azimuth incident angle
ψ	elevation incident angle
d	distance between two aligned antennas
CUT	cell under test
X_i	training cell
Z	estimated interference level
P_D	probability of detection
P_{FA}	probability of false alarm
α	scaling factor
γ	threshold
N_C	number of chirps
N_S	number of samples
n_G	number of guard cells
n_T	number of training cells

1 Introduction

In this chapter the motivation for this research is explained in section 1.1, including why there is a need for monitoring (elderly) patients at home and how mmWave radar is a suitable technology that can be used. Section 1.2 gives an overview on the current use of mmWave radar and novel research in different fields. The principles of radar technology including how information is retrieved, is explained in section 1.3, and in section 1.4 are the research goals and objectives formulated. This introductory chapter ends with section 1.5, with an outline of the entire thesis and an overview of the contributions.

1.1 Motivation

According to the report from December 2022 by the *Inspectie Gezondheidszorg en Jeugd* (Inspection Healthcare and Youth) of the Ministry of Health, Welfare and Sports, there is a shortage on the labour market in the healthcare sector in the Netherlands [31]. Healthcare organisations are encouraged by the inspection to investigate the possibilities of applying innovative technologies to increase independence of patients and simultaneously decrease the work pressure for the personnel. MmWave radar is a suitable technology for this and can be used for monitoring purposes. That is because by processing echo signals to detect distance, angle and velocity, both large and small movements are detected. This means a person can be localised and tracked [28, 83], but also activities, gestures and even vital signs can be recognized [54, 77].

Camera-based motion monitoring systems have been popular for similar purposes, but they require strict placement settings, lighting, and raise privacy concerns. MmWave radar on the other hand is privacy preserving because personal features cannot be directly distinguished from the signals. Next to that, the radar can be located somewhere on the ceiling similar to a fire alarm. Furthermore it does not contain a camera lens which needs to be placed in direct sight, but antennas that cover at most a few centimeters of surface and can even be placed behind a cover. This unobtrusive and non-invasive way of monitoring is beneficial for the patient comfort.

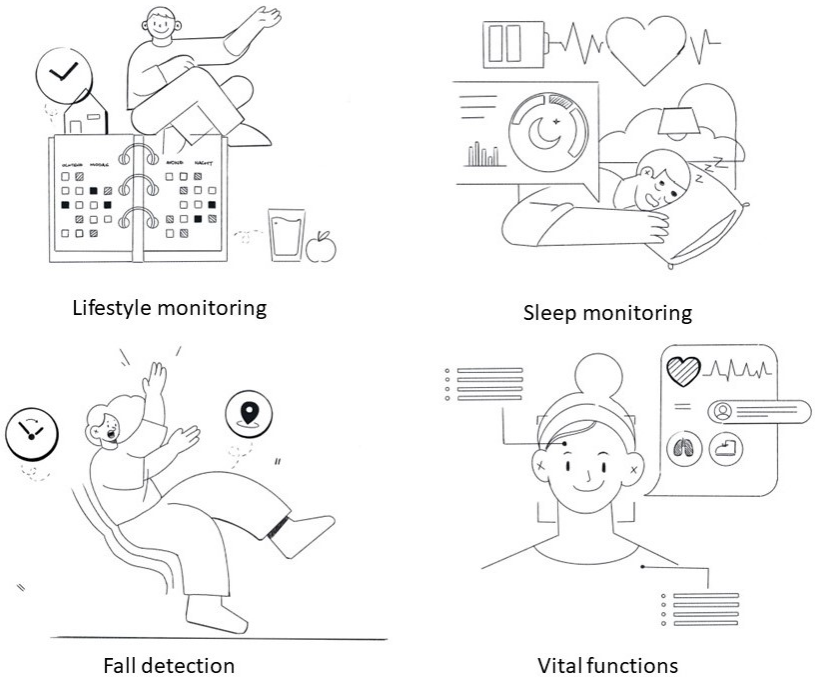

Figure 1: Possible applications of mmWave radar in the healthcare sector [13]

There are multiple applications for which mmWave radar could serve, that are beneficial for both patients and caregivers. An overview of possible applications can be seen in Figure 1. First of all, a person's lifestyle including daily routines, but also irregular behaviour can be monitored. Knowing if the patient is having an afternoon nap, or if visitors are present, is useful information for the caregiver to, for instance, change the route of their rounds. A patient who often forgets dinner can now be effectively reminded by their

caregiver. Likewise, insights in the pattern, activity and quality of the sleep can lead to actions to improve the patients wellbeing, such as turning a patient in their bed to prevent pressure sores. A clearer and more complete picture of the patient's daily routine is provided at distance.

Moreover, safety is increased for particularly the elderly patients. They have an increased risk of falling, and incidents often result in severe physical and psychological consequences [79]. Falls can be detected and directly alarm caregivers, which decreases the risk of a patient being in an immobile situation for quite some time till the next routine check-up. Next to that, monitoring the gait and balance can be used to assess which patients are at higher risk of falling [76], such that caregivers can keep an extra eye on these patients to prevent possible incidents.

Additionally, vital signs of patients such as heart and respiratory rate can also be monitored remotely without the need for physical contact with a device [80, 2]. This can give insight into whether a patient has been deteriorating rapidly and if adapted care is needed, while no additional action from a caregiver is required and thus saves time. This can also be helpful for patients who have difficulty with articulating their stress or need for help.

These examples give a clear view of the advantages of mmWave radar, and which improvements it can bring for patient monitoring. For the patients this results in, but is not limited to, increased patient comfort by adjusting the caregiver's visits to the patient's daily routines and decreased waiting time for immediate care. While for the caregiver mmWave radar monitoring can contribute to better insights into the patients wellbeing and a decrease in number of routine checks and hence decreased travel time. This may result in an increase in time available for each patient, and thus increasing the quality of the care provided which is again beneficial for the patient as well.

1.2 Current MmWave Applications

Radar technology in general was originally developed for military purposes, namely to detect enemy aircrafts during the second world war [50]. Since then research on radar has continued within this field, resulting into mmWave radar technology now being used in multiple ways for military purposes. For instance as a seeker in smart weapons, and precision-guided munition to search, detect, classify, and even guide missiles toward their targets [11]. For these applications the accuracy, reliability, and real-time signal processing and operation are very important. Additionally, the U.S. Army has implemented mmWave radar for intruder detection because of its localisation and tracking capabilities [1].

Next to the military field, mmWave radar is widely applied in the automotive industry, because of its small-size, and weather-independent advantages [34]. For example in adaptive cruise control and collision avoidance systems to detect nearby vehicles [72, 36, 53]. MmWave is low-cost compared to the expensive alternative LiDAR sensors, which are also frequently used in this industry [42]. LiDAR technology determines distance by emitting laser pulses and evaluating their received reflections, this results in more dense data representations than those of mmWave radar [3]. These data presentations are called point clouds, and for both sensors are shown in Figure 2. The past years research is performed on increasing the density of the radar point clouds[46, 3], often interpolation is used to increase the amount of data points [35, 10].

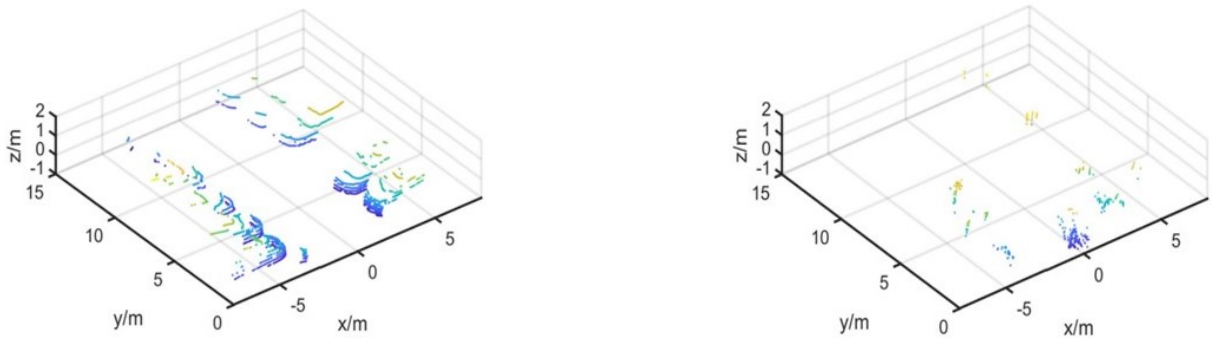

(a) LiDAR point cloud

(b) Radar point cloud

Figure 2: LiDAR and radar point clouds of a parking lot [10]

Radar is often favoured over optical sensors because the performance does not degrade as much in certain

weather situations such as heavy rain and fog [23]. Even occlusions such as smoke do not form an obstacle for radar, therefore research is also done on indoor mapping for firefighters to find their way in buildings when heavy smoke is present [24, 57].

Another research field where mmWave is active, is movement and activity recognition [73, 82]. Including for instance large movements such as tracking people [83], but also smaller ones such as gesture recognition for human-computer interaction [52, 54]. MmWave measurements focused on gait patterns of people can even extract indicators for early stage cognitive disorders [79]. Even smaller movements like the heartbeat and breathing rate of people can also be detected, which remains difficult for optical sensors [2, 56].

1.3 Background Information

When an mmWave radar has been purchased, it does not mean it can be directly used. The output from the radar needs to undergo specific steps before it can be used for actual applications. First, the spatial and velocity information is retrieved by processing the signals, than a point cloud is formed using object detection algorithms. These steps are shown in Figure 3, and form the basis of radar processing.

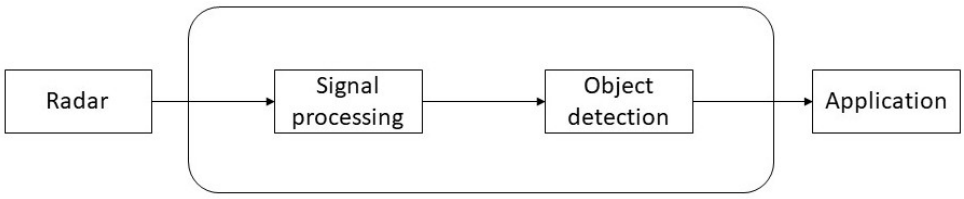

Figure 3: Information processing flow from radar to applications

1.3.1 Frequency Modulated Continuous Wave Radar

Radar technology uses electromagnetic waves and their reflected echo signal to provide information on the range between an object and the radar itself. Mmwave radar operates in the frequency range of 30 GHz to 300 GHz, which is a higher frequency range than traditional systems. The frequency of electromagnetic waves is inversely proportional to its wavelength, which means that the frequency of mmWave radar sensors corresponds with a short wavelength of in this case 1-10 millimeters [44]. Because of these smaller wavelengths the size of the radar itself can remain small and accurate range measurements of millimeters can be reached. This increased accuracy comes at the cost of a decrease in maximum distance, which for common naval radars is around 400 km [4]. Dependent on the frequency range of the signal and its transmit power, the maximum detection distance for mmWave radar ranges from a few meters to 200 meters [44].

Radars can be categorized by transmitting their signal as multiple individual pulses, or as a continuous wave. A subtype of mmWave radar is Frequency Modulated Continuous Wave (FMCW) radar, a continuous wave whose frequency changes during transmitting. Repeatedly the signal increases linearly over a pre-determined frequency bandwidth, which results in a saw-tooth representation which is called a chirp and can be seen in figures 4 and 5. Chirps are transmitted by a transmitter antenna Tx and reflected signals are perceived by receiver antennas Rx. One mmWave radar can have multiple transmitter and receiver antennas.

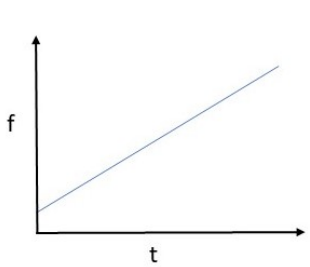

(a) Frequency as function of time

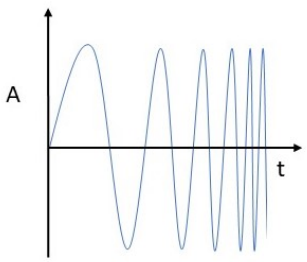

(b) Amplitude as function of time

Figure 4: Chirp signal

The transmitted frequency modulated signal is an electromagnetic wave and represented as [32, 62]

$$s_{Tx}(t) = e^{i\pi(f_{start}t + St^2)}, \tag{1}$$

with $S = \frac{B}{T_c}$ the slope of the chirp, for $B = f_{end} - f_{start}$ the bandwidth, and T_c the time duration of the chirp . When a reflected signal from a stationary object is received at an antenna, the incoming signal also has the form of a chirp but arrives with a time delay τ,

$$s_{Rx}(t) = e^{i\pi(f_{start}(t-\tau) + S(t-\tau)^2)}. \tag{2}$$

On the hardware of an mmWave radar is a mixer, which subtracts the received signal from the transmitted signal. This results in an intermediate frequency (IF) signal, which is then converted to a discrete signal by an analog to digital converter (ADC). The formula for the IF signal becomes

$$s_{IF}(t) = e^{i\pi(f_{start}\tau + S(2\tau t - \tau^2))} = e^{2i\pi S\tau t} e^{i\pi(f_{start}\tau - S\tau^2)} = e^{2i\pi S\tau t} e^{\phi}, \tag{3}$$

where the time-independent term is isolated as a phase shift ϕ, for $\phi = i\pi\tau(f_{start} - S\tau)$. Some mmWave radars only provide the real part of the IF signal as output, leading to the form

$$\mathrm{Re}(s_{IF}(t)) = \cos(2\pi S\tau t + \phi) = \cos(2\pi f_{IF} t + \phi), \tag{4}$$

where $f_{IF} = S\tau$ denotes the frequency of the IF signal, which is also called the beat frequency [47].

Figure 5 shows how the IF signal at frequency $S\tau$ results from the subtraction of the transmitted and received chirps. The IF signal only exists during the time period the two signals overlap.

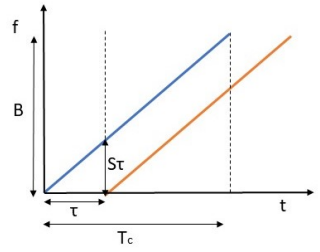

(a) Transmitted signal (blue), received signal (orange)

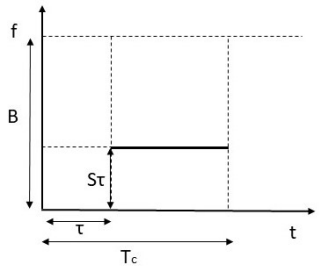

(b) IF signal

Figure 5: Frequency representation of mixing two signals to the IF signal

The output of the radar is raw data that consists of the discretised IF signal over N samples. For all k receiver antennas Rx this information is stored in M chirps, and over L frames. For each frame the information can be represented as a three-dimensional radar data cube with dimensions (k, M, N) as can be seen for the example in Figure 6.

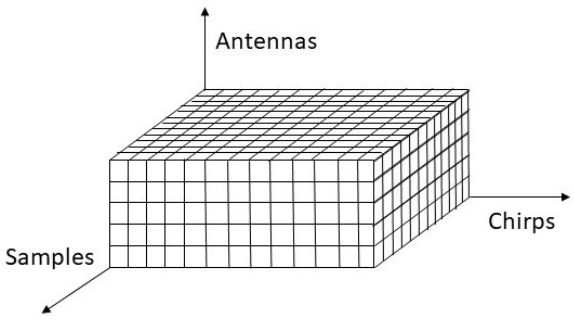

Figure 6: Radar data cube representation for a single time frame with $k = 5, M = 13, N = 12$

1.3.2 Range, Velocity, and Angle of Arrival

The reflected signal of an object at distance R arrives after a time delay $\tau = \frac{2R}{c}$, where c is the speed of light. As can also be seen from Figure 5, the IF frequency is equal to the frequency slope $S = B/T_c$ times the time delay τ,

$$f_{IF} = S\tau = \frac{2SR}{c} = \frac{2BR}{cT_c}, \tag{5}$$

with bandwidth B, and chirp duration time T_c. Rewriting leads to the following formula, which shows that the range R can be retrieved from the IF frequency by

$$R = \frac{cT_c}{2B} f_{IF}. \tag{6}$$

The phase of the IF signal ϕ_{IF} can be determined the moment the reflected signal arrives at the receiver antenna. Given Equation (1), the wavelength representation $\lambda = c/f_0$, and using $f_0 \gg S\tau/2$ for mmWave radar systems, the phase can be approximated as [41]

$$\phi_{IF} = 2\pi f_0 \tau + \pi S\tau^2 \approx 2\pi f_0 \tau = 4\pi R/\lambda. \tag{7}$$

In Figure 5 the received signal and computed IF frequency are shown for one object. When reflected signals from multiple objects are received, their individual frequencies can be separated by performing a Fourier transform. In a similar way, a second Fourier needs to be performed over the chirps to separate the individual phases.

Multiple chirps of duration T_c are transmitted after each other. When the object of detection is moving with velocity v with respect to the sensor, the object will have traveled $\Delta R = vT_c$ during one chirp. Based on Equations (5) and (7) the difference in frequency and chirp between two chirps are

$$\Delta f = \frac{2S\Delta R}{c} = \frac{2SvT_c}{c}, \tag{8}$$

$$\Delta \phi = \frac{4\pi \Delta R}{\lambda} = \frac{4\pi v T_c}{\lambda}. \tag{9}$$

In practice Δf is negligible compared to f_{IF}, because T_c is small. Nevertheless, $\Delta\phi$ can still be detected even when ΔR is only a millimeter. This means that from the difference in phase of the IF signal between multiple chirps the velocity of an object from and towards a receiver antenna can be computed by

$$v = \frac{\lambda \Delta \phi}{4\pi T_c}. \tag{10}$$

When multiple receiver antennas are aligned, the angle of arrival can be estimated. The orientation in which the antennas are positioned determines the angle it can detect. When antennas are placed in an L format or grid with arrays over both horizontal and vertical direction, both azimuth and elevation angles can be computed.

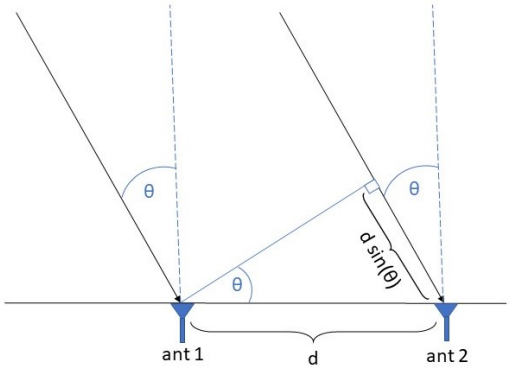

Figure 7: Angle of arrival estimation

Focusing on a single angular dimension, Figure 7 shows a reflected signal of an object, coming from an incident angle θ. By assumption the range R between the object and antennas is much larger than the distance d between the two antennas. Therefore the difference of incident angle between the two antennas is negligible and the incoming signal at both antennas is assumed to be parallel. However, the signal needs to travel further to the second antenna with the relative delay [41]

$$\Delta\tau = \frac{d\sin(\theta)}{c}. \tag{11}$$

Based on Equations (5) and (7), the differences in frequency and phase of the IF signal for two adjacent receiver antennas and incident angle θ are

$$\Delta f = S\Delta\tau = \frac{Sd\sin(\theta)}{c}, \tag{12}$$

$$\Delta\phi = 2\pi f_0\Delta\tau = \frac{2\pi d\sin(\theta)}{\lambda}. \tag{13}$$

Similar as explained for the velocity computation, because d is too small relative to R the difference in frequency of the IF signal becomes negligible with respect to f_{IF}. But $\Delta\phi$ is detectable and thus the angle of arrival can be computed as

$$\theta = \sin^{-1}(\frac{\lambda\Delta\phi}{2\pi d}). \tag{14}$$

1.3.3 Object detection

When all spatial and velocity information is derived from the IF signals, it cannot directly be used for applications. Although mmWave radar has increased accuracy because of its high frequency, it comes with the disadvantage that clutter of millimeter size also won't go unnoticed. This means that more interference is present in the received signals [50]. In order to be able to provide a useful representation for possible applications, it first needs to be determined which signals belong to actual objects of interest and which to ignore. The interference may include statistically distributed noise and undesired reflections of for instance unpredictable multipath reflections [75, 63]. Multipath reflections are indirect reflection paths which lead to detections at incorrect locations, these incorrect detections are also called ghost targets [8]. Interference in general is thus difficult to characterize, a distribution cannot be simply assumed [17].

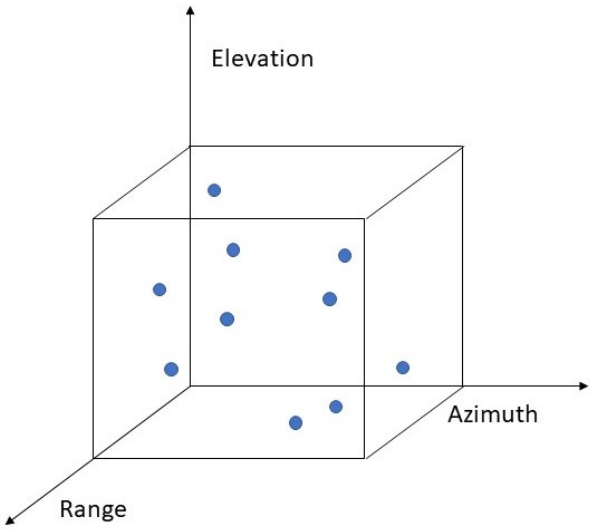

Figure 8: Example of a 3D point cloud

The simplest method to filter signals of interest, is to set a fixed threshold. Only when this threshold is exceeded, the received signal at that location is identified as an object. Using a fixed threshold does not result in good performance, object reflections are affected by many factors such as shape, material, range and size [17]. There may also be large variations in interference, which would require multiple thresholds to be able to detect all objects. For this reason have adaptive thresholding methods have been developed,

and are used in most modern radars [66]. Adaptive threshold detection methods determine the threshold by looking into the signals of the local region and are based on the assumption that background noise and clutter locally follow the same distribution [17]. Constant False Alarm Rate (CFAR) method is an adaptive thresholding method that is used by most modern radars [71], and results in point clouds as shown in Figure 8. Chapter 2 discusses the CFAR algorithm and its many variants in detail. Because interference makes detection a complicated problem, the detection performance is an important evaluation factor for radar sensors. The CFAR method keeps a constant probability of incorrect detections, and is therefore widely used.

1.4 Goal and Objectives

There are numerous reasons to integrate mmWave radar in monitoring applications in the healthcare sector, with (nursing) homes as environment. However, when considering the current applications and research, applications or tests in realistic living room settings are not included. Complex situations result in decreased detection performance, which calls for a more robust approach before real industrial implementations can take place or devices are build. This leads to the following overarching aim for this thesis:

Make the process of object detection with mmWave radar more robust.

The focus lies on the most common used radar object detection method, the constant false alarm rate (CFAR) method for setting adaptive thresholds. To genuinely understand the method, means not merely being able to follow the steps, but really understanding the underlying concepts and reasoning behind it. In available literature, such a complete overview including the theory is missing and the lack of this leads to the first research objective.

1 Provide a complete overview of steps including theory of the CFAR object detection method.

Within the CFAR method, the computation of the scaling factor is influenced by other choices and assumptions made in earlier steps. However, in literature and current research this does not always become clear. Therefore this thesis elaborates on and clarifies this interdependent relation as the second objective.

2 Clarify the relation between determination of the scaling factor and detector used.

To be able to actually test and check, the third objective is to develop an implementation for the path from radar output to object detection. This includes the CFAR method and multiple of its variations, but also the essential signal processing steps such as computing spatial dimensions of the received signals.

3 Develop an implementation from radar signal to point cloud.

Furthermore, mmWave radar point clouds are sparse compared to point clouds from other sensors. This is a disadvantage for most applications, and more informative point clouds are preferred. Therefore the fourth objective is to add a novel post-processing step to the processing path, which improves the point clouds by using information already gathered.

4 Proposition to informatively improve the generated point clouds.

To bridge the gap between theory and simulations to the real world, the last objective is to develop an experiment design that demonstrates the capabilities and differences in performance for variations in the CFAR object detection method, particularly for indoor practical implementations. The focus lies on the variants in estimators for the interference level, and the effect different environments have on them.

5 Design and conduct an experiment for testing in realistic living rooms.

1.5 Contributions and Thesis Outline

This thesis covers the previously mentioned five research objectives over three separate chapters. Figure 9 shows which objectives are covered in which chapters, and their relation to the general process from radar to application. Each colour represents a separate chapter.

Chapter 2 goes into depth in the CFAR adaptive threshold detection method and deals with the first two objectives. Detailed descriptions of the individual steps are provided, and a complete overview of the method is created. The assumptions and theory on which computations within the method rely are also elaborated on, which is new for such an overview. For each step within the method, there are multiple

options to be chosen from which lead to many possible variations of the method. Choices regarding certain steps influence later steps within the method, however this is not always made clear. Therefore specific attention is given to the interdependent relation between these steps, showing the practical implications that may result when this relation is not correctly taken into account.

Chapter 3 covers the implementation of the point cloud generation, with simulated radar signals as input. The spatial information is retrieved during the signal processing step, where not a standard angle detection method is used. To calculate the angle of arrival for both azimuth and elevation angles at the same time, the algorithm is adjusted. Variations of the object detection method from Chapter 2 are included in the implementation, including the effect of incorrect combinations within the method which are shown according to the simulations. Additionally, the fourth objective is included by implementing a novel post-processing step, which improves how informative the point clouds are. Using simulated signals, the results from adding this step are shown.

Chapter 4 addresses the last objective, namely the experiment. An entire experiment has been designed to demonstrate and test the capabilities of the different CFAR variants for realistic indoor environments. Experiments for these specific situations have not yet been conducted before, therefore the decisions for the experiment setup have carefully been thought out. From setting the parameters and determining which properties and characteristics of the rooms will be analysed, to finding a location and performing the actual measurements. The acquired mmWave data is processed using the previously mentioned implementation framework, and thus also includes the adjusted angle detection and informative improved step.

This thesis ends with a discussion, suggestions, and an outlook on possible future research in Chapter 5.

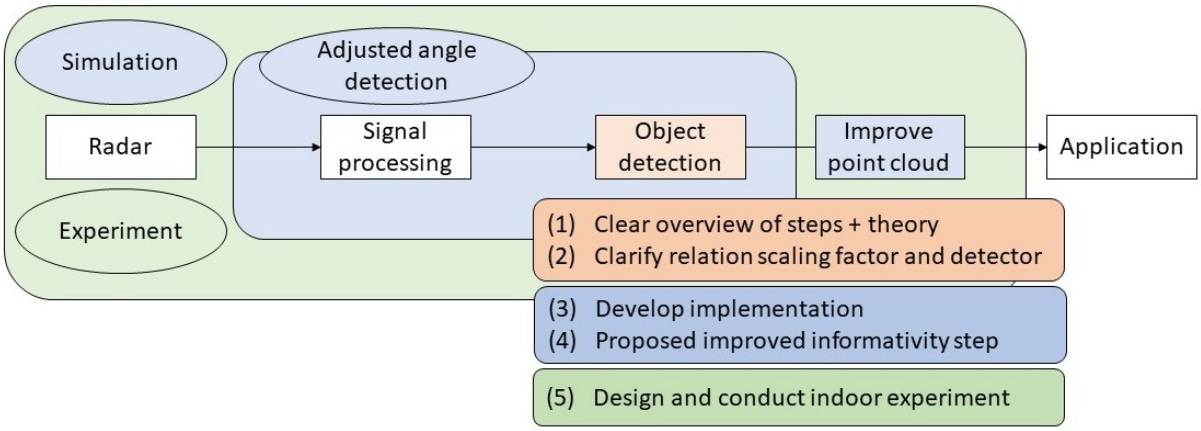

Figure 9: Overview of the general process from radar to application, and the contributions in relation to the chapters. Chapter 2 in orange, Chapter 3 in blue, and Chapter 4 in green.

2 Constant False Alarm Rate Adaptive Threshold Detection

Using a fixed threshold is undesired for object detection, it results in a decreased detection performance and increased false alarm rate because the background clutter is unlikely to be the same everywhere [16]. Because interference is almost always present in the received radar signals and detection algorithms are sensitive to interference, it is desired to keep false detections at a constant low to increase reliability [17]. The CFAR method uses an adaptive thresholding technique that resolves this problem by looking into the regional background and thus taking into account local variations. When interference is present, these signals will be contained in the surroundings and hence should in some way be included in the threshold.

This chapter focuses on the object detection part and addresses the first and second research objectives, as shown in Figure 10. It Includes a detailed explanation on the method, covering not only the steps of the method but also the reasoning and theory behind it. The information on the specific assumptions and relations between steps has not yet been clearly described in one overview, but was distributed over many works and had to be gathered and structured. This chapter provides the complete overview in section 2.1, and explains the most important variations on determining the background interference level in section 2.2. The interdependent relation of the steps is often scarcely reported, but is explicitly clarified in section 2.3. Specifically the determination of the scaling factor and why incorrect combinations will lead to decreased detection performance is elaborated on.

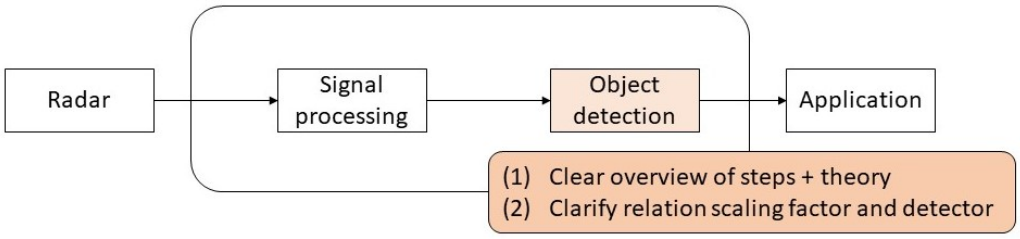

Figure 10: Relation between this chapter, the first two research objectives, and the general process from radar to application.

2.1 Basic Method

The CFAR adaptive threshold detection method is carried out over each dimension individually, and consists of multiple steps which are shown in Figure 11. In this section the path from input data to presence detection is followed. Section 2.1.1 explains how the background interference level is estimated, section 2.1.2 elaborates on the details of the scaling factor and how it is computed, and section 2.1.3 goes into depth on how presence and absence are determined.

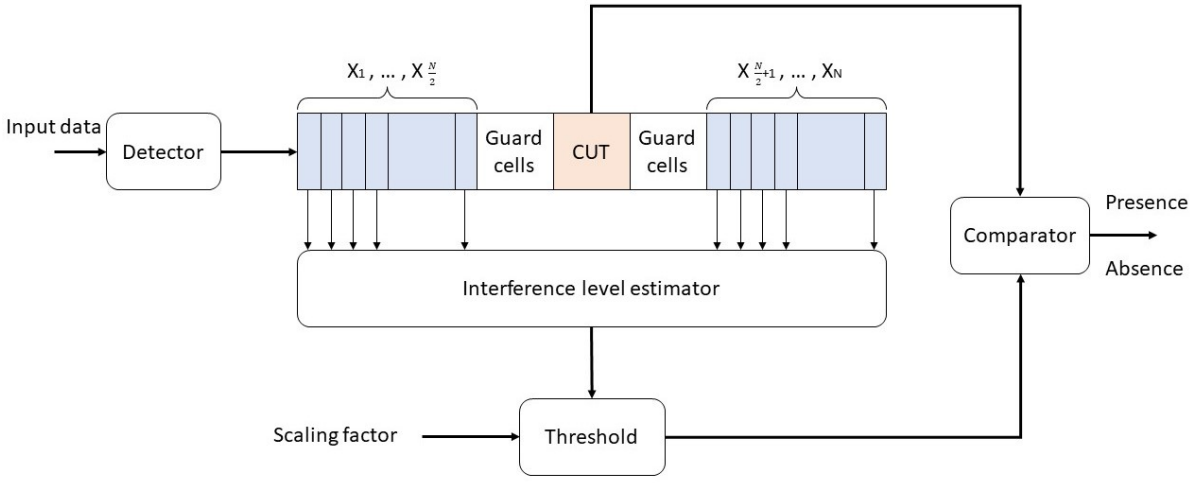

Figure 11: CFAR object detection scheme

2.1.1 Interference Level Estimation

A distinctive feature of the CFAR method is that it uses a sliding window technique, where along one dimension each cell is individually evaluated for absence or presence of objects with respect to its local background. The cells directly next to the cell under test (CUT) are called the guard cells and are excluded from the interference estimation because it may occur that a reflected signal covers multiple cells. Excluding them prevents signals of the object of detection being treated as background interference. The local background on which the estimation is based are the reference cells $X_i, i = 1, ..., N$, which form the reference window and are assumed to be a proper representation of the background interference level.

Before the background interference level is estimated, a detector is applied on the input data. The choice of detector has influence on both the detection performance and computational costs, and thus the general performance of the CFAR algorithm [49]. Common detectors are the linear law detector that uses the original data, and the square law detector that uses the squared data [60]. Thus for original input data $\bar{X}_i$, the linear law detector gives $X_i = \bar{X}_i$, and the square law detector $X_i = \bar{X}_i^2$, $i = 1, ..., N$.

After a detector has been used over the input data, the interference level is estimated. There are multiple ways to do this, the easiest way is to take the average over the reference window, this is called Cell Averaging (CA) CFAR, and the estimated interference level is

$$Z_{CA} = \frac{1}{N} \sum_{i=1}^{N} X_i. \tag{15}$$

2.1.2 Scaling Factor

To maintain a constant false alarm rate, the estimated interference level needs to be scaled with respect to its probability of false alarms. This scaling factor is dependent on the distribution of interference, the type of detector, which estimation variant is used, and the size N of the reference window. The interference distribution usually is unknown and difficult to approximate, but Rayleigh and Weibull are two distributions that are commonly used [45]. The Rayleigh distribution is the standard for i.i.d. Gaussian noise and suitable to describe meteorological and ground interference for low resolution radar [49]. The Weibull distribution for non-Gaussian noise is the norm for high resolution and weather interference situations [12, 69].

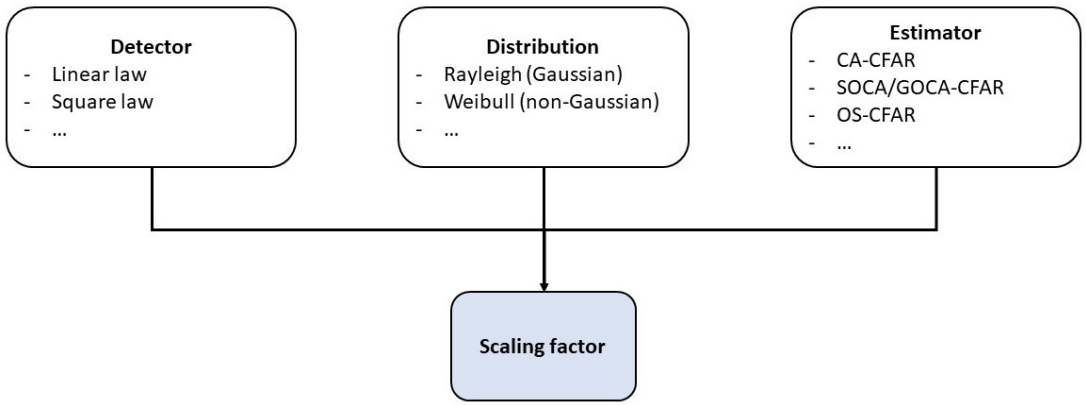

Figure 12: Interdependence of detector, background interference distribution and estimator, and the scaling factor.

For an assumed Gaussian distribution, the probabilities of false alarm can be computed analytically and their complete derivations can be found in [64]. The probabilities of false alarm for a linear detector and square law detector with Gaussian distributed interference are [60]

$$P_{FA,CA}^{(lin)} = \left(1 + \frac{\alpha^2}{N(\frac{4}{\pi} - (\frac{4}{\pi} - 1)e^{-\frac{4}{\pi}+1})}\right)^{-N}, \tag{16}$$

$$P_{FA,CA}^{(sq)} = \left(\frac{\alpha}{N} + 1\right)^{-N}. \tag{17}$$

In these equations α is the scaling factor, which can be obtained by rewriting the formulas and when P_{FA} is known . Hence the scaling factor for CA-CFAR with a Rayleigh distribution for both the square law and linear law detectors are the following [64],

$$\alpha_{CA}^{(lin)} = \sqrt{N\left(P_{FA}^{-1/N} - 1\right)\left(\frac{4}{\pi} - (\frac{4}{\pi} - 1)e^{1-N}\right)}, \tag{18}$$

$$\alpha_{CA}^{(sq)} = N(P_{FA}^{\frac{1}{N}} - 1). \tag{19}$$

For the Weibull distribution no closed form expression for the scaling factor exists, but can be computed with for instance Monte Carlo simulation [49]. The interference estimator is multiplied with the scaling factor to come to the adaptive detection threshold [29]

$$\gamma_{CA} = \alpha_{CA} Z_{CA}. \tag{20}$$

2.1.3 Hypothesis Test and Neyman-Pearson Lemma

Dependent on the background interference estimation and the computed scaling factor, a threshold is computed which determines whether a received signal is detected as an object or not. The detection is a binary hypothesis test, with hypotheses

$$\begin{aligned} H_0 &: \text{ Object is absent,} \\ H_1 &: \text{ Object is present.} \end{aligned}$$

In the hypothesis test, the CUT is compared to the threshold for presence and absence detection according to the likelihood ratio test (LRT) [51]. If the CUT has a higher value than the threshold γ, the null hypothesis H_0 is rejected and presence H_1 is detected. If the threshold is not passed, the null hypothesis H_0 is accepted,

$$CUT \gtrless_{H_0}^{H_1} \gamma. \tag{21}$$

The probability of detection P_D (true positive) and the probability of false alarm P_{FA} (false positive, type I error) can be written as the probabilities

$$P_D = P(CUT > \gamma | H_1) = P(H_1|H_1), \tag{22}$$

$$P_{FA} = P(CUT < \gamma | H_1) = P(H_1|H_0). \tag{23}$$

The goal of the CFAR method is to maximize the probability of detection P_D, while maintaining a low constant probability of false alarms P_{FA}. This increases the chance of correct identification of true positives, and is is based on the Neyman-Pearson lemma. The lemma states that to optimize the detection performance while maintaining a predetermined significance level, the LRT is the most powerful test to use [51]. To get a better understanding of the lemma this method is based on, the lemma and a proof adapted from [59] are presented below.

Theorem 2.1 (Neyman-Pearson Lemma)**.** *To solve the constrained optimization problem*

$$max\ P_D\ s.t.\ P_{FA} = c,$$

decide according to the likelihood ratio test (LRT)

$$\Gamma(x) = \frac{p_1(x)}{p_0(x)} \gtrless_{H_0}^{H_1} \gamma. \tag{24}$$

Proof. The region where the likelihood ratio test decides H_1 is

$$R_{NP} = \left\{ x : \frac{p_1(x)}{p_0(x)} \geq \gamma \right\}. \tag{25}$$

Let R_T denote the region where some other test describes H_1. For any region R, the probability of $x \in R$ under hypothesis H_i is

$$P_i(R) = \int_R p_i(x) dx. \tag{26}$$

By assumption both test have $P_{FA} = c$,

$$c = P_0(R_{NP}) = P_0(R_T). \tag{27}$$

Now note that the regions can be rewritten as

$$P_i(R_{NP}) = P_i(R_{NP} \cap R_T) + P_i(R_{NP} \cap R_T^C), \tag{28}$$

$$P_i(R_T) = P_i(R_{NP} \cap R_T) + P_i(R_{NP}^C \cap R_T). \tag{29}$$

Hence rewrite Equations (28) and (29) into (27) to see that

$$P_i(R_{NP} \cap R_T^C) = P_i(R_{NP}^C \cap R_T). \tag{30}$$

To show that indeed the detection probability of the Neyman-Pearson Likelihood Ratio test is larger than the probability of detection of any other test, it needs to be shown that

$$P_1(R_{NP}) \geq P_1(R_T). \tag{31}$$

Using Equation (30) this holds if $P_1(R_{NP} \cap R_T^C) \geq P_1(R_{NP}^C \cap R_T)$. Note that

$$\begin{aligned}
P_1(R_{NP} \cap R_T^C) &= \int_{R_{NP} \cap R_T^C} p_1(x)dx \text{ (by Equation (26))} && (32)\\
&\geq \gamma \int_{R_{NP} \cap R_T^C} p_0(x)dx \text{ (by Equation (25))} && (33)\\
&= \gamma P_0(R_{NP} \cap R_T^C) \text{ (by Equation (26))} && (34)\\
&= \gamma P_0(R_{NP}^C \cap R_T) \text{ (by Equation (30))} && (35)\\
&= \gamma \int_{R_{NP}^C \cap R_T} p_0(x)dx \text{ (by Equation (26))} && (36)\\
&\geq \int_{R_{NP}^C \cap R_T} p_1(x)dx \text{ (by Equation (25))} && (37)\\
&= P_1(R_{NP}^C \cap R_T) \text{ (by Equation (26))}. && (38)
\end{aligned}$$

Hence it can be concluded that $P_1(R_{NP} \cap R_T^C) \geq P_1(R_{NP}^C \cap R_T)$ and thus $P_1(R_{NP}) \geq P_1(R_T)$, which means that the probability of detection is largest for the likelihood ratio test compared to any other test for the same probability of false detections. This agrees with the Neyman-Pearson lemma. □

2.2 Interference Estimation Variations

Now that the steps of the basic method and the theory behind it are known, there are also other ways to estimate the background interference level. In the previous section the method is explained according to the CA-CFAR interference estimator, but there exist more. They all use arithmetic averaging and the most important ones are elaborated on in this section.

2.2.1 Smallest/Greatest of Cell Averaging

As explained in section 2.1, the CA-CFAR estimator averages over the entire reference window. Although this estimation method is easy to implement, has low computational costs, and performs well for homogeneous clutter situations, there are difficulties encountered for more realistic environments [29, 16]. When signals from other objects are in the reference window for another object, it may occur that only one of them will be detected [40]. The peak signal from another object is then included in the interference estimation, and therefore the assumption of an independent identical distribution does not hold anymore. This may result in a too high threshold for the other to be detected, and is called the masking effect.

Additionally, the environment may also suddenly change, for instance naval radars encounter the transition between water and air. When their interference levels are different, this transition is called a clutter edge [61]. When such a clutter edge is present in the reference window, objects in the lower interference region may be masked. The other way around, a decreased threshold may also result in false alarms.

To resolve the difficulties regarding non-homogeneous interference environments such as clutter edges and multiple objects, Hansen and Swayers [25] proposed two variations of the CA-CFAR interference estimator. Smallest of (SO) CA-CFAR deals with the multiple target situation, whereas greatest of (GO) CA-CFAR handles clutter edges. Both variants split the reference window in a leading and lagging part, and average over them separately. SOCA-CFAR takes the minimum of the two averages as estimator, whereas GOCA-CFAR takes the maximum of the two,

$$Z_{SOCA} = \frac{2}{N} min(\sum_{i=1}^{N/2} X_i, \sum_{i=N/2+1}^{N} X_i), \tag{39}$$

$$Z_{GOCA} = \frac{2}{N} max(\sum_{i=1}^{N/2} X_i, \sum_{i=N/2+1}^{N} X_i). \tag{40}$$

The scaling factors α_{SOCA} and α_{GOCA} for Rayleigh distributed interference and the square law detector can be computed from the false alarm probabilities [68]

$$P_{FA,SOCA} = 2 \sum_{i=0}^{N/2-1} \binom{N+i-2}{i} \frac{1}{(2+2\alpha_{SOCA}/N)^{N/2+i}}, \tag{41}$$

$$P_{FA,GOCA} = 2\frac{1}{\sqrt{(1+2\frac{\alpha_{GOCA}}{N})^N}} - 2 \sum_{i=0}^{N/2-1} \binom{N+i-2}{i} \frac{1}{(2+2\alpha_{GOCA}/N)^{N/2+i}}. \tag{42}$$

Both variants remain to have difficulties. The SOCA-CFAR estimator has improved performance when a second object is present in the reference window, but does not perform well when a clutter edge is present. The GOCA-CFAR estimator is exactly the other way around, it performs well when a clutter edge is present in the reference window, but degrades in performance in presence of another object. So when both a clutter edge and another object are present, neither of the two variants performs well.

2.2.2 Ordered Statistic

The ordered statistic (OS) CFAR variant has been developed to be able to deal with both difficulties at the same time, multiple objects and clutter edges. The idea behind it is that the signals with largest magnitude do not belong to ordinary interference, and should therefore be discarded from the estimation. The first step of the OS-CFAR variant is ordering the reference window by increasing magnitude

$$X_{(1)} \leq X_{(2)} \leq ... \leq X_{(N)}, \tag{43}$$

where $X_{(1)}$ denotes the smallest value and $X_{(N)}$ the largest [66]. The OS-CFAR method does not use the entire reference window for its estimation, but takes one value $X_{(k)}, k \in 1, 2, ..., N$ as an estimate for the interference level,

$$Z_{OS} = X_{(k)}. \tag{44}$$

Where for other variants guard cells need to be excluded from the estimation in case they might contain the object of detection, OS-CFAR already excludes the highest $N - k$ signals and thus does not require exclusion of guard cells for the reference window.

The threshold γ is computed similar to the CA-CFAR threshold, but with a different estimator and scaling factor. The scaling factor α for the square law detector and both Rayleigh and Weibull interference, it can be derived from the probability of false alarm [37]

$$P_{FA,OS}^{(sq)} = \frac{N!}{N-k} \frac{(\alpha_{OS}^{(sq)} + N - k)!}{(\alpha_{OS}^{(sq)} + N)!}. \tag{45}$$

The scaling factor for the linear detector for both Rayleigh and Weibull distributed interference is computed according to [64, 66]

$$\alpha_{OS}^{(lin)} = \sqrt{\alpha_{OS}^{(sq)}}. \tag{46}$$

OS-CFAR has increased performance over CA-CFAR variants when multiple objects and clutter edges are present [29]. A limitation of the variant is that it requires longer processing time, because the reference

window needs to be ordered [6]. Dependent on which ordering algorithm is chosen, this can be decreased but will always have higher computational costs than CA-CFAR estimator variants. Another advantage is that it is able to detect closely spaced targets, but when a lot of clutter is present and k is chosen either too large or too small, there will be a lot of difficulties encountered [16].

2.2.3 Others

Where the OS-CFAR interference estimator takes the k-th cell as estimator, the Censored Mean Level Detector (CMLD) CFAR variant uses the k smallest cells of the reference window [65]. This means the estimated interference level is computed as

$$Z_{CMLD} = \frac{1}{k} \sum_{i=1}^{k} X_{(i)}. \tag{47}$$

If there are multiple objects present in the reference window, this method has increased performance. That is, as long as not more than $N - k$ cells of the reference window contain signals from those objects. At the same time the performance may decrease for other situations, as the reference window and thus the amount of information used decreases as well.

The Trimmed Mean (TM) CFAR variant does not only exclude the largest $N - k$ cells from the reference window, but also the smallest l are neglected [19].

$$Z_{TM} = \frac{1}{k - l} \sum_{i=l}^{k} X_{(i)}. \tag{48}$$

Both CMLD- and TM-CFAR are outlier rejection variants, and have increased performance for nonhomogenous situations. A disadvantage of the estimators is that the computation costs is also increased, the reference window needs to be ordered and then the mean needs to be calculated. Furthermore, in the ideal situation it would be known a priori how many objects there are to be detected, such that the right amount of largest cells can be excluded. However, in realistic situations this is never known beforehand.

There are more CFAR interference estimation variants. Most often they are improved versions of the ones described here, several variants are combined or computational efforts are decreased compared to the original variants [85, 33]. These improved versions are often developed for naval applications, where every second matters when detecting rockets and missiles in the air. Similar for the automotive industry, where time is also of importance for avoiding collisions.

2.3 Determination of Scaling Factor

How the scaling factor should be computed is dependent on multiple factors, as explained in section 2.1.2. However, in literature not all parts of the CFAR detection method are always elaborated on, which leaves unclarity about the exact procedure followed. The scaling factor scales with respect to all choices made within the method, hence when the scaling factor is not accurately matched with another step in the procedure, this results in decreased performance.

To elaborate on this unclarity, first an overview regarding unclarity in current literature is provided. Apart from the lack of mentioning all steps of the method, there exist a few cases which suggest that a theoretically incorrect combination of detector and scaling factor are made. Therefore the importance of using the correct scaling factor for detection is elaborated on afterwards, according to an example for this specific situation of incorrect combination.

2.3.1 Literature

Because the scaling factor depends on the detector, assumed distribution, and interference estimator, it is thus important to know which detector is used. Often the detector is not mentioned at all, but when the method is used correctly this may also be derived from how the scaling factor is computed.

There is literature that mentions which detector is used [43]. In most cases this is the square law detector, although explanation on why this detector has been chosen is lacking [25, 29, 15, 61, 39], [50, 5]. However, [49] compares multiple detectors and shows that the square law detector offers indeed in most cases the

best performance. In the case of Gaussian noise, the linear law and square law have similar performance, but even then the square law is still preferred due to its lower computational costs.

Nevertheless, in literature there also exist cases where the step of using a scaling factor is mentioned, but no further information on which one or how it is calculated is provided [84, 79, 10]. Information on the detector used is not provided either. When the formula for the scaling factor is given, the detector used is frequently not mentioned [58] nor included in the elaborate diagrams that are provided [26, 78]. This does not necessarily mean that an incorrect combination has been used, but when there is not more information available it also cannot be checked.

Sometimes code of the implementation is publicly available, and the exact steps can be traced. There are cases which suggest that an incorrect scaling factor is used, as the formula for the square law detector is implemented although the squared data step is missing [14]. Possibly the data is squared during a pre-processing step that is not included in the implementation, but it can be checked that this is not included in the data set used either [18].

Even though for some cases the procedure is correctly mentioned in literature [9, 56], the corresponding available code suggests otherwise. For these specific cases, the square law detector does not seem to have been applied in the implementation, although the corresponding scaling factor is used. The author has been informed about it and states that a very good point has been raised and thinks probably a mistake has been made in the code [55].

2.3.2 Effect and Importance

From the previous subsection it becomes clear that a mistake of using an incorrect combination is easily made. However, such an incorrect combination may result in a decrease of detection performance. This section shows the effect of using an incorrect scaling factor can have on the detection performance.

In Figure 13 the sampled signal signals and their correct thresholds are shown for both the linear law and square law detector. For both detectors the threshold is computed for the CA-CFAR interference estimator and scaling factors according to Equations (18) and (19). The samples where the signal passes the threshold are shown in 13d, and for both linear and square law the same samples are detected as objects.

As can be seen from Figure 13b, applying the square law detector results in a less gradual and more steep slope and a stronger signal compared to the linear law detector. The scaling factors developed for both detectors take this difference into account, such that they will result in the same detection as is shown in Figure 13d. When the scaling factor for the square law detector is used although the detector has not been applied to the signal samples, the signal will not be detected. The square law scaling factor takes into account the increased signal strength, which results in a higher threshold. Figure 14 shows what happens when the scaling factor from Equation (19) is used for both the linear and square law detector. The linear threshold is set too high and the signal is not detected by the algorithm. Therefore the scaling factors that belong to the correct detectors should be used, and incorrect combinations result in undetected signals.

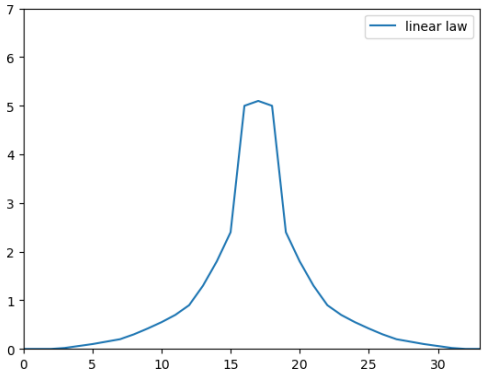

(a) Original sampled signal

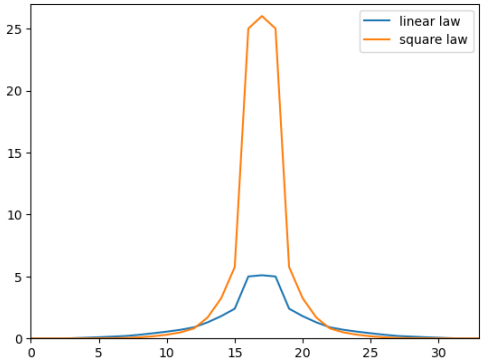

(b) Original and squared sampled signals

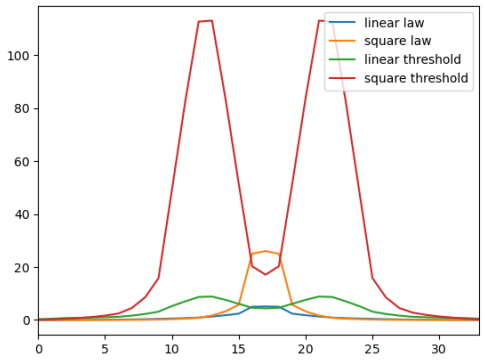

(c) Sampled signal and thresholds

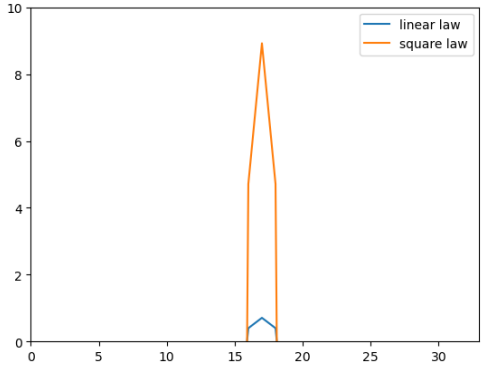

(d) Detected samples

Figure 13: Correct combination of scaling factors and law detectors. Figure 13d shows that the region of detection where the thresholds are passed is similar for bot linear and square law.

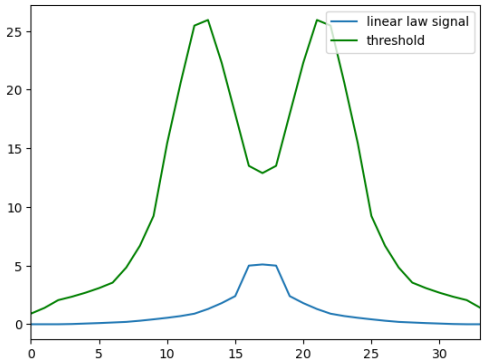

Figure 14: Incorrect combination, square law scaling factor used on the linear law detector. The new incorrect threshold is not passed.

3 Implementation

This chapter elaborates on the entire path from reflected signal to generated point cloud, by following the steps of the developed Python implementation. Radar signals are simulated and used as input. Section 3.1 focuses on the signal processing step, and explains and shows how the velocity and three-dimensional spatial information are retrieved. To determine the angles of arrival, the Minimum Variance Distortionless Response (MVDR) method is implemented. This method determines the angle over one dimension, but has now been adjusted such that both azimuth and elevation angle can be detected at once.

Section 3.2 includes the implementation of the CFAR detection method, and the interference level estimator variations as described in Chapter 2. Their differences and the effects caused by change in sliding window parameters are shown. Furthermore, to improve how informative the generated point clouds are, a post-processing step is proposed and its resulting point clouds are included.

How this chapter and covered objectives relate to the general process from radar to application, is shown in Figure 15.

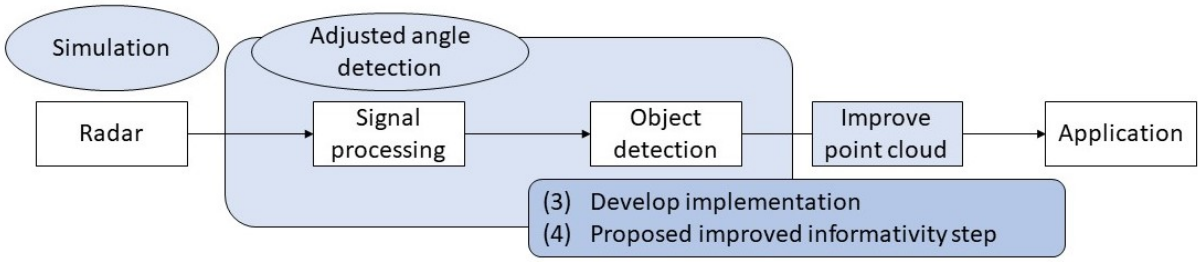

Figure 15: Relation between this chapter, the two research objectives covered, and the general process from radar to application.

To validate the computation steps in the signal processing as well as the detection implementation, simulations have been performed. All individual steps of the signal processing and detection path are explained along these simulation results. The radar parameters used for the simulation are the same as for the experimental results in Chapter 4 and are shown in Table 1a.

For the results in this chapter, the reflected signals of three separate objects have been simulated with various amplitude (A), range from the radar (R), velocity (v), azimuth angle (θ), and elevation angle (ψ). Table 1b shows the values for these object parameters. It should be noted that the simulations do not include any interference effects, and the objects are distinctly separated from each other in both spatial and velocity domains.

N_{Tx}	1	f_0	60 GHz
N_{Rx}	3	B	3 GHz
N_C	128	S	4 MHz/μ s
N_S	512	T_c	750 μ s

(a) Radar parameters

	A(V)	R(m)	v(m/s)	θ(°)	ψ(°)
A	1	3	0	-10	3
B	0.7	5	-1.2	5	8
C	0.5	4	0.7	10	10

(b) Object parameters

Table 1: Simulation parameter values

3.1 Signal Processing

This section describes how four-dimensional (range, azimuth, elevation, velocity) data representations are formed from the raw radar output (antenna, frame, chirp, sample). Range and velocity can be retrieved from mmWave radar signals by performing Fourier transforms, and is shown according to simulations in section 3.1.1. The azimuth and elevation angle are retrieved according to the MVDR method, which is explained in section 3.1.2. The method is meant for angle detection over only one dimension, but is adjusted such that both angles can be detected simultaneously.

3.1.1 Range and Velocity

Three objects are simulated according to the parameters in Table 1. All three objects result in a reflected signal with the frequency dependent on their range from the radar. The IF signal measured at the receiver antenna is a linear combination of all three waves, shown in Figure 16a. From this combined signal the independent frequencies cannot be directly determined, but a Fourier transform first needs to be applied which results in peaks at the separate frequencies and is shown in Figure 16b.

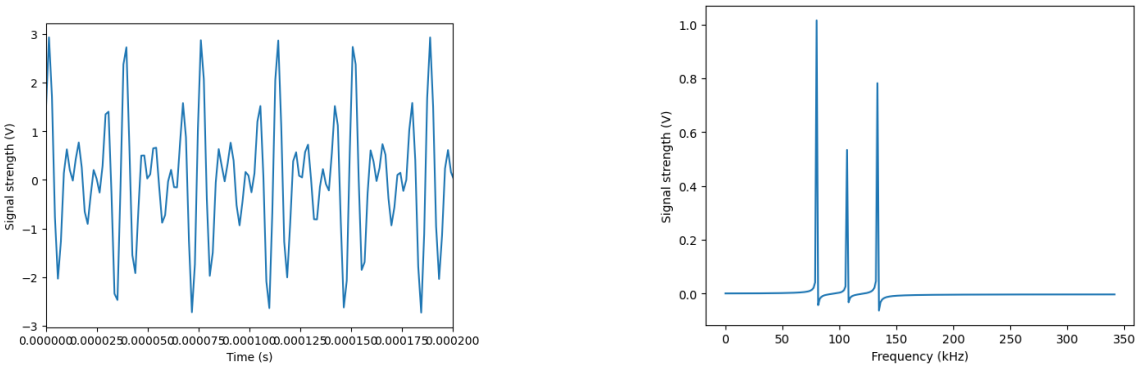

(a) Time domain

(b) Frequency domain

Figure 16: Fourier transform of IF signal

The IF signal is sampled in 512 data points over one chirp. Although one chirp is only less than a millisecond, change in movement can be detected. Figure 17a shows the range of the three objects over the duration of one chirp. The objects A, B, and C have traveled 0 m, -0.9 mm, and 0.5 mm respectively.

Chirps are stacked one after another as a frame of 128 successive chirps. Looking at the change in range over these chirps, the velocity can be detected be performing another Fourier transform. Figure 17b shows the range and velocity for the three objects.

Object A has a higher amplitude and does not change position. Object B and C both already have a less strong signal and move from or towards the radar. This causes the spread and less bright signal seen in the figure, because the objects covers more range whereas object A remains at a constant location.

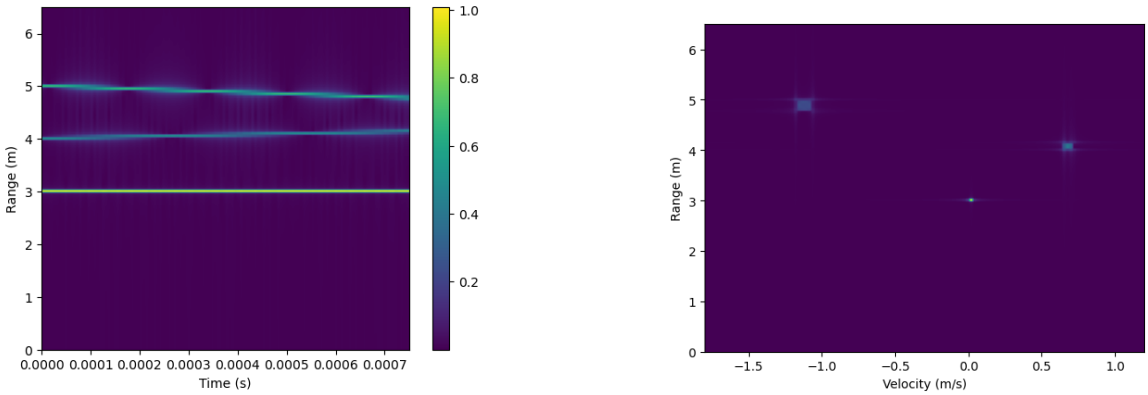

(a) Range over a single chirp

(b) Velocity over a single frame

Figure 17: Computing the velocity for three simulated objects

3.1.2 Azimuth and Elevation Angle

The mmWave radar board that is used for the experiment described in Chapter 4, and has three receiver antennas. These antennas are shaped in an L-format, which means that for the detection of azimuth angle there are two antennas to use, for the elevation angle likewise.

The time delay and corresponding phase difference for a two antenna receiver array for a signal incoming

at incident angle θ is

$$\Delta\tau = \left[0, \quad \frac{d\sin(\theta)}{c}\right], \tag{49}$$

$$\Delta\phi = \left[0, \quad \frac{2\pi d\sin(\theta)}{\lambda}\right], \tag{50}$$

for d the spacing between the antennas, c the speed of light, and λ its wavelength. The angle of arrival can be determined by performing another Fourier transform, now over the aligned antennas. When there are not that many antennas in one array, the angle estimation is not very accurate and hence other methods are preferred [74]. There are multiple methods to determine the angle of arrival for only two aligned antennas. Most of them rely on angle vectors and the spatial covariance matrix, from which the respective signal strength is determined.

Suppose M antennas receive signals from L separate sources, than the received signal at antenna $k \in M$ of source $l \in L$ is

$$S_k(t) \approx s_l(t)e^{\frac{-i2\pi dk\sin(\theta)}{\lambda}} = s_l(t)a_k(\theta_l), \tag{51}$$

where $s_l(t)$ for $l = 0, 1, ...L-1$ denotes the the signal coming from the lth source signal, and $a_k(\theta) = e^{\frac{-i2\pi dk\sin(\theta)}{\lambda}}$ is the angle vector. Then the combined received signal from all L sources for antenna k is

$$S_k(t) \approx \sum_{l=0}^{L-1} s_l(t)a(\theta_l). \tag{52}$$

This results in the matrix representation

$$x(t) = \begin{bmatrix} a(\theta_0) & a(\theta_1) & ... & a(\theta_{L-1}) \end{bmatrix} s(t) + n(t) = As(t) + n(t), \tag{53}$$

for A the Mx L angle matrix, $s(t)$ the received signal vector, and $n(t)$ the noise. Note that for the case of the simulation and the experiment $M = 2$ for both angles and thus the angle matrix is of the form

$$A = \begin{bmatrix} 1 & 1 & ... & 1 \\ e^{\frac{i2\pi d\sin(\theta_1)}{\lambda}} & e^{\frac{i2\pi d\sin(\theta_2)}{\lambda}} & ... & e^{\frac{i2\pi d\sin(\theta_l)}{\lambda}} \end{bmatrix}. \tag{54}$$

Suppose that the noise $n(t)$ has zero mean, covariance matrix $\sigma^2 I$ and is uncorrelated to $s(t)$. Then the spatial correlation matrix is

$$R = \mathbb{E}[x(t)x(t)^H] \tag{55}$$

$$= \mathbb{E}[(As(t) + n(t))(As(t) + n(t))^H] \tag{56}$$

$$= A\mathbb{E}[s(t)s(t)^H]A^H + \mathbb{E}[n(t)b(t)^H] \tag{57}$$

$$= AR_sA^H + \sigma^2 I. \tag{58}$$

The most common angle estimation methods can be divided over two categories: extrema search, and matrix shifts. The delay-and-sum (DS) method [22], the minimum variance distortionless response (MVDR) method [27] and multiple signal classifier (MUSIC) method [70] are extrema searching techniques. Estimation of signal parameters via rotational invariance techniques (ESPRIT) is a well-known matrix-shifting technique [67]. The MUSIC and ESPRIT methods have cubic complexity, whereas the DS and MVDR method have quadratic complexity and are therefore preferred [21]. Because MVDR has higher resolution than DS, the MVDR method is chosen as angle detection method.

The MVDR method is based on beamforming, and computes the signal strength for all possible directions. Beamforming means that a set of weights w optimizes a specific parameter, here maximizing the signal from the angle of interest. Hence consider the weighted signal

$$y(t) = w^H x(t). \tag{59}$$

The goal of this method is to minimize the signal power belonging to other angles, while setting the response for an individual angle to 1. Thus for each possible angle θ, the signal power is minimized w.r.t. a single constraint,

$$\min_w \ w^H Rw \tag{60}$$

$$\text{s.t. } w^H a(\theta) = 1. \tag{61}$$

Using Lagrangian multipliers, the signal power at angle θ is computed as [38, 81]

$$P(\theta) = \frac{1}{a(\theta)^H R^{-1} a(\theta)}, \tag{62}$$

$$R = \mathbb{E}[S(\theta)^H S(t)]. \tag{63}$$

For the three simulated objects as described in the previous section, the azimuth angle is computed and shown as angle with respect to the range in Figure 18a, and in polar coordinates in Figure 18b. Figures 18c and 18d also show the elevation angle of the three objects in both domains.

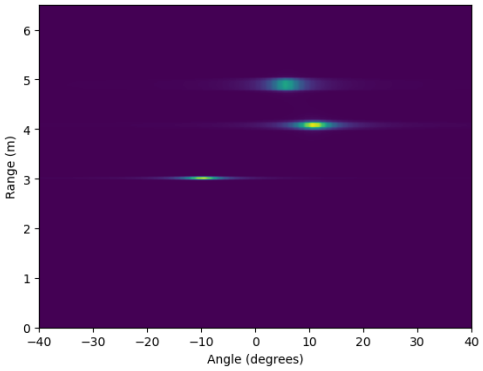

(a) Range-azimuth, angle domain

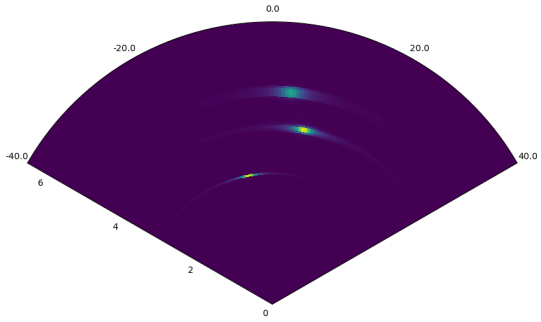

(b) Range-azimuth, 2D spatial domain

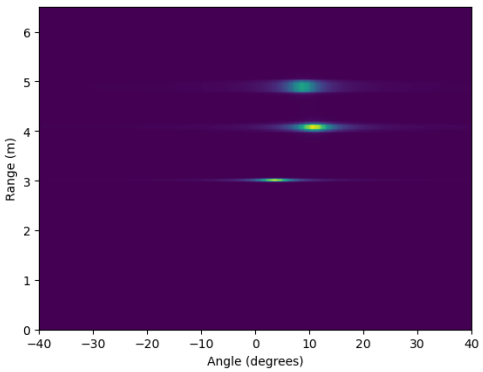

(c) Range-elevation, angle domain

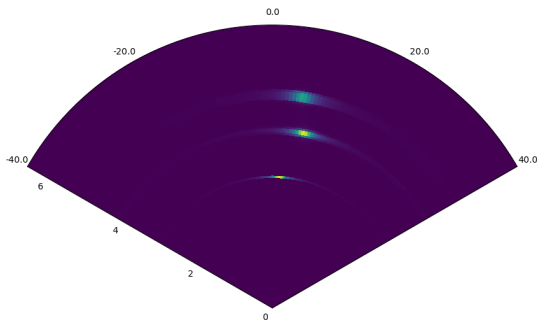

(d) Range-elevation, 2D spatial domain

Figure 18: Range w.r.t. azimuth and elevation angle of three simulated objects

For both angle dimensions the angles are known corresponding to their range. Because the three objects have distinct ranges, the azimuth and elevation angles can be matched to the correct object and is called pair-matching [48]. However, it is not always the case that all objects have separate range distances. Therefore a method where both angular dimensions are measured simultaneously is preferred. Combined-angle method implementations exist for MUSIC and ESPRIT [20]. The procedure of this extension to combined angle estimation is used and adjusted for the MVDR method.

The concept of the method stays the same, but computations need to be adjusted. Consider the angle matrix A_θ for the azimuth angle θ, and A_ψ for the elevation angle for A according to Equation (54). Then for two angle dimension at the same time the angle matrix is computed as the Kronecker product

$$A_{\theta,\psi} = A_\theta \otimes A_\psi. \tag{64}$$

Both angle matrices are of dimension $(2 \cdot n)$, for n the number of angular segments over which the signals are estimated. The dimension of the combined angular matrix now becomes $(2^2 \cdot n^2)$, which also increases the computational complexity. Figure 19 shows the combined angles for each of the simulated objects from Table 1b separately. It can be seen that the strength of the signals is indeed in descending order.

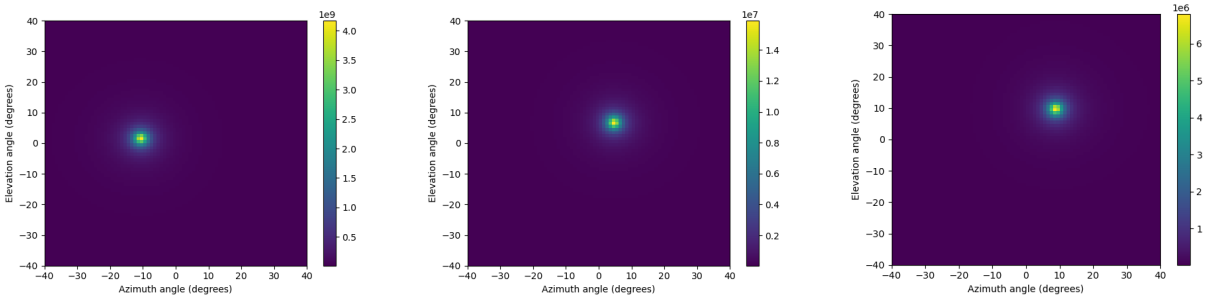

(a) Object A (b) Object B (c) Object C

Figure 19: Azimuth and elevation angles for three simulated objects

To show that the method also works for more challenging situations than three independent signals, a spatial complex but stationary object is simulated and shown in Figure 20. The spatial dimensions of the object vary but are close to each other, which makes the angles more difficult to detect. Both angle dimensions are estimated for the incoming signal by using the combined-angle version of the MVDR method. Figure 21 shows both angles for the object over variation in range. The shape of the object can be clearly seen in these angular plots. Next to that, although the entire object is simulated at equal strength, it can be seen that the signal strength degrades as the range increases. This is in line with the expectation, because signal strength in general degrades when it has to travel further.

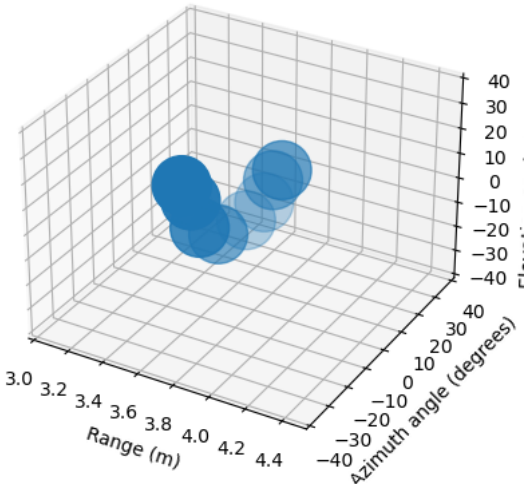

Figure 20: Visualization of more complex simulated object

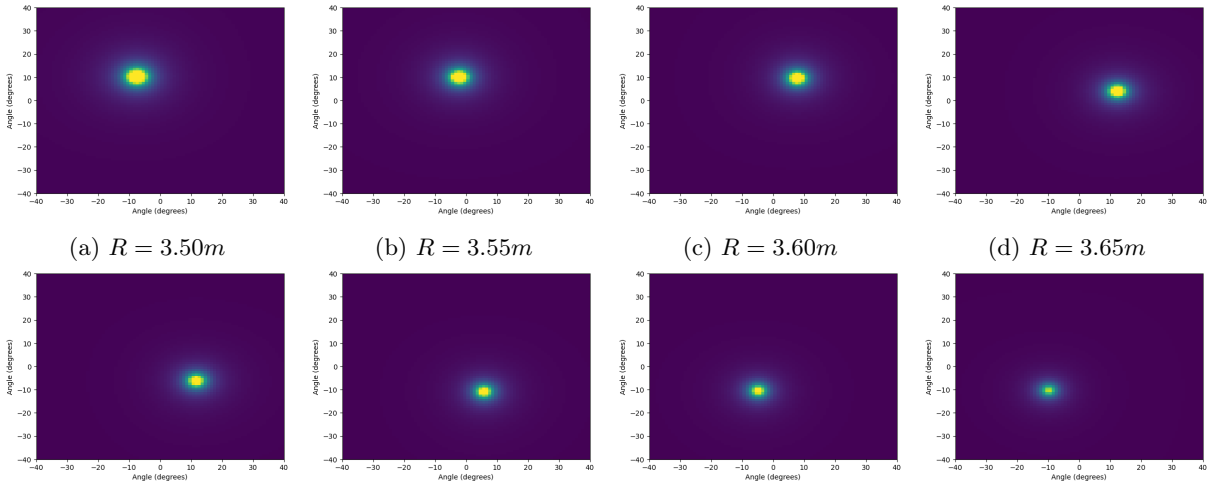

(a) $R = 3.50m$ (b) $R = 3.55m$ (c) $R = 3.60m$ (d) $R = 3.65m$

(e) $R = 3.70m$ (f) $R = 3.75m$ (g) $R = 3.80m$ (h) $R = 3.85m$

Figure 21: Azimuth and elevation angle over increasing range

3.2 Point Cloud Generation

The CFAR detection algorithm is performed on the three dimensions range, azimuth angle, and elevation angle separately. Only when all three thresholds are passed, presence is detected and that point is included in the cloud. Section 3.2.1 shows and discusses generated point clouds for the different CFAR interference estimators and varying parameters. Also the situation described in section 2.3 of incorrect combination of detector and scaling factor, is shown for the simulated signal. Next to that, section 3.2.2 proposes to add a post-processing step to improve point clouds in an informative way.

3.2.1 CFAR Detection

Figure 22 shows the generated point clouds for the three simulated objects from Table 1b, for CA-, SOCA-, GOCA-, and OS-CFAR. The number of guard cells n_G varies over the values 2, 4, and 8, while the number of training cells remains $n_T = 16$. The values n_G and n_T are the amount of guard and training cells on one side of the CUT, meaning that the entire reference and training windows consist out of $2(n_G + n_T)$ and $2n_T$ cells respectively.

The CA-CFAR plots of Figure 22 clearly show that when the number of guard cells is increased, the region of detection for each object is also increased. When there is a large amount of guard cells, a cell which lies in the weakening gradient of the actual signal can pass the threshold because the actual signal cells are excluded from the interference estimation. A higher amount of guard cells thus results in a larger region of detection as shown in Figure 22b, but may also result in masked objects. This is shown in Figure 22c, where object C is not detected. If the amount of guard cells increases, the entire reference window also enlarges. The azimuth angles of object B and C are close to each other, hence when the other object is covered in the reference window it will be included in the interference estimation. Because object B has a larger signal strength than object C, object C is masked by object B and will thus not be detected.

Where CA-CFAR detected three separate objects, for SOCA-CFAR and $n_G = 2$ in Figure 22d the signals of object B and C are merged into one larger region. Object B and C are closely situated, therefore the signals that lie in the weakening gradient regions of either of the two objects are detected as presence for SOCA-CFAR. The region detected for object A is also increased when looking at the azimuth angle, but due to its zero velocity not for the range dimension. Objects B and C have nonzero velocity, and their signal thus changes over range whereas object A is stationary. When the amount of guard cells is increased to 4 in Figure 22e, both object B and C are masked because the weakening of the strong signal of object A is included in the estimation.

When the amount of guard cells and thus also the reference window is increased even further as shown in Figure 22f, the regions of detection also increase. For a larger reference window, cells with a lower signal strength resulting from the weakening gradient of the objects are more likely to be detected as presence

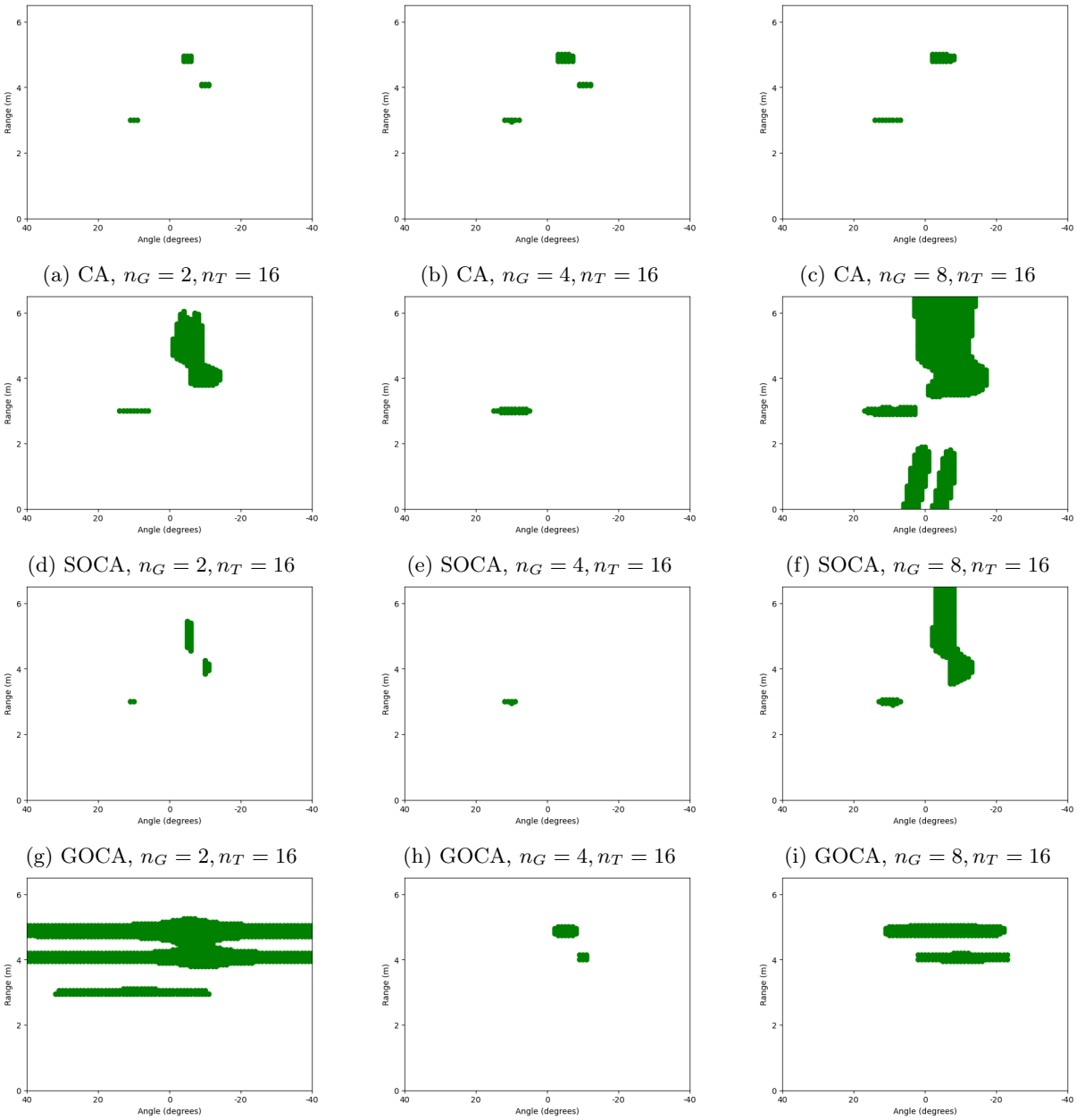

(a) CA, $n_G = 2, n_T = 16$ (b) CA, $n_G = 4, n_T = 16$ (c) CA, $n_G = 8, n_T = 16$

(d) SOCA, $n_G = 2, n_T = 16$ (e) SOCA, $n_G = 4, n_T = 16$ (f) SOCA, $n_G = 8, n_T = 16$

(g) GOCA, $n_G = 2, n_T = 16$ (h) GOCA, $n_G = 4, n_T = 16$ (i) GOCA, $n_G = 8, n_T = 16$

(j) OS, $n_G = 2, n_T = 16, k = 24$ (k) OS, $n_G = 4, n_T = 16, k = 24$ (l) OS, $n_G = 8, n_T = 16, k = 24$

Figure 22: CFAR point clouds for various interference estimators and varying number of guard cells n_G, for three simulated objects from Table 1b.

when there are no other objects nearby. The interference estimation is based on cells that lie further from the object, which results in a lower threshold and thus a higher chance of being detected. The two stripe-like detected regions are typical for SOCA-CFAR detection. Although there is no object simulated for these ranges, the low signal strength resulting from the other objects are detected as presence. There is a region where no presence is detected in the middle, because both halves of the reference window now contain stronger signals from the same region. For the detected stripes, one half contained low signals ans thus resulted in a low threshold.

As expected, GOCA-CFAR results in smaller detected regions than for the other two cell-averaging variants. When the amount of guard cells is increased to $n_G = 4$ in Figure 22h, objects B and C are masked because similar to the SOCA-CFAR variant in Figure 22e signals from other objects are included in the training window and thus the background interference estimation. Figure 22i shows that when there is a larger number of guard cells, cells nearby the objects are detected as presence because now the strong signals from the object are excluded and the threshold is lowered.

For the OS-CFAR generated point clouds for the three objects, the value k of three quarters of the training window is chosen. The different ranges of the three simulated objects are clearly detected in Figure 22j. When the amount of guard cells is increased for the OS-CFAR estimator variant as shown in Figure 22k, object A is not detected. Because object A has a stronger amplitude than the other two objects and does not change or range because it has zero velocity, its strong signal is centered at one location. Where object B and C have a lower amplitude which is also spread over a larger range, this leads to significantly lower signal strengths. The OS-CFAR estimator bases its statistically derived threshold on the weaker objects' signals, resulting in the strong signals from object A not being detected. In Figure 22l it is shown that when the amount of guard cells is increased even further, the region of detection increases because the training cells contain lower signal strength compared to the previous situation.

In section 2.3 the incorrect use of the linear law detector in combination with the scaling factor that belongs to the square law detector is covered. To show the differences in detection performance, the detection for the same simulated objects and sliding window parameters are shown in figures 23d, 23e, and 23f. When the square law detector is applied, the difference between weak and strong signals becomes larger and the edge is less gradual compared to the linear law. As can also be seen in Figure 23, more cells will be detected as presence, compared to the linear law.

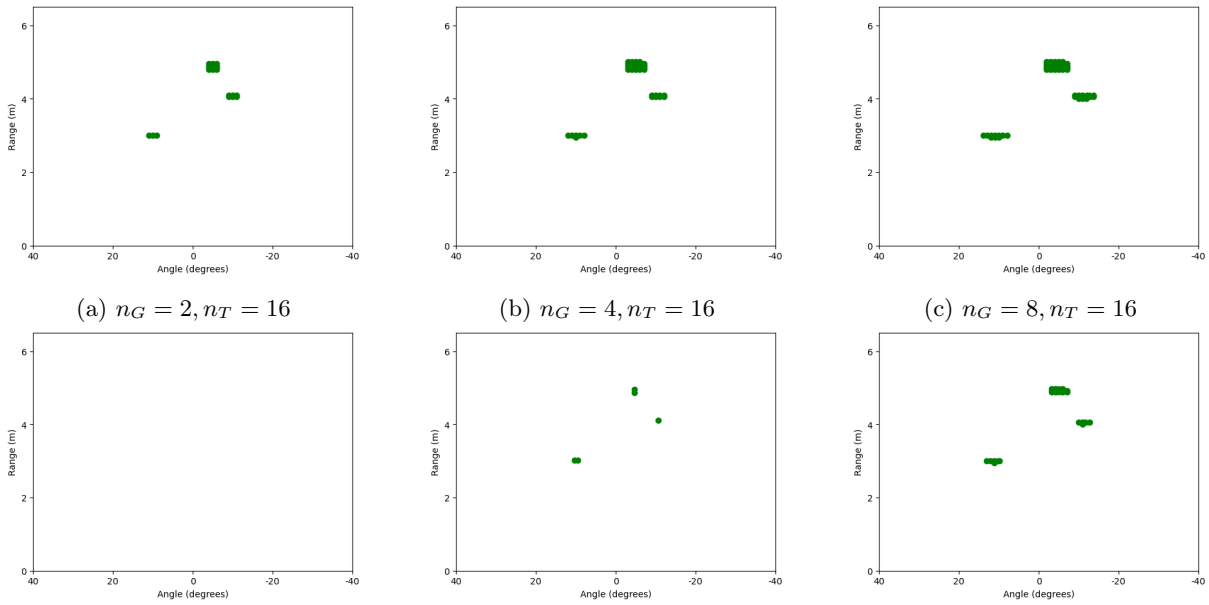

(a) $n_G = 2, n_T = 16$ (b) $n_G = 4, n_T = 16$ (c) $n_G = 8, n_T = 16$

(d) $n_G = 2, n_T = 16$ (e) $n_G = 4, n_T = 16$ (f) $n_G = 8, n_T = 16$

Figure 23: Detection for increase in number of guard cells, CA-CFAR. Correct use of square law detector in (a), (b) and (c), linear law detector in combination with incorrect scaling factor in (d), (e), and (f).

For the more complex simulated object from Figure 20, the point clouds for the CA-, SOCA-, GOCA-, and OS-CFAR interference estimators have also been generated for an increase in guard cells in Figure 24. The object of detection is not a signal coming from a single location, but covers a larger region over both range and azimuth dimension. Therefore having enough guard cells becomes of greater importance for correct detection. The CA-CFAR point clouds show that masking of itself takes place for a small amount of guard cells. In contrast to the three individual objects, more guard cells now do not result in masking because there are no other strong signals from for example other objects.

The SOCA-CFAR estimator results in similar but slightly larger point clouds, the region nearby the object is also detected. For a small amount of guard cells, the interference estimation always includes signals from the object itself. For the GOCA-CFAR estimator and $n_G = 2$ in Figure 24g, only the cell belonging to the strongest signal is detected. Increasing the number of guard cells to $n_G = 4$ leads to increased detection performance, whereas too many guard cells lead to the same false detection phenomena as explained for Figure 22f and 22i.

The OS-CFAR interference estimator has been designed for combined clutter-edge and multiple object situations, however this simulated situation contains neither of the two. Hence for this easy situation but with a more complex object, using the OS-CFAR estimator does not result in good detection performance.

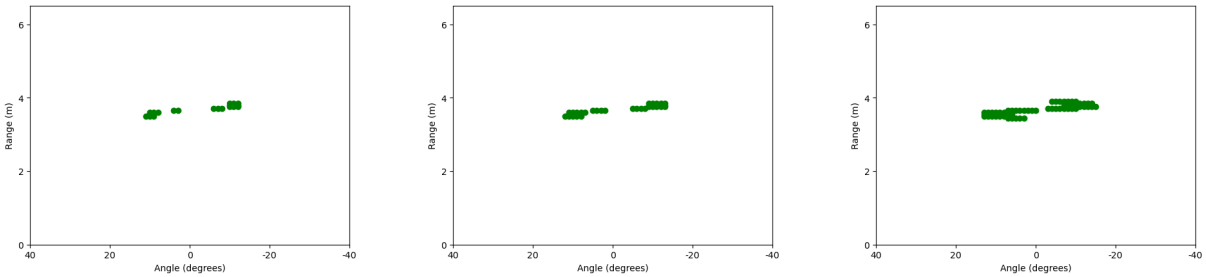

(a) CA, $n_G = 2, n_T = 16$ (b) CA, $n_G = 4, n_T = 16$ (c) CA, $n_G = 8, n_T = 16$

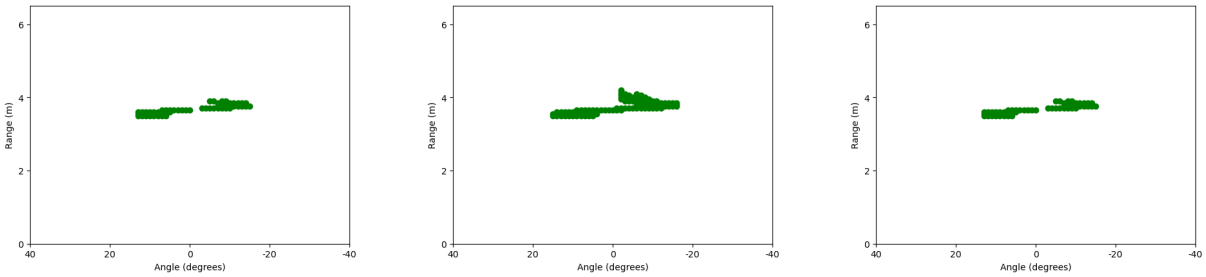

(d) SOCA, $n_G = 2, n_T = 16$ (e) SOCA, $n_G = 4, n_T = 16$ (f) SOCA, $n_G = 8, n_T = 16$

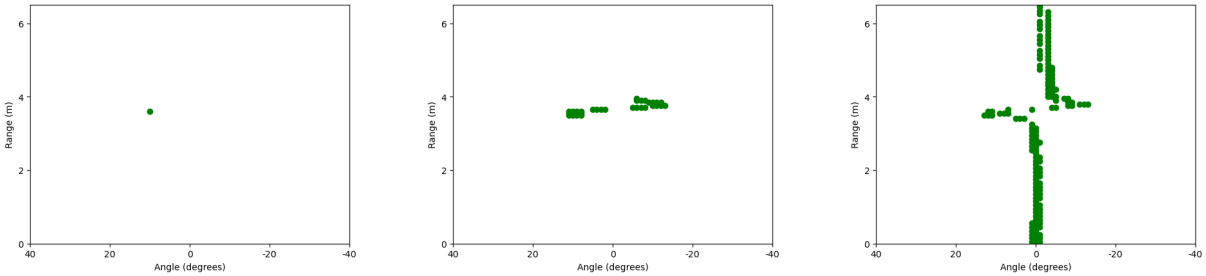

(g) GOCA, $n_G = 2, n_T = 16$ (h) GOCA, $n_G = 4, n_T = 16$ (i) GOCA, $n_G = 8, n_T = 16$

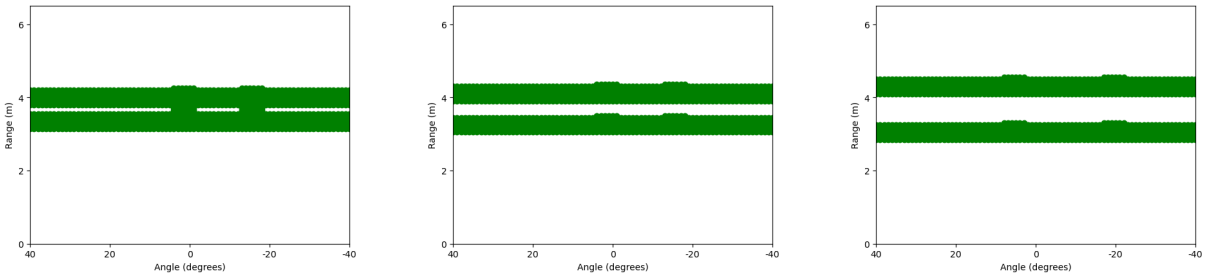

(j) OS, $n_G = 2, n_T = 16, k = 24$ (k) OS, $n_G = 4, n_T = 16, k = 24$ (l) OS, $n_G = 8, n_T = 16, k = 24$

Figure 24: CFAR point clouds for various interference estimators and varying number of guard cells n_G, for more complex simulated object from Figure 20.

For this specific situation having $k = \frac{3}{4}$ is too low, and results in the region surrounding the simulated object in being detected. The centre of the object is not detected because the k for those cells include signals from the object itself. When the amount of guard cells is further increased, the outer borders of the detected band get wider because the value of the kth signal is lower. At the same time the undetected band in the middle also increases.

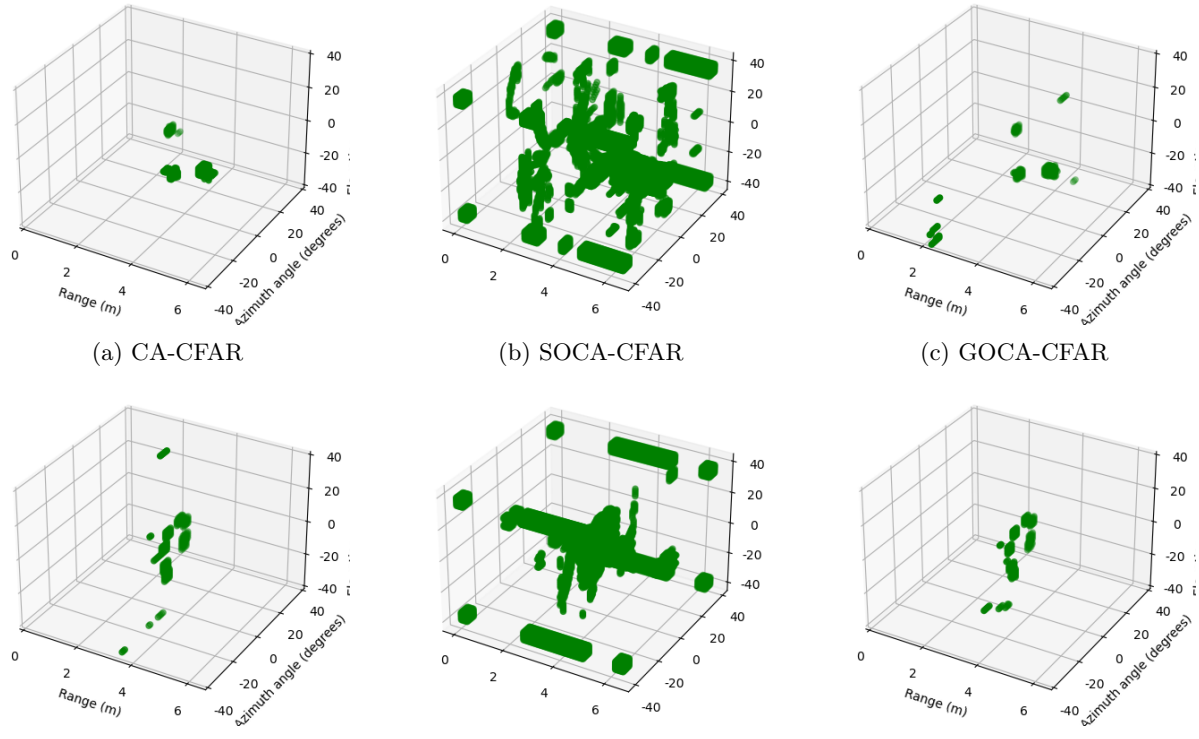

(a) CA-CFAR (b) SOCA-CFAR (c) GOCA-CFAR

(d) CA-CFAR (e) SOCA-CFAR (f) GOCA-CFAR

Figure 25: 3D figures for CFAR detection with $n_G = 4, n_T = 16$, for three simulated objects in Figures 25a, 25b, and 25c, and a more complex simulated object in Figures 25d, 25e, and 25f.

Until now the generated point clouds have been shown as two-dimensional representations, however they can easily be computed over three dimensions as well. Figure 25 shows the three dimensional generated point clouds for both the three separate object simulation and the more complex object situation. It can be seen that for both simulations the point clouds generated with the GOCA-CFAR estimator result in fewer points, whereas usage of the SOCA-CFAR estimator results in a larger amount of points detected. The point clouds generated for the OS-CFAR estimator result in zero detections, and are therefore not included in the figure.

3.2.2 Informatively Improved Point Clouds

As shown in section 1.2 and Figure 2, mmWave radar point clouds are sparse compared to LiDAR point clouds [46]. Radar sensors deal with specular reflections from surfaces, in contrast to light waves which scatter in every direction and are thus also reflected back to the sensor [3]. The point clouds are usually too sparse for classification and recognition applications in the automotive industry [34]. In fact, radar point clouds are in general not good at capturing a detailed shape of an object [3]. A trivial approach to increase the density is interpolation [35]. Current research focuses on more informative ways to improve the generated mmWave point clouds, by increasing the number of points and the accuracy [81].

This gives reason to propose to include an extra step in the general detection procedure, which eventually results in more informative point clouds. What features are of added information, is dependent on the application the point cloud will be used for. However, there are more informative ways than interpolation to include extra information in the point cloud, by actually using the data already gathered and computations made. Next to the number of points and density of the clouds, there are other possibilities to informatively improve point clouds. The reflected signal strength of the detected points seems obvious as added information, but might also give a distorted picture. The signal strength is dependent on a combination of many different factors, for instance the object's material, range, orientation, and multipath effects caused by itself and other objects [50].

A possible way to store more information in point clouds, is to include the CFAR results over each dimension separately. In the ordinary procedure only the points which are detected over the range, azimuth, and elevation dimension are included in the point cloud. Situations where the threshold of

only one dimension has not been passed may include useful information on the shape of the object to be detected. To analyse the effects of this proposed added informative step, it has been included in the implementation.

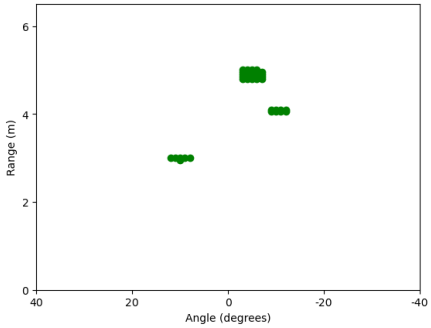

(a) Detection over both dimensions

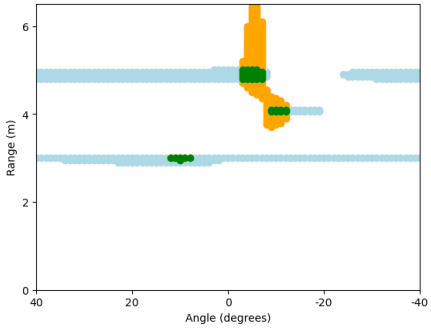

(b) Detection over azimuth (orange) and range (blue) separately, and both (green).

Figure 26: CA-CFAR detection over the 2D range-azimuth plane for three simulated objects

Figure 26 shows the ordinary generated point cloud in the range-azimuth plane in 26a, and the proposed informatively improved version in 26b. The proposed point cloud does not directly seem to add useful extra information.

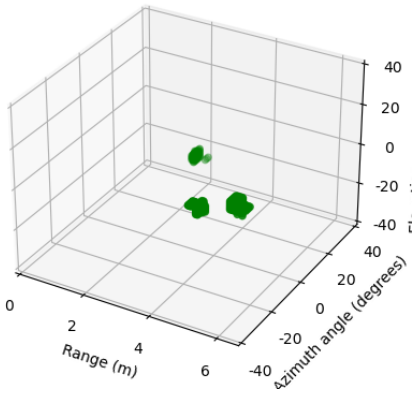

(a) Range, azimuth, and elevation

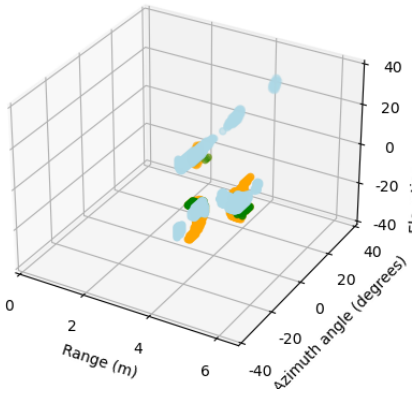

(b) Range and azimuth (orange), range and elevation (blue), and over all three dimensions (green).

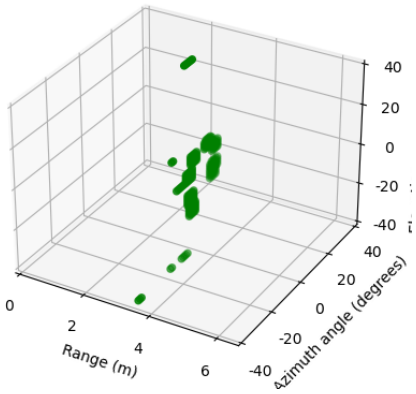

(c) Detection over all three dimensions

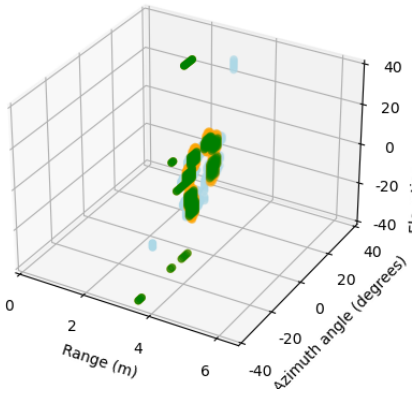

(d) Separate

Figure 27: CA-CFAR for the simulated situations in 3D

Figure 27a shows the 3D generated point cloud for the three simulated objects and its proposed informatively improved point cloud in Figure 27b. It includes the individual point clouds for when either the azimuth or elevation angular dimension have been excluded from the detection. Figures 27c and 27d show the original 3D point cloud and its informatively improved version for the more complex simulated object from Figure 20. For the three simulated objects, if only the improved point cloud were provided it would not become directly clear where the regions of the original detected point cloud are. Parts of the green point cloud are hidden by the other two. For the simulation of the more complex object this does not form a problem, but this could not have been known beforehand. Therefore it is advised to not solely rely on the point cloud resulting from this proposed post-processing step, but to view it as an addition to the ordinary point cloud output.

4 Experiment

This chapter discusses the experiment, from the design in section 4.1 to the results and analysis of the conducted measurements in section 4.2. To test the performance of the different CFAR interference level estimators in realistic living rooms, a novel experiment had to be set up. The variables and choices made regarding which properties to focus on and which to minimize the influence of, are elaborated on in section 4.1.1. The set-up is described in section 4.1.2, including the radar sensor board that is used as well as the layout of the rooms the experiment is performed in.

The weight of this chapter lies with the obtained results, for which the data processing framework as described in chapter 4 for the simulations is used. Hence the same angle detection method is used, and the CFAR interference level estimators that are included are CA-, SOCA-, GOCA-, and OS-CFAR. The reflected signal strengths are shown for different situations and rooms in section 4.2.1. Section 4.2.2 includes and discusses the point clouds generated for the different rooms, situations, and different interference level estimators. Furthermore, the informatively improved point clouds proposed in section 3.2.2 have been generated for the experimental data as well and are shown and elaborated on in section 4.2.3. How this chapter and covered objective relates to the general process from radar to application, is shown in Figure 28.

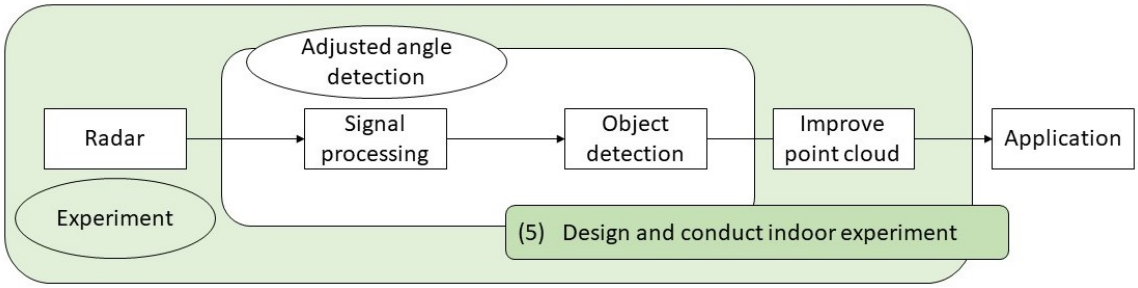

Figure 28: Relation between this chapter, the covered research objective covered, and the general process from radar to application.

4.1 Experiment Design

The background for indoor situations is different than outdoors, the ratio of objects compared to background is very large. Therefore it is not certain if performance of CFAR interference level estimators remain the same for this different kind of environment. The expectation is that estimators which have degraded performance in multi-object situations will also not perform very well in realistic living rooms, but this has not yet been looked into. Therefore a systematical procedure is created and performed, which focuses on the detection performance of the different CFAR background interference level estimators in a realistic living room environment.

4.1.1 Variables

Living rooms are completely different from each other, they may vary with respect to many characteristics and properties. Certain properties are likely to effect the reflection of signals and thus may also influence the detection performance. For instance the shape, size, and building materials pf the room directly relate to multipath effects. To limit this variation, the experiment is conducted in rooms of the same shape and size and in the same buildings. The measurements are performed at van Boeijen, which is an organisation for people with intellectual disabilities. Their location in Assen includes several buildings with similar rooms, where residents have their own studio.

Just like ordinary living rooms, the interior of these studios differ a lot. The two properties with respect to the interior that are focused on during this experiment, are how filled the room is and the amount of strong reflectors. A highly occupied room may cause for more complex situations regarding multiple objects. Whereas a high amount of strong reflectors may cause difficulties by masking other objects. Both properties are evaluated objectively for each room, by letting three individuals fill out a small questionnaire categorizing all rooms.

Next to the interior of the room, is the situation and occupancy by people also of interest. Therefore

five variations in movement activity are tested in each room, from zero movement to multiple movements close to each other. The five movement situations are described as the following:

1. **No movement**: No person present.
2. **Large scale movement**: Person walks through the room (> 1m).
3. **Small scale movement A**: Vertical arm movement (< 1m).
4. **Small scale movement B**: Horizontal hand movement (< 0.3m).
5. **Small scale movements combined**: Small scale movements A and B in front of each other.

Figure 29: Movement situations 3 (L), 4 (M), and 5 (R).

During the recording of the room without anyone present, the background signals are measured which themselves also belong to objects. From this it can be evaluated whether the furniture can be clearly detected. Additionally, evaluation of the large scale movement of a person walking through the room may provide insights regarding the detection performance at different locations within the room.

The small scale movements 3, 4, and 5 are visualized in Figure 29. Movement situation 3 varies over the azimuth and elevation angle, the range movement is limited. Movement situation 4 varies over the range, whereas movement over both angles is limited. By including these different movement situations, difference in performance caused by movements over different spatial dimensions may also be observed. By including the combined movement situation 5, movements which cross paths can be evaluated.

4.1.2 Set-up

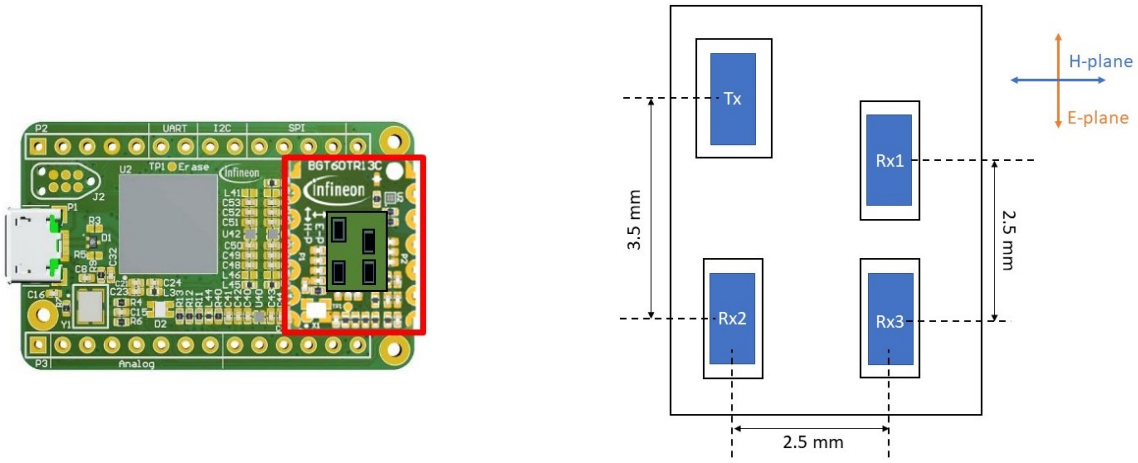

Figure 30: Infineon BGT60TR13C radar sensor [30], and details of the antenna positions

For this experiment an Infineon BGT60TR13C XENSIV 60GHz radar sensor has been used. Figure 30 shows the mmWave radar, in the red square. The rest of the board is required such that the information can be read via a USBC connection. Next to it is a zoomed in representation of the antennas on the mmWave radar. When the radar board is oriented as in the figure, the maximum azimuth angular range is 80°, and the elevation angle has a maximum range of 50°. The region of interest for this experiment is

more focused on the centre and close to the floor, than towards the ceiling. Therefore this orientation of the radar is preferred. However, when the focus lies on the entire elevation angle and the azimuth plane is limited, the radar should be rotated resulting in exchanged elevation and horizontal-planes.

For reference a depth camera has been mounted on top of the mmWave radar, the Intel Realsense D455 has been used for this. As can be seen from Figure 31, it does not capture colour as an ordinary camera, but the distance. Both sensors together are placed on a tripod at a height of 1.5m in the corner of each room, located at the green marker in Figure 32. The tripod is directed into the room such that most of the room is included in the 80° azimuth angle.

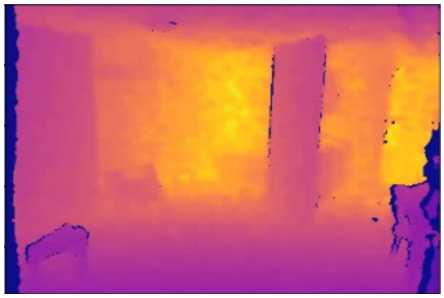

(a) Movement situation 1, no presence.

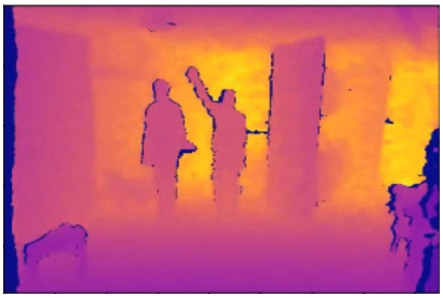

(b) Movement situation 5, combined movements.

Figure 31: Depth camera images of Intel Realsense D455

The movement situations happen at the same location within one room. As mentioned before, multipath effects can be caused by the walls, hence the positioning with respect to them matters. Not every room has an empty spot in the exact same location, therefore the location of movement activities differs per room and is noted. Similar to the positioning within the room, characteristics of the person performing the movements may also be of influence. Therefore it is noted who performs each movement including their features of interest with respect to reflecting signals, such as wearing a large watch or a belt with a big buckle.

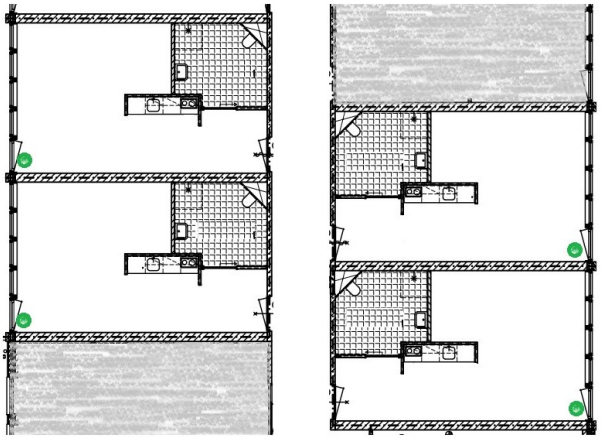

Figure 32: Map of a building at Van Boeijen [7], including the sensor setup location marked in green

4.2 Results and Analysis

The radar parameters from Table 1a are used, which are the same as used for the simulations in the previous Chapter. This leads to a maximum range of 6.5m, therefore the figures include only results up till this distance. The maximum angles are defined as twice the half-power beam widths, and are dependent on the antenna design and their beam patterns. For this sensor this leads to the maximum detection angles $\theta_{az} = 80°$, and $\theta_{el} = 50°$ for the azimuth and elevation angles respectively.

4.2.1 Detected Signal Strengths

Figure 33 shows the difference signal strength polar plots of the range and azimuth angle. The signal strength of the no presence situation is higher for the room with a fuller interior in Figure 33b, than for the almost empty room in Figure 33a. The objects in the more crowded room lead as expected to detected strong reflections at closer ranges compared to the room with less furniture. Figure 33c shows the detected signal strengths for one person present in the almost empty room, and shows a clearer signal at a range of 3.5m which was not there before. When two people are present, as shown in Figure 33e, this can also be clearly detected from the stronger reflections detected within the range of 3.5 to 4m. For the room with a lot of furniture and objects, Figures 33d and 33f also show the situation of respectively one and two persons present. Presence and absence of people is visible from the plots, but the difference is less large because the ratio of number of reflections changes less compared to the room with an almost empty interior.

Additional plots of the detected signal strengths, including plots for the elevation angle and other rooms, can be found in Appendix A.1.

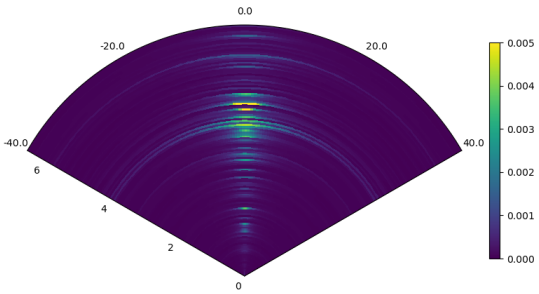

(a) Empty interior, no presence

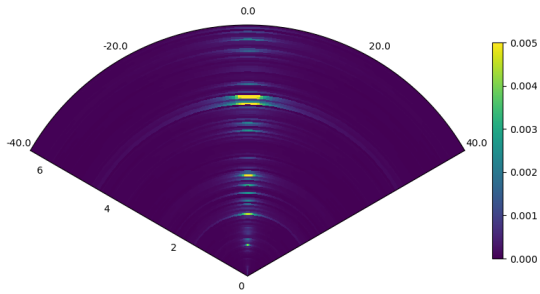

(b) Full interior, no presence

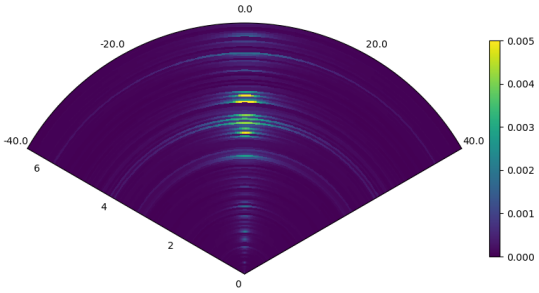

(c) Empty interior, one person

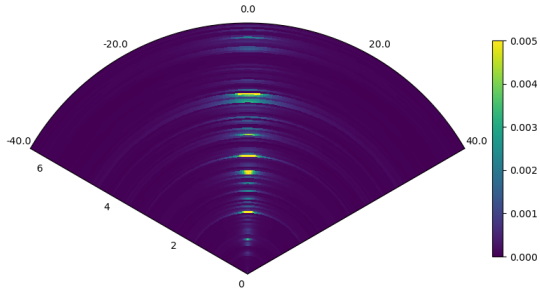

(d) Full interior, one person

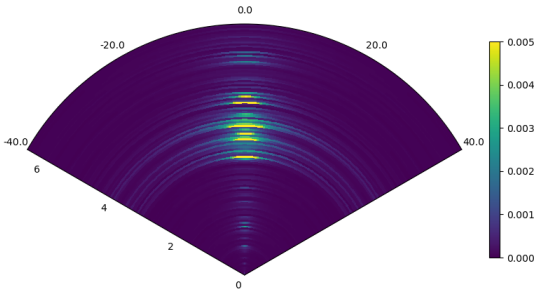

(e) Empty interior, two people

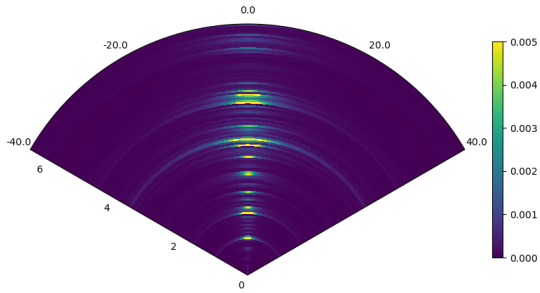

(f) Full interior, two people

Figure 33: Range-azimuth plots for different presence situations for a room with an empty interior and almost no strong-reflecting materials, and for a room with a full interior and a lot of strong-reflecting materials.

4.2.2 Point Clouds for Variations of Interference Estimators

Point clouds have been generated for each of the five movement situations in all of the thirteen individual rooms, using the CA-, GOCA-, SOCA-, and OS-CFAR interference estimators. The most interesting figures are discussed and included in this section, additional figures may be found in Appendix A.2. The point clouds have been generated for $n_G = 4$ guard cells and $n_T = 16$ training cells on each side.

Figures 34, 35, and 36 show the generated point clouds for the three background interference level estimators CA-, GOCA, and SOCA-CFAR for three consecutive frames in. Focus lies on the differences and comparisons of the three small scale movement situations, the arm and hand movements and their combination. The interval between two frames is equal to the chirp repetition time T_c of 750 μ s, which is less than a millisecond. Although there is only a small period of time between the consecutive frames, the point clouds differ per frame for every estimator variant used. The OS-CFAR estimator point clouds have also been generated, but lead to empty point clouds and are therefore not included in the figures.

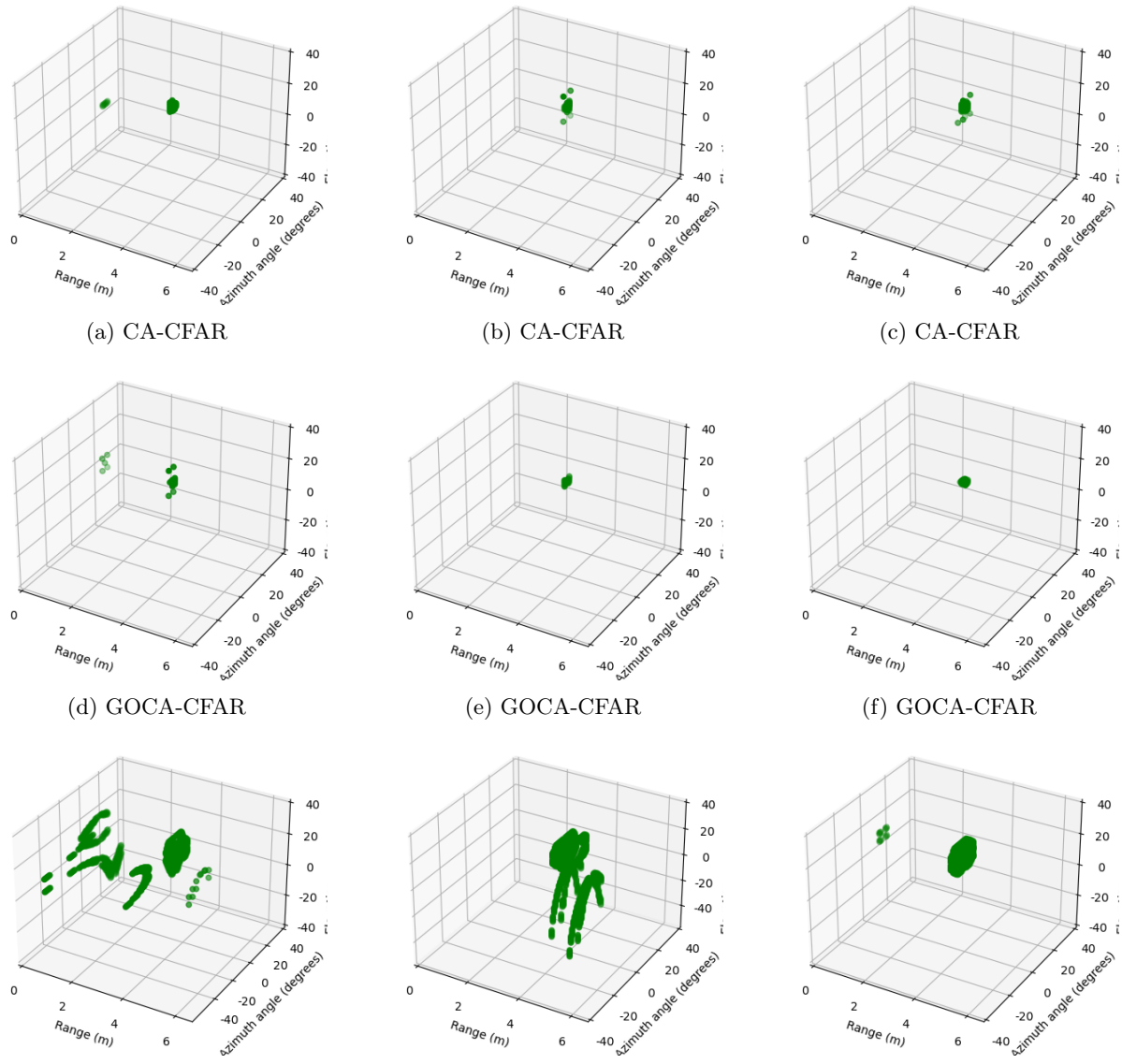

(a) CA-CFAR (b) CA-CFAR (c) CA-CFAR

(d) GOCA-CFAR (e) GOCA-CFAR (f) GOCA-CFAR

(g) SOCA-CFAR (h) SOCA-CFAR (i) SOCA-CFAR

Figure 34: Point clouds for CA-, GOCA, and SOCA-CFAR for the same three consecutive frames. One person present in the room, small scale arm movement, almost empty interior and minimal strong-reflecting materials.

The small scale arm movement is shown in Figure 34, and the differences between the interference estimator variants is shown. The SOCA-CFAR estimator leads as expected to more points than the other two. The CA- and GOCA-CFAR estimators lead to smaller but similar point clouds, where the GOCA-CFAR point clouds have a smaller number of points than the CA-CFAR point clouds. Where the SOCA-CFAR point cloud changes a lot over the frames, one part is consistently detected at the same location. This is the larger cloud in Figure 34i, which also corresponds to the location of the point clouds of the other estimators. For both CA- and GOCA-CFAR, in the first frame points are detected nearby the sensor which, belong to something else than the person making the movement.

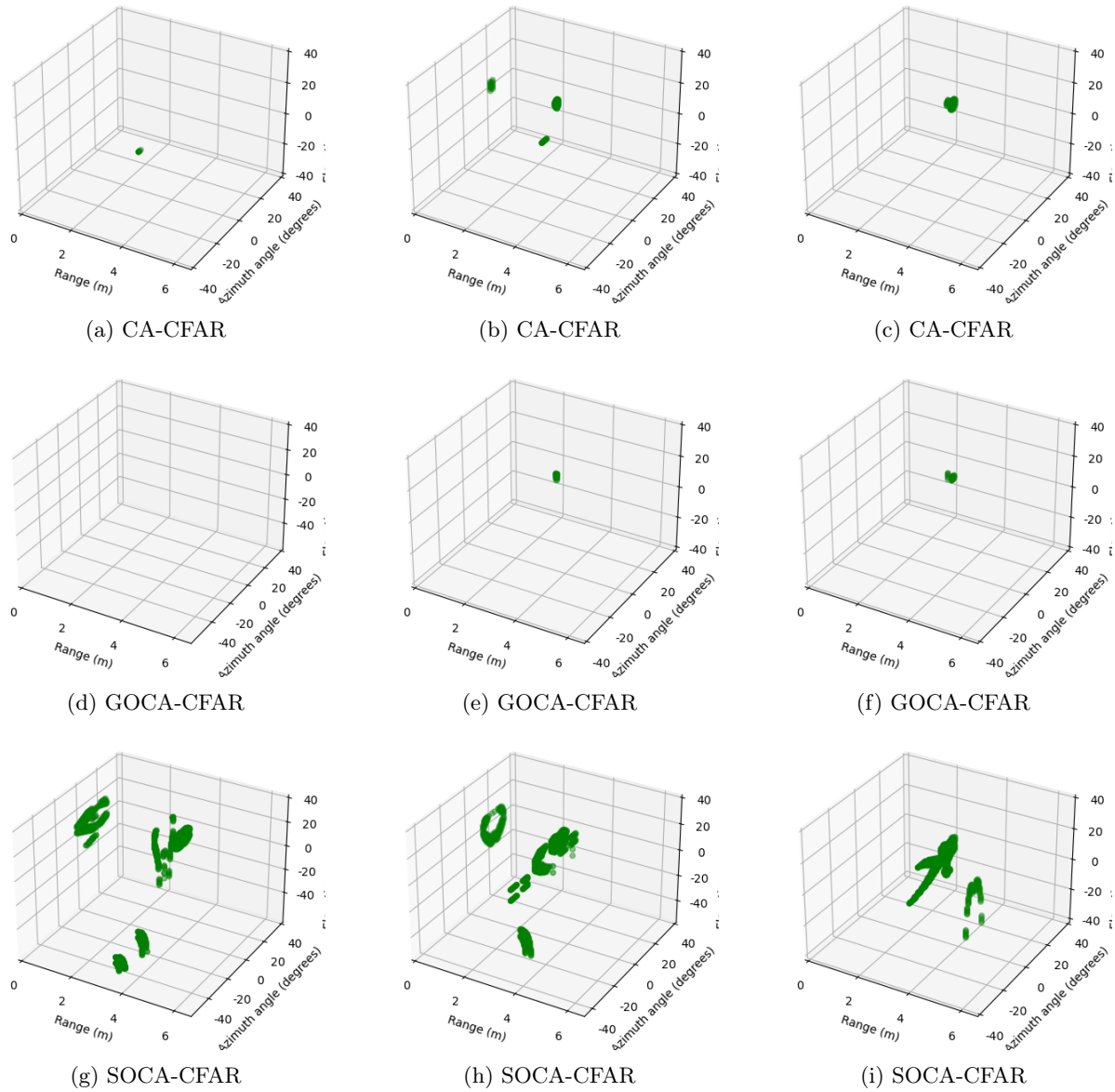

(a) CA-CFAR (b) CA-CFAR (c) CA-CFAR

(d) GOCA-CFAR (e) GOCA-CFAR (f) GOCA-CFAR

(g) SOCA-CFAR (h) SOCA-CFAR (i) SOCA-CFAR

Figure 35: Point clouds for CA-, GOCA, and SOCA-CFAR for the same three consecutive frames. One person present in the room, small scale hand movement, almost empty interior and minimal strong-reflecting materials.

Comparing the hand movement point clouds in Figure 35 to the arm movement point clouds of Figure 34, it can be seen that the smaller hand movement lead to a smaller number of points. Furthermore, where the arm movement had a constant part in the point clouds over the different frames and estimator variants, this is not the case for the hand movement situation. The point clouds over each frame are very different. The location of the CA-CFAR cloud in Figure 35a is not included in the other two frames, and only one of the three sub-clouds of Figure 35b is included in the cloud of Figure 35c.

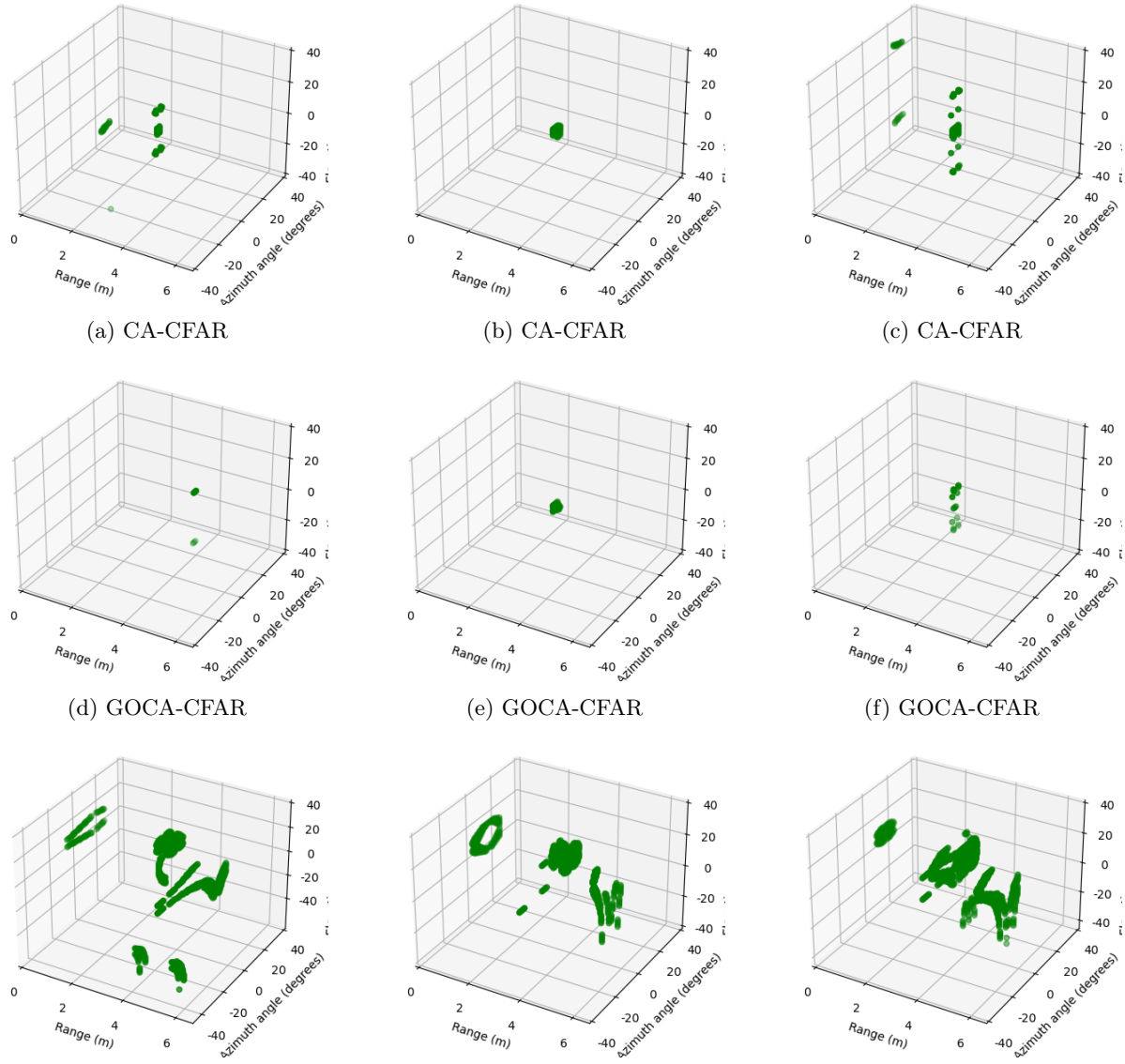

(a) CA-CFAR (b) CA-CFAR (c) CA-CFAR

(d) GOCA-CFAR (e) GOCA-CFAR (f) GOCA-CFAR

(g) SOCA-CFAR (h) SOCA-CFAR (i) SOCA-CFAR

Figure 36: Point clouds for CA-, GOCA, and SOCA-CFAR for the same three consecutive frames. Two people present in the room, small scale arm and hand movements combined, almost empty interior and minimal strong-reflecting materials.

Figure 36 shows the generated point clouds for the two small scale movements combined, and thus two people present. However, when comparing the point clouds to Figures 34 and 35, it does not necessarily become clear that the amount of people present has increased. Nonetheless, from the point clouds in Figures 36c and 36f, the shape of a human body could be deduced. Furthermore, for all three estimator variants, the point clouds change quite a bit over the frames. For the CA- and SOCA-CFAR estimators there is again a part of the point cloud which remains constant over the frames. However, this is not the case for the GOCA-CFAR estimator generated clouds.

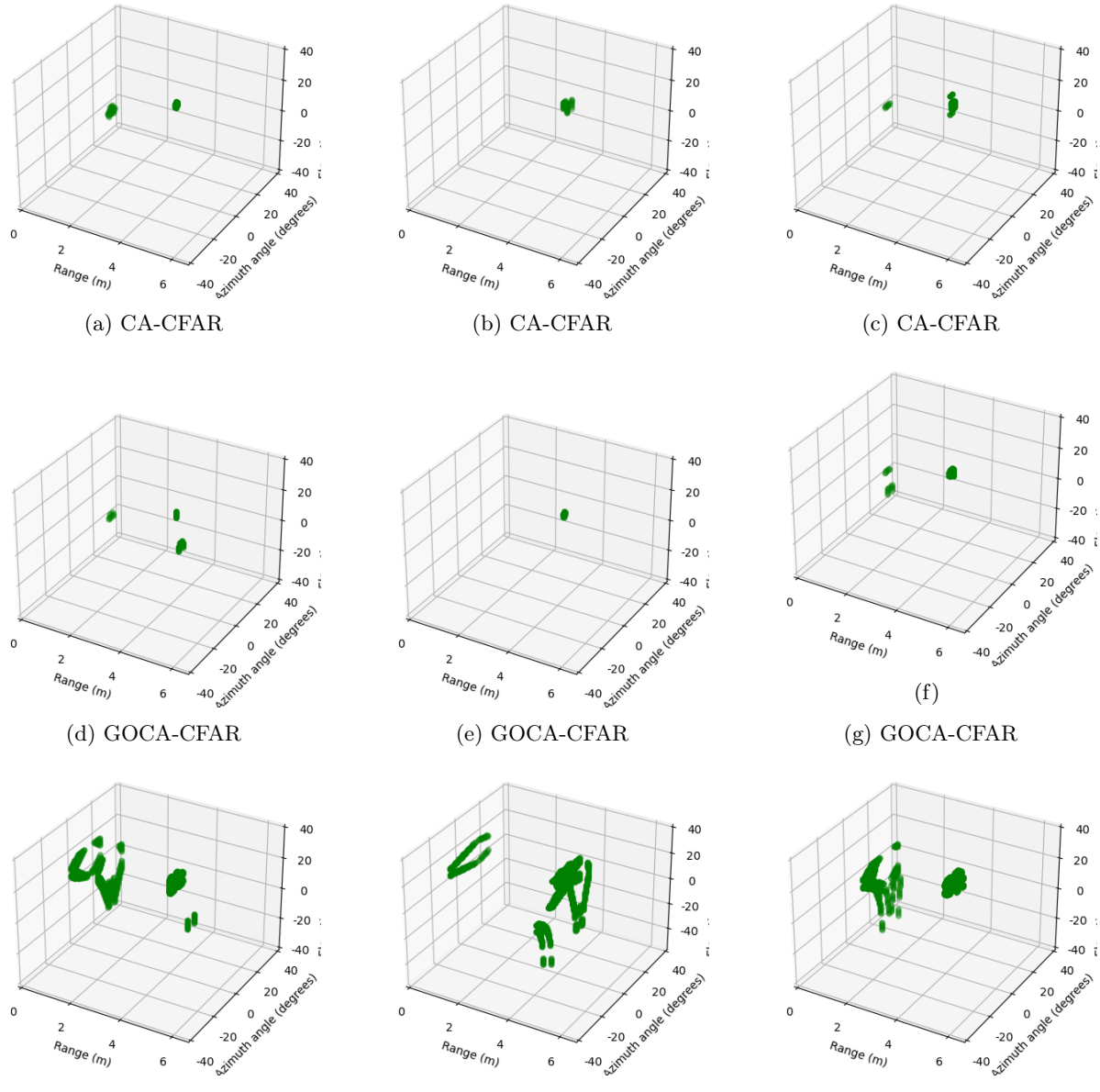

(a) CA-CFAR (b) CA-CFAR (c) CA-CFAR

(d) GOCA-CFAR (e) GOCA-CFAR (f) (g) GOCA-CFAR

(h) SOCA-CFAR (i) SOCA-CFAR (j) SOCA-CFAR

Figure 37: Point clouds for CA-, GOCA, and SOCA-CFAR for the same three consecutive frames. One person present in the room, small scale arm movement, full interior and many strong-reflecting materials.

Figure 37 shows the generated point clouds for the small scale arm movement, in a room with a full interior and a lot of strong-reflecting materials. The point clouds are similar to the ones generated for the same situation but in a more empty room, although these point clouds suggest the presence of a second object. This might be caused by any of the objects present in the room.

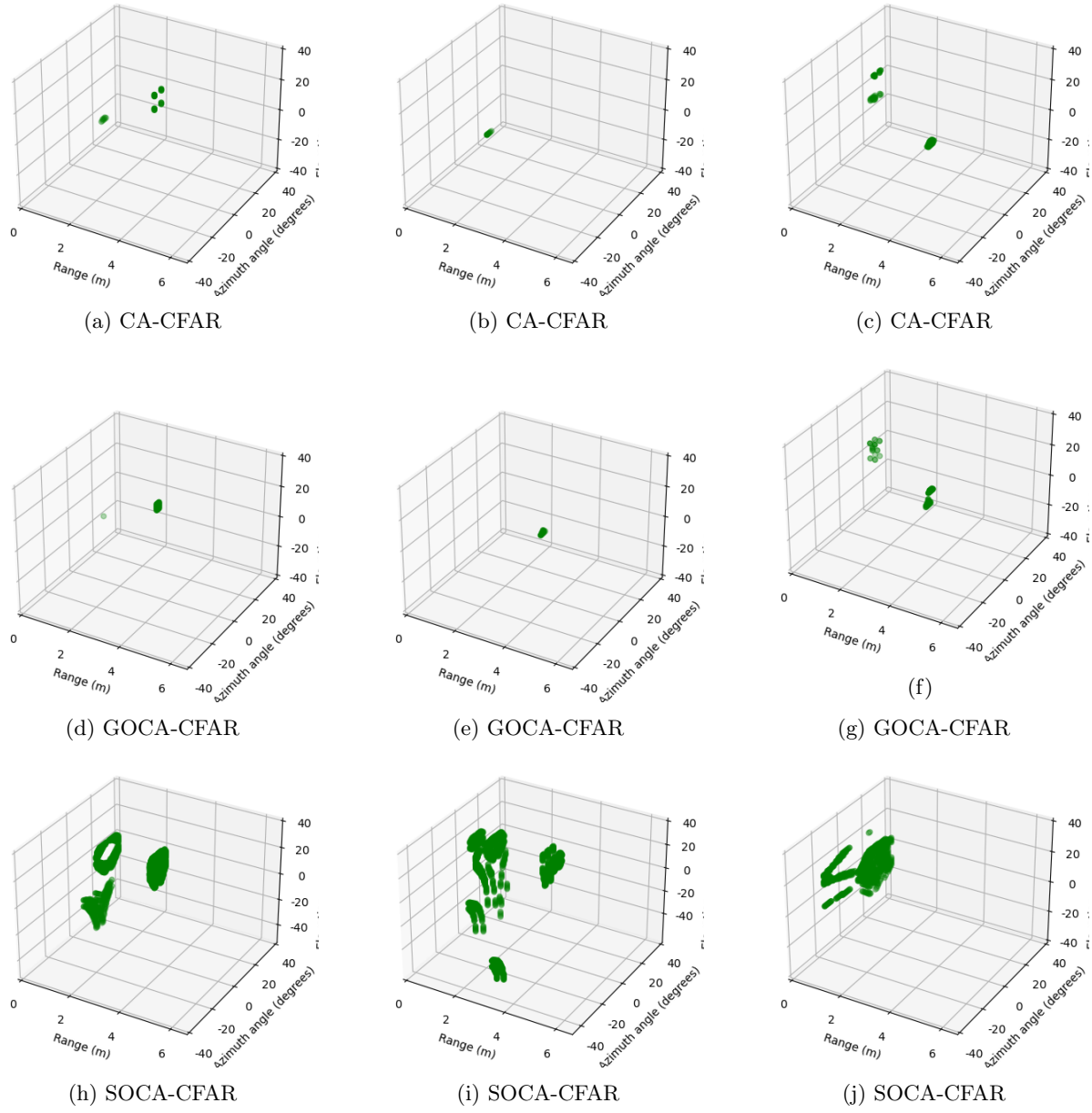

(a) CA-CFAR (b) CA-CFAR (c) CA-CFAR

(d) GOCA-CFAR (e) GOCA-CFAR (f) (g) GOCA-CFAR

(h) SOCA-CFAR (i) SOCA-CFAR (j) SOCA-CFAR

Figure 38: Point clouds for CA-, GOCA, and SOCA-CFAR for the same three consecutive frames. One person present in the room, small scale hand movement, full interior and many strong-reflecting materials.

Figure 38 shows the point clouds for the small scale hand movement, and leads again to less points compared to the arm movement situation in Figure 37 of the same room. This is similar to the relation that was seen between the same movement situations, but for the room with a more empty interior. When compared to this other room, measurements in the more crowded room lead to less points detected. This may be the result of furniture blocking the view between the sensor and the person. Another also quite likely possibility is that more signals from other objects are included in the reference window and thus result in a raised threshold.

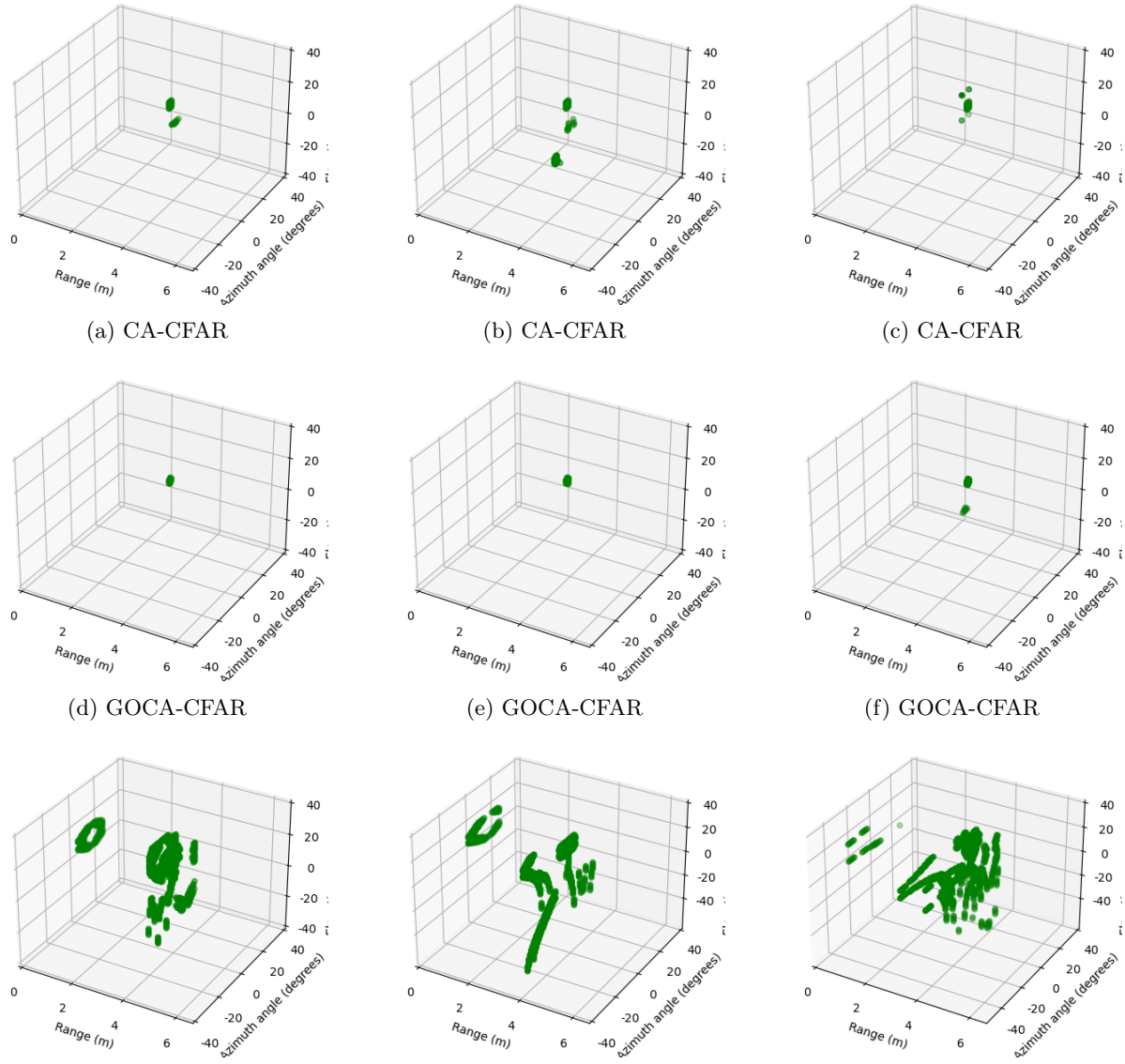

(a) CA-CFAR (b) CA-CFAR (c) CA-CFAR

(d) GOCA-CFAR (e) GOCA-CFAR (f) GOCA-CFAR

(g) SOCA-CFAR (h) SOCA-CFAR (i) SOCA-CFAR

Figure 39: Point clouds for CA-, GOCA, and SOCA-CFAR for the same three consecutive frames. Two people present in the room, small scale arm and hand movement combined, full interior and many strong-reflecting materials.

Looking at the point clouds generated for two people and the combined small scale movements as shown in Figure 39, the shape of the point clouds do not suggest an increase in presence when compared to Figures 37 and 38. The point clouds are similar to the two previously shown situations. Where the CA-CFAR plots of the similar situation but in the more empty room suggested a second location of presence in the room, this does not become clear from any of the estimator variations plots for this more crowded room.

To summarize the differences and comparisons regarding the point clouds generated for the different interference level estimators CA-, GOCA-, SOCA-, and OS-CFAR, it can be said that the CA- and GOCA-CFAR estimators result in comparable point clouds for almost every situation. The GOCA-CFAR estimator's point clouds generally include a fewer number of points than for the CA-CFAR estimator, but not in the same order of difference compared to the SOCA-CFAR estimator generated point clouds. The SOCA-CFAR estimated point clouds contain many points which also change over the different frames, and thus probably do not belong to the presence of an actual object. Therefore it can be said that although the SOCA-CFAR estimator has been developed to deal with detection in multiple target situations, it is not preferred in this setting.

Although the OS-CFAR estimator generated point clouds have not been included, their detection performance should not be forgotten. A highly possible reason why the OS-CFAR generated point clouds result in the detection of zero points, because inside a living room there are many reflected signals received by the sensor, setting k to $\frac{3}{4}$ may result in a too high threshold.

Furthermore, for the more empty room with almost no strong-reflecting materials present from Figures 34, 35, and 36, the combined movement situation resulted in larger point clouds. For the room with a more full interior and many strong-reflecting materials from Figures 37, 38, and 39, this is the other way around and the combined movement situation results in smaller point clouds.

4.2.3 Proposed Informative Improvement

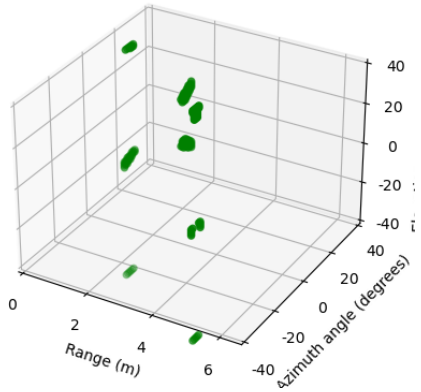

(a) Empty interior, original point cloud

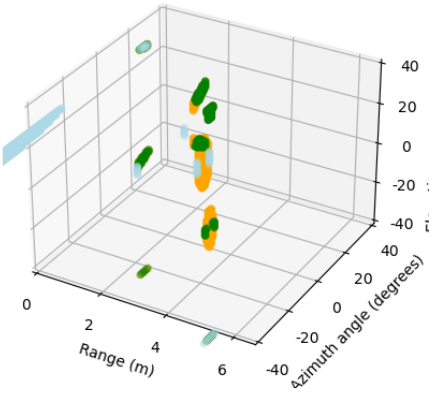

(b) Empty interior, improved point cloud

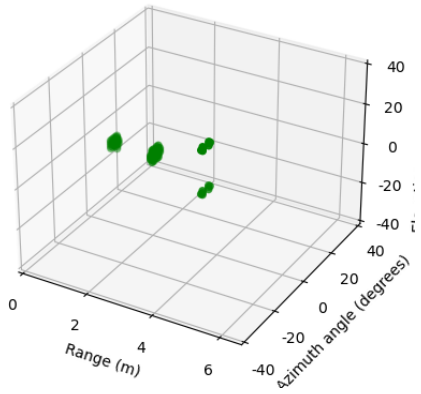

(c) Full interior, original point cloud

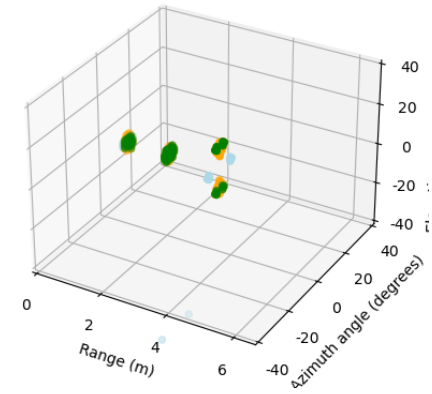

(d) Full interior, improved point cloud

Figure 40: Original point clouds and their informative improved versions for CA-CFAR estimator detection, small scale hand movement. (Top: Almost empty interior and minimal strong-reflecting materials, bottom: full interior and many strong-reflecting materials.)

Figure 40 shows the original and informatively improved point clouds as described in section 3.2.2, for the small scale hand movement and two different room situations. From the original point cloud in Figure 40a, the shape of a human body is difficult to derive. However, the improved point cloud in Figure 40b does suggest the shape of a body and thus provides more information to the original point cloud.

Figure 40d also provides more information to the original point cloud of Figure 40c. The improved point cloud suggests that the two pair of dots at same azimuth angle and range but different elevation angle, belongs to the same object. This object is the person standing in the room, nevertheless this would have been hard to determine from the original point cloud. Furthermore, Figure 40 clearly shows that rooms with a more full interior lead to less points detected in their point clouds, compared to the larger number of points included for more empty rooms.

Figure 41 shows the original and improved point clouds for the same situation of the combined small scale hand and arm movements, in a room with almost empty interior and minimal strong-reflecting

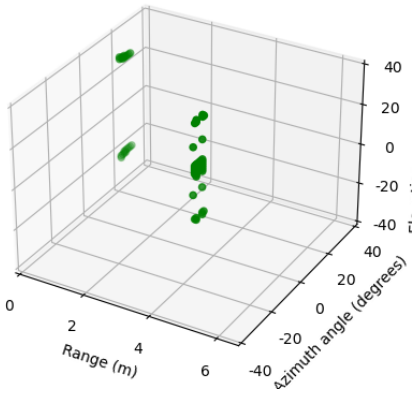

(a) CA-CFAR, original point cloud

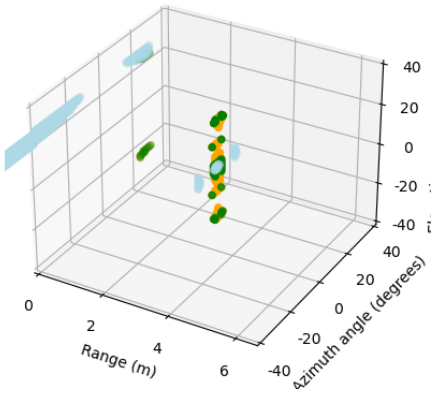

(b) CA-CFAR, improved point cloud

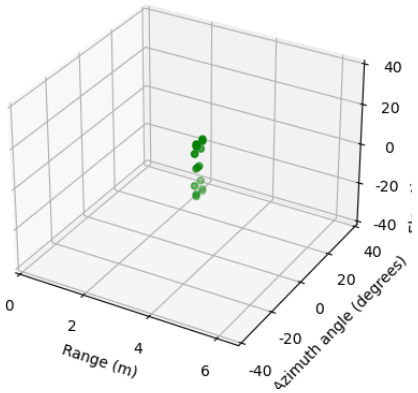

(c) GOCA-CFAR, original point cloud

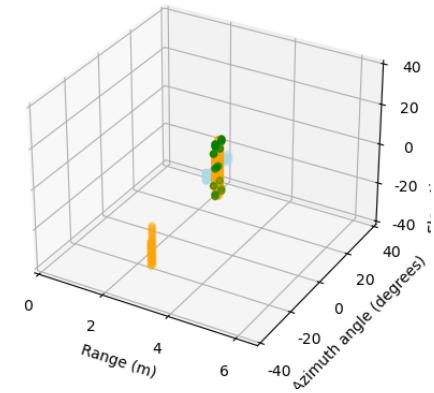

(d) GOCA-CFAR, improved point cloud

Figure 41: Original point clouds and their informative improved versions for small scale hand and arm movements combined in an almost empty interior and minimal strong-reflecting materials. (Top: CA-CFAR estimator, bottom: GOCA-CFAR estimator.)

materials present. The differences between the CA-CFAR and GOCA-CFAR estimator can be seen, for both estimators the improved point clouds provide additional information to the original point clouds. Figure 41d suggests the location of the second person in orange, which is at the same azimuth angle and range as the separate part of the point cloud in Figure 41a and 41b. Although the second person in the room is not directly apparent from the original point clouds or the individual improved point clouds, combining the information from the improved point clouds for different interference estimators may provide an even more complete picture of the actual situation in the room.

5 Discussion and Future Research

Current mmWave point clouds have their limitations, and indoor detection results in multiple difficulties. Hence before mmWave radar sensors can be used in an actual device for monitoring patients, the detection process needs to become more robust. With this in mind, the five research objectives of this thesis had been determined. This chapter discusses these objectives, draws conclusions and makes suggestions for future research regarding the specific topics.

Using adaptive thresholds from the CFAR method for object detection is the most common procedure to generate point clouds from radar signals. However, a complete overview including all steps and their variations, their interdependent relations, or assumptions the computations are based on is missing. The information is spread over multiple articles, papers, and educational books. By gathering and structuring all this information, this thesis provides a clear and complete overview of the CFAR object detection method.

Not only the steps and their computations are included, but also the theory behind the method. The detector operated over the data influences computations in following steps, similar for whether a Gaussian or non-Gaussian distribution of the background interference is assumed. Together with the choice of interference estimator used, these three factors determine how the probability of false alarm should be computed to maintain a constant false alarm while optimizing the probability of detection. From this false alarm rate a scaling factor is computed that is incorporated in the hypothesis test. The detection by hypothesis test relies on the Neyman-Pearson Lemma, which is explained and its proof is provided.

The scaling factor is directly related to the probability of false alarm, and thus also dependent on the detector, assumed interference distribution, and estimator used. Due to lack of information on the interdependent relations of these steps, combinations of detector and incorrect corresponding scaling factor might happen. Such a mismatch can result in decreased detection performance, which is undesired. The determination of the scaling factor, including its relation to other steps of the method, are clarified. Specific attention is given to incorrect interchanging of the linear law and square law detectors, possible effects are also shown.

How the probability of false alarm, and thus also the scaling factor, are calculated is strongly dependent on the assumed background interference distribution. This distribution determines a large part of the threshold. However, no distribution can give an accurate representation of a realistic living room setting. Therefore other computations which don't rely that heavily on the assumed interference distribution, might provide better scaling factors that result in an increased detection performance. Developing a new method to calculate the scaling factor, dependent on other factors than in the original CFAR method, will take a lot of work but can result in better point clouds. It is suggested to look into different ways of including the background interference in the scaling factor determination.

From the generated point clouds it has also become clear that the shape of the object of detection cannot always be easily derived. Including additional information in the point cloud be the proposed post-processing step may in some cases improve the point cloud. However it does not always provide a better picture of the actual situation. Setting a threshold is perhaps not the best method when more information on the object is preferred. Instead of using CFAR detection methods, it is suggested for further research to focus on alternative ways to determine presence and absence. Starting from the signal strength information computed over the different dimensions, a possibility is to look into the shapes of those signal figures and recognizing patterns over the frames.

An implementation has been developed and tested for both simulations and acquired mmWave radar data. The range and velocity are retrieved according to standard Fourier transform procedures. For determining the angle or arrival, there are multiple methods that can be considered. The angular resolution is highly dependent on the amount of antennas on the sensor, but the choice of angle detection method also has influence on this. The MVDR method was chosen for this implementation, because it has the highest angular resolution of the angle detection methods with lower complexity.

The method computes the angle of arrival over one angular dimension at a time. An extension to compute both azimuth and elevation angles at the same time has not yet been provided. However, the method is adjusted according to the steps of other two-dimensional angle detection methods and included in this implementation. Although the MVDR method is characterized as having low complexity and thus lower computational costs compared to other angle detection methods, the computational costs increase quadratically for the extension to two angle dimensions at the same time.

Other angle detection methods were not implemented in this thesis, however it is suggested to also look in the effect different angle detection methods. Improving this part of the signal processing may beneficially influence the eventual generated point clouds. More accurate information can result in more accurate detection. Additionally, the angular detection can also be improved by using different mmWave sensors. Having an array of two receiver antennas is the bare minimum to be able to detect the angle of arrival. The accuracy of detection and resolution increase when more receiver antennas are aligned. When the amount of antennas cannot be increased due to limited costs or physical limitations for the sensor or device, virtual antennas can also be included. This results in increased angular resolution, but comes at the cost of higher computational complexity.

Furthermore, an experiment has been developed and conducted for realistic living rooms, to demonstrate and compare the performance of different interference level estimators for the CFAR detection method. Living room situations are not similar to ordinary experimental environments in the radar research field, such as military or automotive situations. Therefore it is not surprising that the performance of the different interference estimators does not match the performance for these other situations, which was the exact reason to look into this new situation. The estimators CA- and GOCA-CFAR perform better over other estimators SOCA- and OS-CFAR, although the performance is still not at a desired level. However, the performance of these estimators over the same data may vary when different signal processing steps are implemented.

The data acquired in this research is limited. It is advised to gather data on multi-scale level in order to get a comprehensive reliable radar data set. Such a large amount of data would be useful in order to train the point cloud generator which points are of interest and which are not, instead of focusing on using a threshold. A possibility is to label signals belonging to furniture like wardrobes and couches, which can then be viewed as clutter and ignored during the rest of the detection process. However, it is dependent on the eventual application whether these objects are also of interest and thus should be included in the point cloud.

References

[1] MD Abouzahra and RK Avent. "The 100-kW millimeter-wave radar at the Kwajalein Atoll". In: *IEEE Antennas and Propagation Magazine* 36.2 (1994), pp. 7–19.

[2] Muhammad Arsalan, Avik Santra, and Christoph Will. "Improved contactless heartbeat estimation in FMCW radar via Kalman filter tracking". In: *IEEE Sensors Letters* 4.5 (2020), pp. 1–4.

[3] Kshitiz Bansal et al. "Pointillism: Accurate 3d bounding box estimation with multi-radars". In: *Proceedings of the 18th Conference on Embedded Networked Sensor Systems*. 2020, pp. 340–353.

[4] Amalia E Barrios. "Considerations in the development of the advanced propagation model (APM) for US Navy applications". In: *2003 Proceedings of the International Conference on Radar (IEEE Cat. No. 03EX695)*. IEEE. 2003, pp. 77–82.

[5] R Bassem. *Radarsystems analysis and Design using MATLAB*. 2000.

[6] Stephen Blake. "OS-CFAR theory for multiple targets and nonuniform clutter". In: *IEEE transactions on aerospace and electronic systems* 24.6 (1988), pp. 785–790.

[7] Van Boeijen. *Plattegrond, Assen*.

[8] Mahdi Chamseddine et al. "Ghost target detection in 3d radar data using point cloud based deep neural network". In: *2020 25th International Conference on Pattern Recognition (ICPR)*. IEEE. 2021, pp. 10398–10403.

[9] Xingyu Chen et al. "MetaWave: Attacking mmWave Sensing with Meta-material-enhanced Tags". In: *The 30th Network and Distributed System Security (NDSS) Symposium*. Vol. 2023. 2023.

[10] Yuwei Cheng et al. "A novel radar point cloud generation method for robot environment perception". In: *IEEE Transactions on Robotics* 38.6 (2022), pp. 3754–3773.

[11] C.Q. Cutshaw and L.S. Ness. *Jane's Ammunition Handbook: 2003-2004*. Jane's Ammunition Handbook. Jane's Information Group, 2003. ISBN: 9780710625380.

[12] Xiaobo Deng, Chao Gao, and Jian Yang. "Sea Clutter Amplitude Statistics Analysis by Goodness-of-Fit Test". In: *Procedia Engineering* 29 (2012), pp. 791–796.

[13] Nedap Healthcare internal document. *Possible applications mmWave monitoring*. 2023.

[14] Shichen Dong. *Human Activity Recognition System Based on Millimeter Wave Radar*. 2020.

[15] Mohamed B El Mashade. "Analysis of Cell-Averaging based detectors for x 2 fluctuating targets in multitarget environments". In: *Journal of Electronics (China)* 23 (2006), pp. 853–863.

[16] Mohamed B El Mashade. "Performance analysis of the modified versions of CFAR detectors in multiple-target and nonuniform clutter". In: *Radioelectronics and Communications Systems* 56.8 (2013), pp. 385–401.

[17] Jonah Gamba. *Radar signal processing for autonomous driving*. Vol. 1456. Springer, 2020.

[18] Ennio Gambi et al. "Millimeter wave radar data of people walking". In: *Data in brief* 31 (2020), p. 105996.

[19] Prashant P Gandhi and Saleem A Kassam. "Adaptive order statistic and trimmed mean CFAR radar detectors". In: *Fourth IEEE Region 10 International Conference TENCON*. IEEE. 1989, pp. 832–835.

[20] Xin Gao et al. "On the MUSIC-derived approaches of angle estimation for bistatic MIMO radar". In: *2009 International Conference on Wireless Networks and Information Systems*. IEEE. 2009, pp. 343–346.

[21] Edno Gentilho Jr, Paulo Rogerio Scalassara, and Taufik Abrão. "Direction-of-arrival estimation methods: A performance-complexity tradeoff perspective". In: *Journal of Signal Processing Systems* 92.2 (2020), pp. 239–256.

[22] Lal Chand Godara. *Smart antennas*. CRC press, 2004.

[23] Junfeng Guan et al. "Through fog high-resolution imaging using millimeter wave radar". In: *Proceedings of the IEEE/CVF Conference on Computer Vision and Pattern Recognition*. 2020, pp. 11464–11473.

[24] Francesco Guidi et al. "Environment mapping with millimeter-wave massive arrays: System design and performance". In: *2016 IEEE Globecom Workshops (GC Wkshps)*. IEEE. 2016, pp. 1–6.

[25] V Gregers Hansen and James H Sawyers. "Detectability loss due to" greatest of" selection in a cell-averaging CFAR". In: *IEEE Transactions on Aerospace and Electronic Systems* 1 (1980), pp. 115–118.

[26] Ghufran M Hatem, JW Abdul Sadah, and Thamir R Saeed. "Comparative study of various cfar algorithms for non-homogenous environments". In: *IOP Conference Series: Materials Science and Engineering*. Vol. 433. 1. IOP Publishing. 2018, p. 012080.

[27] S. Haykin. *Adaptative Filter Theory*. 3rd ed. Prentice Hall, New York, 1996.

[28] Xu Huang, Joseph KP Tsoi, and Nitish Patel. "mmWave Radar Sensors Fusion for Indoor Object Detection and Tracking". In: *Electronics* 11.14 (2022), p. 2209.
[29] Eugin Hyun and Jong-Hun Lee. "A new OS-CFAR detector design". In: *2011 First ACIS/JNU International Conference on Computers, Networks, Systems and Industrial Engineering*. IEEE. 2011, pp. 133–136.
[30] Infineon. "BGT60TR13C 60 GHz Radar Sensor Datasheet V2.4.6". In: (2021).
[31] Welzijn en Sport Inspectie Gezondheidszorg en Jeugd Ministerie van Volksgezondheid. *Zorg, jeugdhulp en toezicht in tijden van personeelstekorten*. December 2022.
[32] Cesar Iovescu and Sandeep Rao. "The fundamentals of millimeter wave sensors". In: *Texas Instruments* (2017), pp. 1–8.
[33] Dejan Ivković, Milenko Andrić, and Bojan Zrnić. "A new model of CFAR detector". In: *Frequenz* 68.3-4 (2014), pp. 125–136.
[34] Mengjie Jiang et al. "4D High-resolution imagery of point clouds for automotive MmWave radar". In: *IEEE Transactions on Intelligent Transportation Systems* (2023).
[35] Xinrui Jiang et al. "Millimeter-wave array radar-based human gait recognition using multi-channel three-dimensional convolutional neural network". In: *Sensors* 20.19 (2020), p. 5466.
[36] Willie D Jones. "Keeping cars from crashing". In: *IEEE spectrum* 38.9 (2001), pp. 40–45.
[37] Eyung W Kang. *Radar system analysis, design, and simulation*. Artech House, 2008.
[38] Steven M Kay. *Modern spectral estimation*. Pearson Education India, 1988.
[39] Matthias Kronauge and Hermann Rohling. "Fast two-dimensional CFAR procedure". In: *IEEE Transactions on Aerospace and Electronic Systems* 49.3 (2013), pp. 1817–1823.
[40] Vincent Y. F. Li and Keith M. Miller. "Target Detection in Radar: Current Status and Future Possibilities". In: *The Journal of Navigation* 50.2 (1997), pp. 303–313.
[41] Xinrong Li et al. "Signal processing for TDM MIMO FMCW millimeter-wave radar sensors". In: *IEEE Access* 9 (2021), pp. 167959–167971.
[42] Teck-Yian Lim et al. "Radar and camera early fusion for vehicle detection in advanced driver assistance systems". In: *Machine learning for autonomous driving workshop at the 33rd conference on neural information processing systems*. Vol. 2. 7. 2019.
[43] Gui-Ru Liu et al. "A radar-based door open warning technology for vehicle active safety". In: *2016 International Conference on Information System and Artificial Intelligence (ISAI)*. IEEE. 2016, pp. 479–484.
[44] Hui Liu. *Robot systems for rail transit applications*. Elsevier, 2020.
[45] Yawei Liu and Zhiqiang Li. "Clutter Simulation Overview". In: *2017 2nd International Conference on Materials Science, Machinery and Energy Engineering (MSMEE 2017)*. Atlantis Press. 2017, pp. 530–534.
[46] Harry D Mafukidze et al. "Scattering centers to point clouds: a review of mmWave radars for non-radar-engineers". In: *IEEE Access* (2022).
[47] Bassem R Mahafza. *Radar systems analysis and design using MATLAB*. CRC press, 2022.
[48] Laurence Mailaender et al. *Advances in angle-of-arrival and multidimensional signal processing for localization and communications*. 2011.
[49] Asem Melebari, Amit Kumar Mishra, and MY Abdul Gaffar. "Comparison of square law, linear and bessel detectors for CA and OS CFAR algorithms". In: *2015 IEEE Radar Conference*. IEEE. 2015, pp. 383–388.
[50] WL Melvin and JA Scheer, eds. *Principles of Modern Radar, Vol. III: Radar Applications*. SciTech Publishing, 2014.
[51] Jerzy Neyman and Egon Sharpe Pearson. "IX. On the problem of the most efficient tests of statistical hypotheses". In: *Philosophical Transactions of the Royal Society of London. Series A, Containing Papers of a Mathematical or Physical Character* 231.694-706 (1933), pp. 289–337.
[52] Minh Q Nguyen and Changzhi Li. "Radar and ultrasound hybrid system for human computer interaction". In: *2018 IEEE Radar Conference (RadarConf18)*. IEEE. 2018, pp. 1476–1480.
[53] Ross D. Olney et al. "COLLISION WARNING SYSTEM TECHNOLOGY". In: 1995.
[54] Sameera Palipana et al. "Pantomime: Mid-air gesture recognition with sparse millimeter-wave radar point clouds". In: *Proceedings of the ACM on Interactive, Mobile, Wearable and Ubiquitous Technologies* 5.1 (2021), pp. 1–27.
[55] Zhengyu Peng. "MmWave CFAR object detection: Unclear use of scaling factor". E-mail conversation regarding the radarsimpy code.

[56] Zhengyu Peng et al. “A portable FMCW interferometry radar with programmable low-IF architecture for localization, ISAR imaging, and vital sign tracking”. In: *IEEE transactions on microwave theory and techniques* 65.4 (2016), pp. 1334–1344.
[57] Akarsh Prabhakara et al. “High Resolution Point Clouds from mmWave Radar”. In: *2023 IEEE International Conference on Robotics and Automation (ICRA)*. IEEE. 2023, pp. 4135–4142.
[58] Farra Anindya Putri et al. “Development of FMCW Radar Signal Processing for High-Speed Railway Collision Avoidance”. In: *Jurnal Elektronika dan Telekomunikasi* 22.1 (2022), pp. 40–47.
[59] R.Nowak. *Statistical Signal Processing, Detection Theory*. 2010.
[60] RS Raghavan. “Analysis of CA-CFAR processors for linear-law detection”. In: *IEEE Transactions on Aerospace and Electronic Systems* 28.3 (1992), pp. 661–665.
[61] Narasimhan Raman Subramanyan and Ramakrishnan Kalpathi R. “Robust variability index CFAR for non-homogeneous background”. In: *IET Radar, Sonar & Navigation* 13.10 (2019), pp. 1775–1786.
[62] Karthik Ramasubramanian and T Instruments. “Using a complex-baseband architecture in FMCW radar systems”. In: *Texas Instruments* 19 (2017).
[63] Mark A Richards et al. *Principles of modern radar*. Citeseer, 2010.
[64] Mark A. Richards. *Fundamentals of Radar Signal Processing, 1st ed.* McGraw-Hill, 2005.
[65] James A Ritcey. “Performance analysis of the censored mean-level detector”. In: *IEEE Transactions on Aerospace and Electronic Systems* 4 (1986), pp. 443–454.
[66] Hermann Rohling. “Radar CFAR thresholding in clutter and multiple target situations”. In: *IEEE transactions on aerospace and electronic systems* 4 (1983), pp. 608–621.
[67] Richard Roy and Thomas Kailath. “ESPRIT-estimation of signal parameters via rotational invariance techniques”. In: *IEEE Transactions on acoustics, speech, and signal processing* 37.7 (1989), pp. 984–995.
[68] Mochammad Sahal et al. “Comparison of CFAR methods on multiple targets in sea clutter using SPX-radar-simulator”. In: *2020 International Seminar on Intelligent Technology and Its Applications (ISITIA)*. IEEE. 2020, pp. 260–265.
[69] Shuji Sayama and Seishiro Ishii. “Suppression of Log-Normal Distributed Weather Clutter Observed by an S-Band Radar”. In: (2013).
[70] Ralph Schmidt. “Multiple emitter location and signal parameter estimation”. In: *IEEE transactions on antennas and propagation* 34.3 (1986), pp. 276–280.
[71] Merrill Ivan Skolnik. *Introduction to radar systems*. 1980.
[72] S Tokoro et al. “Electronically scanned millimeter-wave radar for pre-crash safety and adaptive cruise control system”. In: *IEEE IV2003 Intelligent Vehicles Symposium. Proceedings (Cat. No. 03TH8683)*. IEEE. 2003, pp. 304–309.
[73] E Udo, Agwu Amaechi, and Ogobuchi Okey. *Analysis and Computer Simulation of a Continuous Wave Radar Detection System for Moving Targets*. Vol. 5. 2021.
[74] Barry D Van Veen and Kevin M Buckley. “Beamforming: A versatile approach to spatial filtering”. In: *IEEE assp magazine* 5.2 (1988), pp. 4–24.
[75] NY Verona. “M 2006 IEEE Radar Conference”. In: *Conference on Security Tec (CCST)*. Vol. 16. 2006, p. 19.
[76] Fang Wang et al. “Quantitative gait measurement with pulse-Doppler radar for passive in-home gait assessment”. In: *IEEE Transactions on Biomedical Engineering* 61.9 (2014), pp. 2434–2443.
[77] Yuheng Wang et al. “m-activity: Accurate and real-time human activity recognition via millimeter wave radar”. In: *ICASSP 2021-2021 IEEE International Conference on Acoustics, Speech and Signal Processing (ICASSP)*. IEEE. 2021, pp. 8298–8302.
[78] Yunneng Yuan et al. “Two-dimensional FFT and two-dimensional CA-CFAR based on ZYNQ”. In: *The Journal of Engineering* 2019.20 (2019), pp. 6483–6486.
[79] Xuezhi Zeng, Halldór Stefán Laxdal Báruson, and Alexander Sundvall. “Walking Step Monitoring with a Millimeter-Wave Radar in Real-Life Environment for Disease and Fall Prevention for the Elderly”. In: *Sensors* 22.24 (2022), p. 9901.
[80] Youwei Zeng et al. “FarSense: Pushing the range limit of WiFi-based respiration sensing with CSI ratio of two antennas”. In: *Proceedings of the ACM on Interactive, Mobile, Wearable and Ubiquitous Technologies* 3.3 (2019), pp. 1–26.
[81] Guangcheng Zhang, Xiaoyi Geng, and Yueh-Jaw Lin. “Comprehensive mpoint: A method for 3d point cloud generation of human bodies utilizing fmcw mimo mm-wave radar”. In: *Sensors* 21.19 (2021), p. 6455.
[82] Peijun Zhao et al. “CubeLearn: End-to-end learning for human motion recognition from raw mmWave radar signals”. In: *IEEE Internet of Things Journal* (2023).

[83] Peijun Zhao et al. “mid: Tracking and identifying people with millimeter wave radar”. In: *2019 15th International Conference on Distributed Computing in Sensor Systems (DCOSS)*. IEEE. 2019, pp. 33–40.

[84] Qiangwen Zheng et al. “An improved scheme for high-resolution point cloud map generation based on FMCW radar”. In: *2020 IEEE 11th Sensor Array and Multichannel Signal Processing Workshop (SAM)*. IEEE. 2020, pp. 1–5.

[85] Wei Zhou et al. “Modified cell averaging CFAR detector based on Grubbs criterion in non-homogeneous background”. In: *IET Radar, Sonar & Navigation* 13.1 (2019), pp. 104–112.

A Supplementary Figures

A.1 Signal Strength Polar Plots

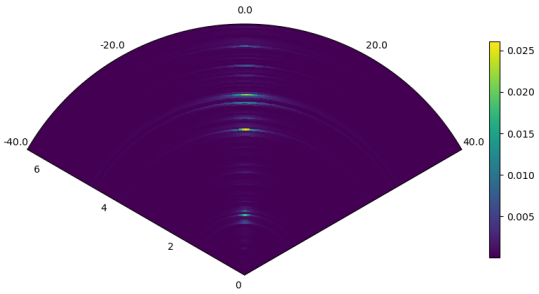

(a) Range-azimuth, no presence

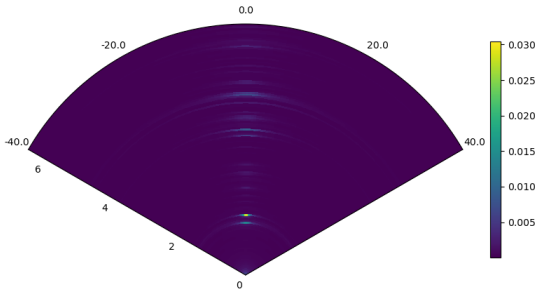

(b) Range-elevation, no presence

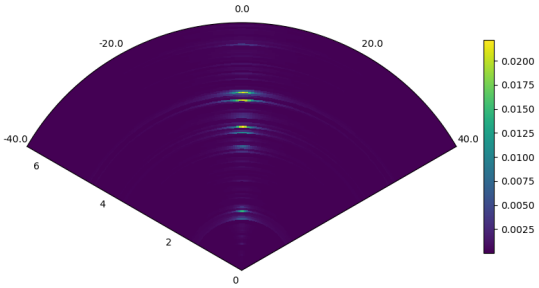

(c) Range-azimuth, one person

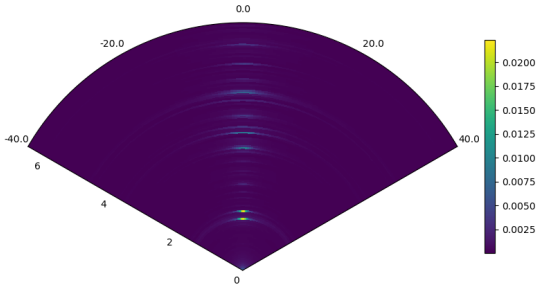

(d) Range-elevation, one person

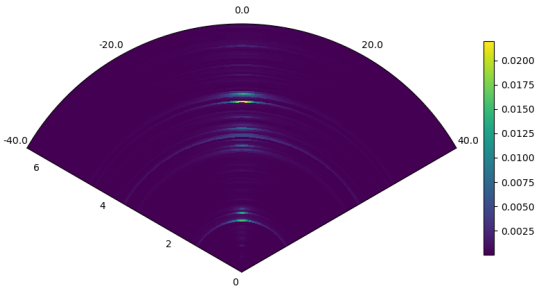

(e) Range-azimuth, 2 people

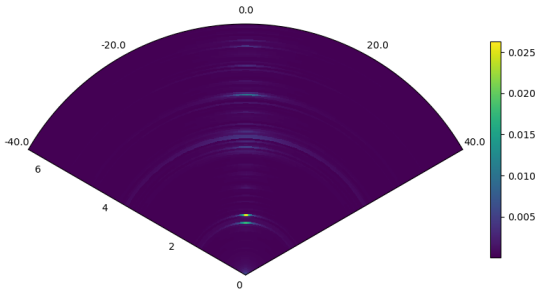

(f) Range-elevation, 2 people

Figure 42: Range-angle plot, empty interior and almost no strong-reflecting materials in the room.

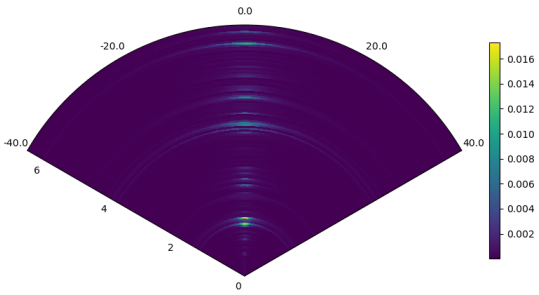

(a) Range-azimuth, no presence

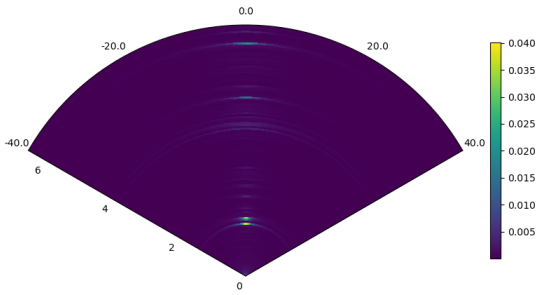

(b) Range-elevation, no presence

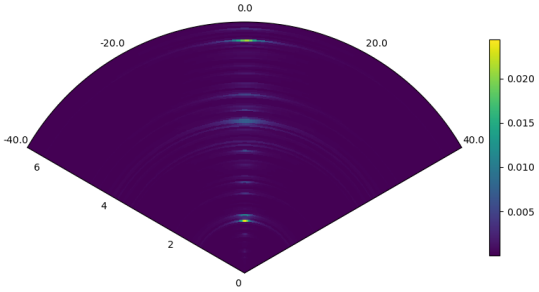

(c) Range-azimuth, one person

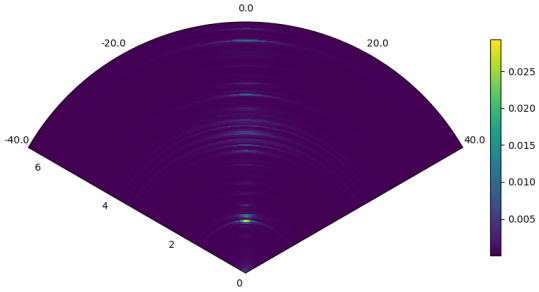

(d) Range-elevation, one person

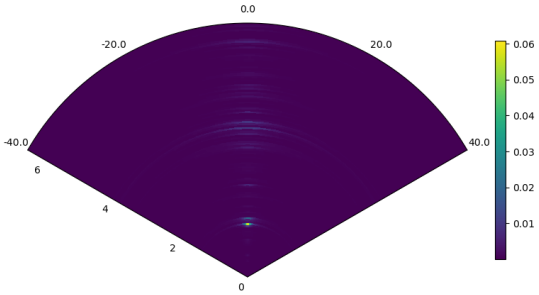

(e) Range-azimuth, 2 people

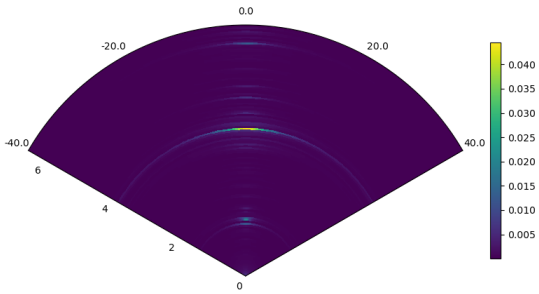

(f) Range-elevation, 2 people

Figure 43: Range-angle plots, empty interior and almost no strong-reflecting materials in the room.

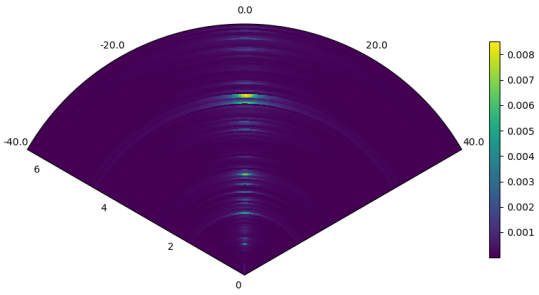

(a) Range-azimuth, no presence

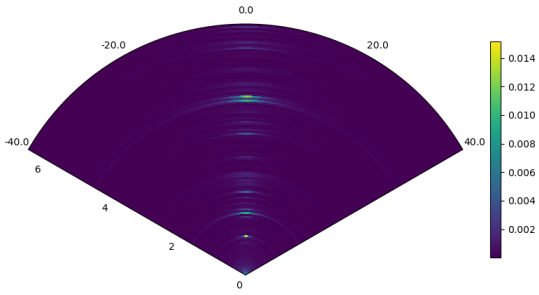

(b) Range-elevation, no presence

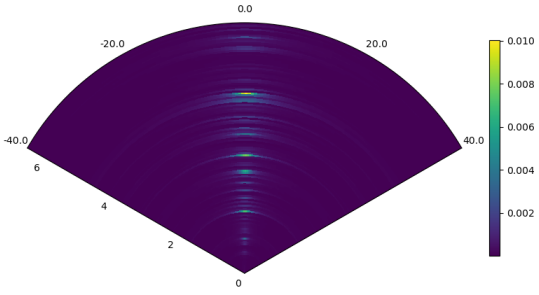

(c) Range-azimuth, one person

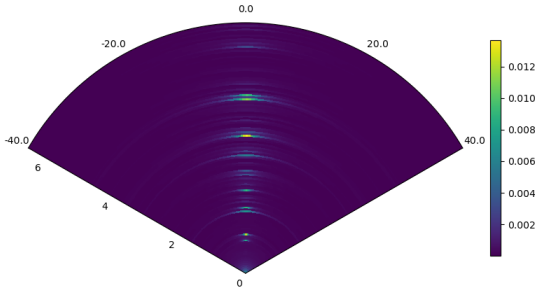

(d) Range-elevation, one person

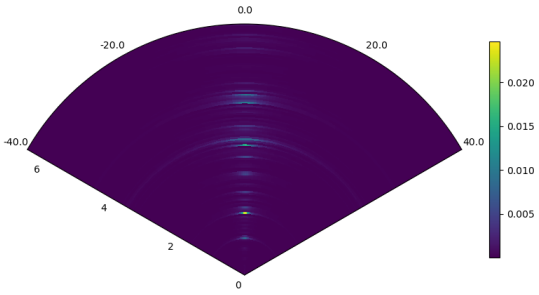

(e) Range-azimuth, 2 people

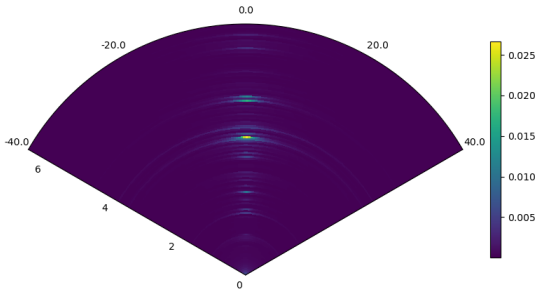

(f) Range-elevation, 2 people

Figure 44: Range-angle plots, empty interior and almost no strong-reflecting materials in the room.

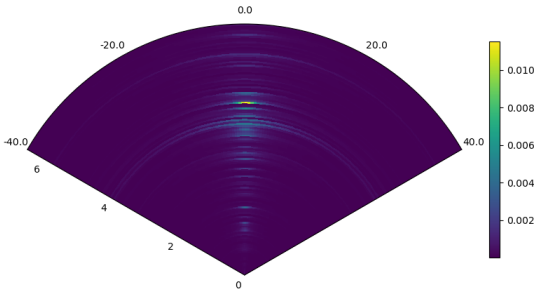

(a) Range-azimuth, no presence

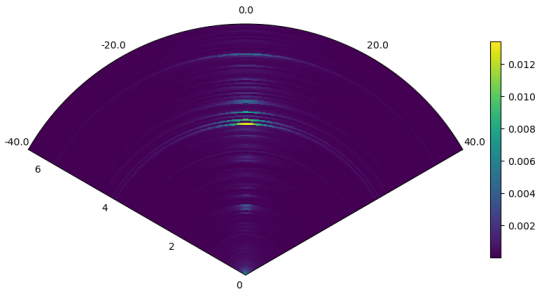

(b) Range-elevation, no presence

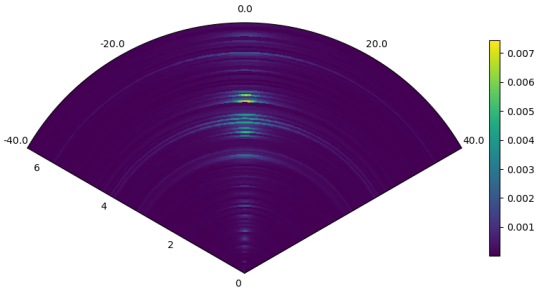

(c) Range-azimuth, one person

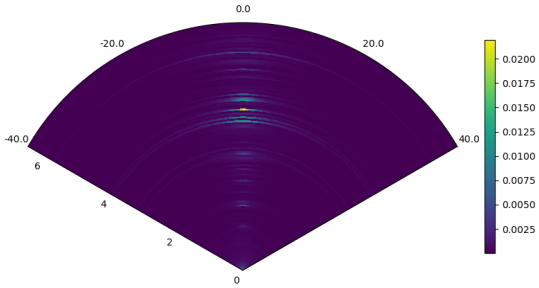

(d) Range-elevation, one person

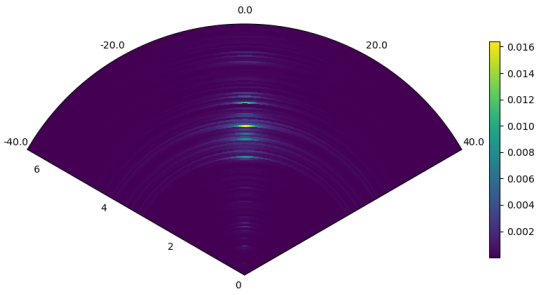

(e) Range-azimuth, 2 people

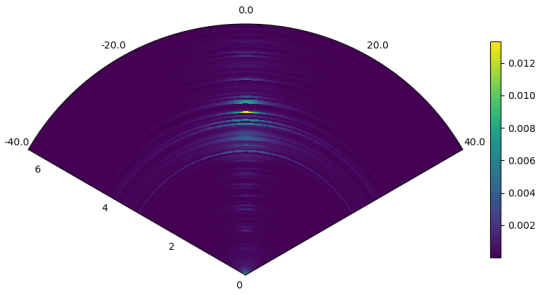

(f) Range-elevation, 2 people

Figure 45: Range-angle plots, full interior and a lot of strong reflecting materials in the room.

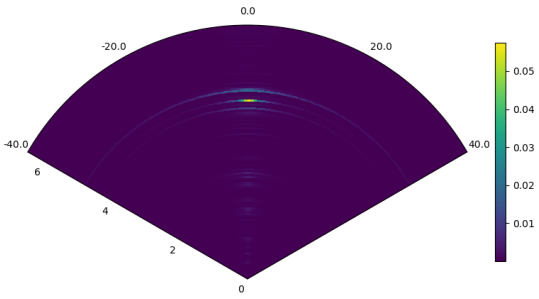

(a) Range-azimuth, no presence

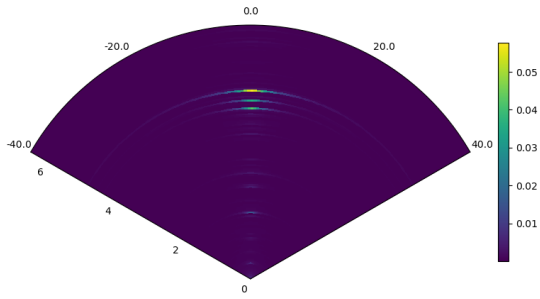

(b) Range-elevation, no presence

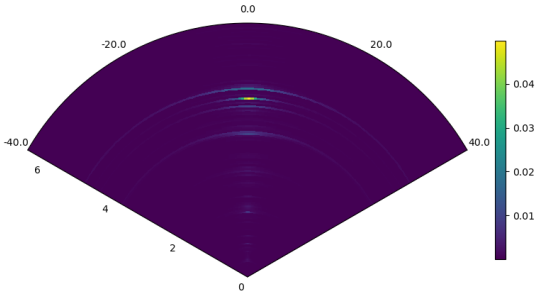

(c) Range-azimuth, one person

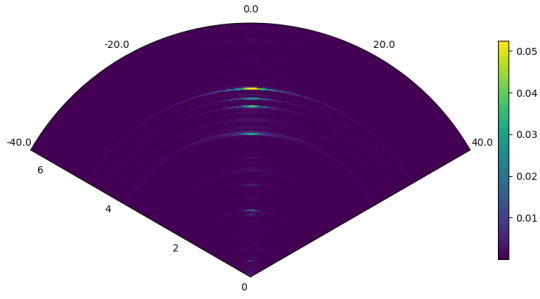

(d) Range-elevation, one person

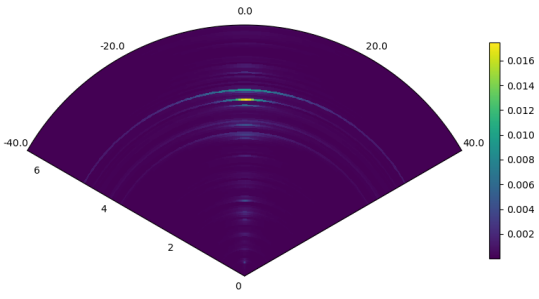

(e) Range-azimuth, 2 people

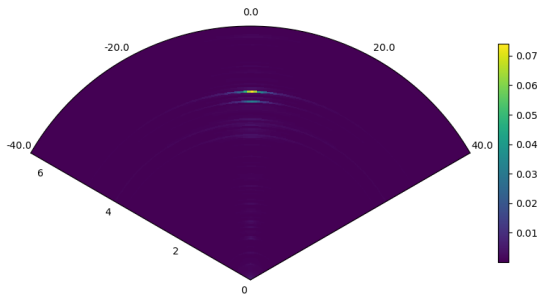

(f) Range-elevation, 2 people

Figure 46: Range-angle plots, full interior and an average amount of strong-reflecting materials in the room.

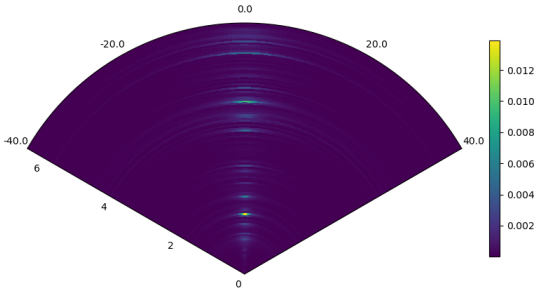

(a) Range-azimuth, no presence

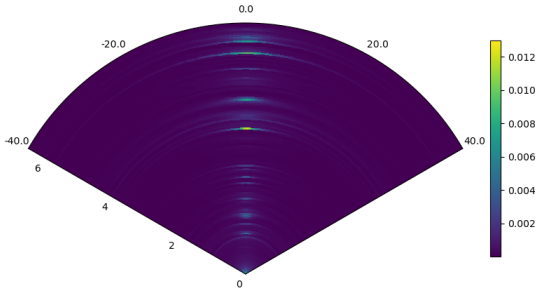

(b) Range-elevation, no presence

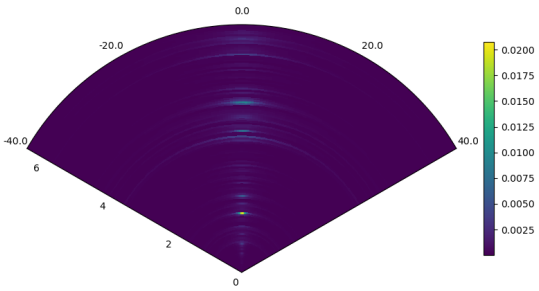

(c) Range-azimuth, one person

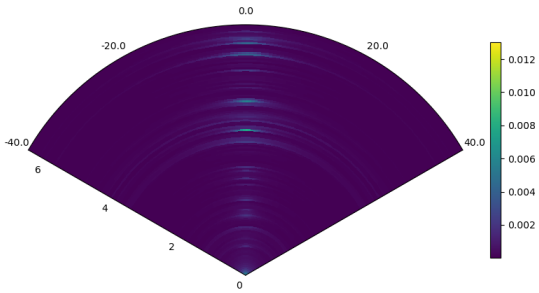

(d) Range-elevation, one person

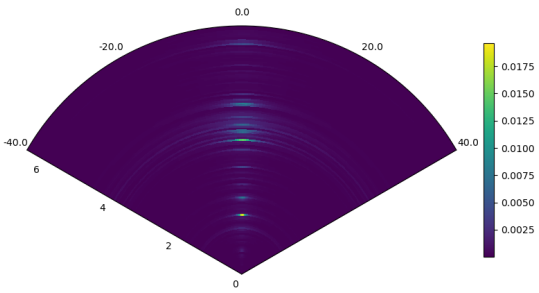

(e) Range-azimuth, 2 people

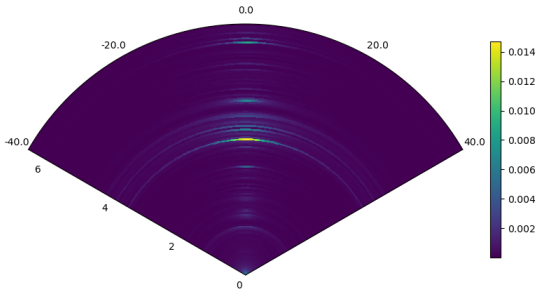

(f) Range-elevation, 2 people

Figure 47: Range-angle plots, average coverage of interior and a lot of strong-reflecting materials in the room.

A.2 3D Point Clouds

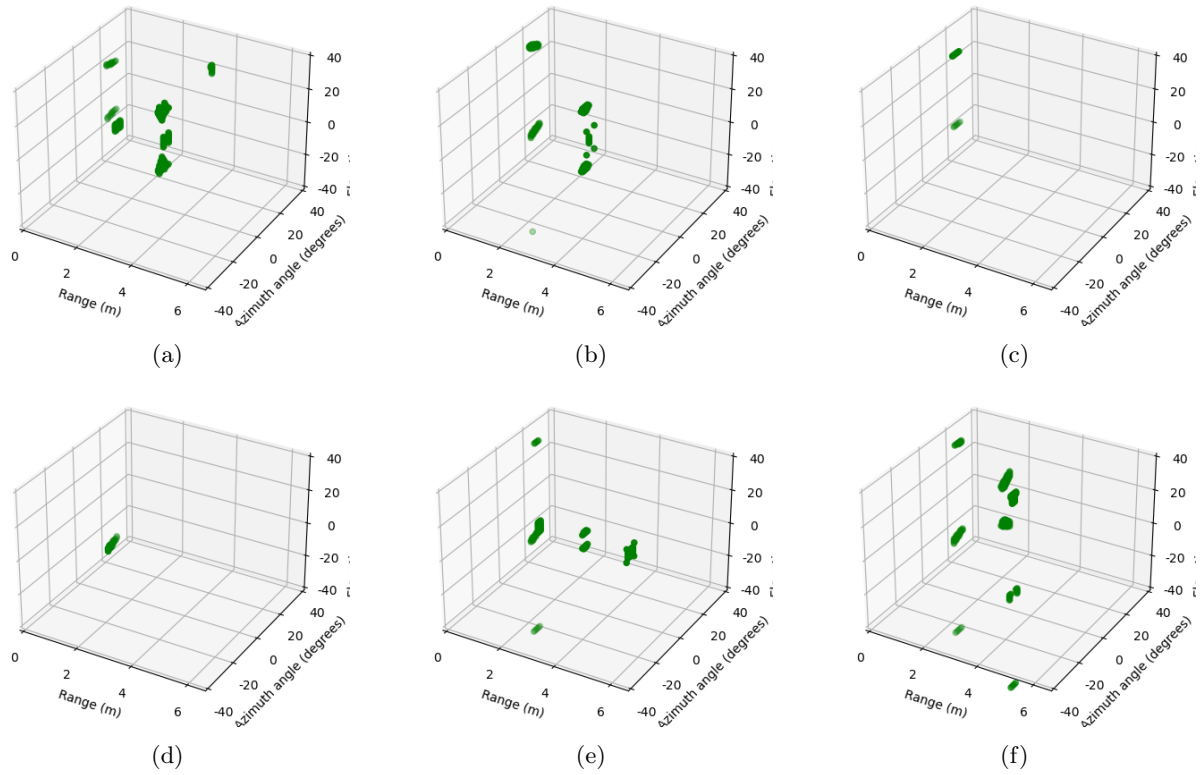

Figure 48: Point clouds for CA-CFAR for six consecutive frames. One person present, small scale hand movement, empty interior and almost no strong-reflecting materials.

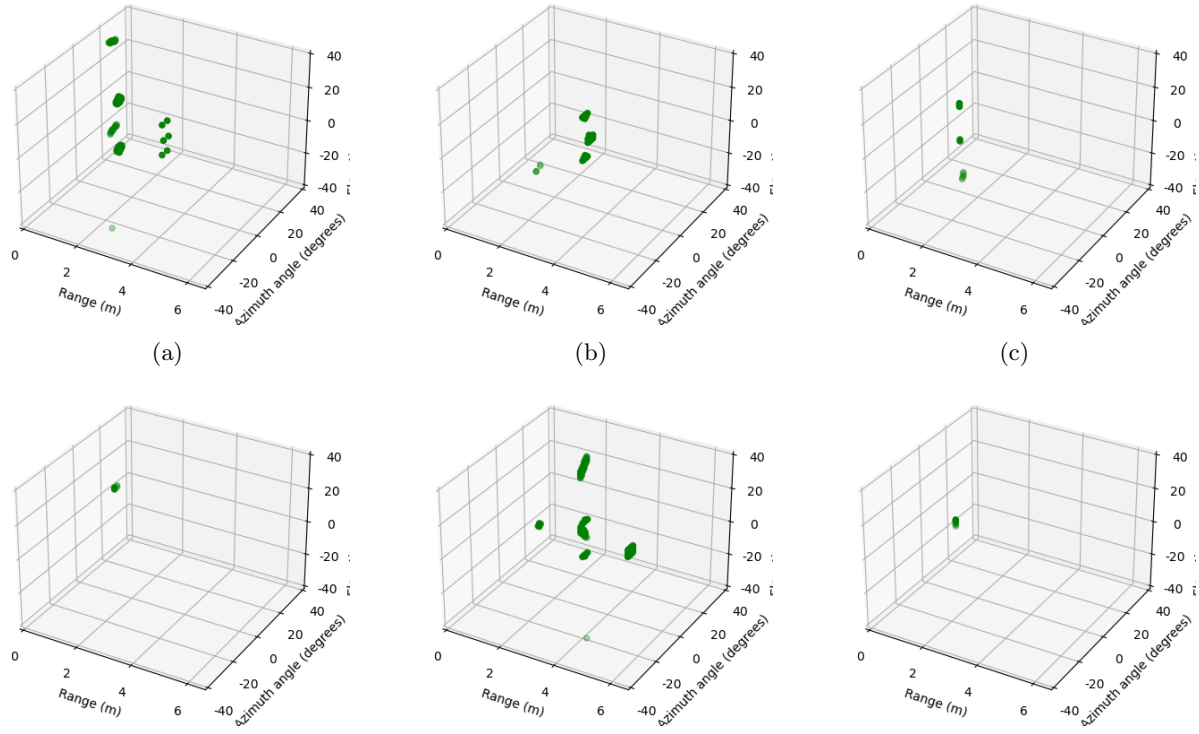

Figure 49: Point clouds for GOCA-CFAR for six consecutive frames. One person present, small scale hand movement, empty interior and almost no strong-reflecting materials.

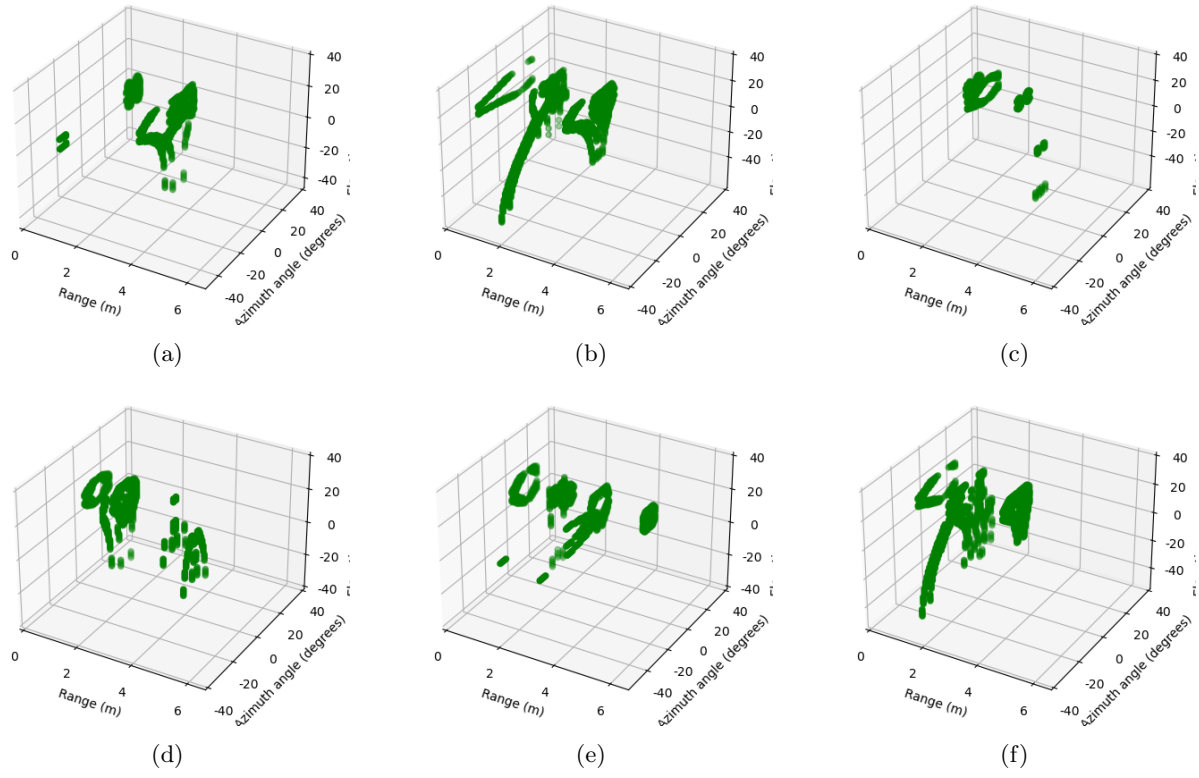

Figure 50: Point clouds for SOCA-CFAR for six consecutive frames. One person present, small scale hand movement, empty interior and almost no strong-reflecting materials.

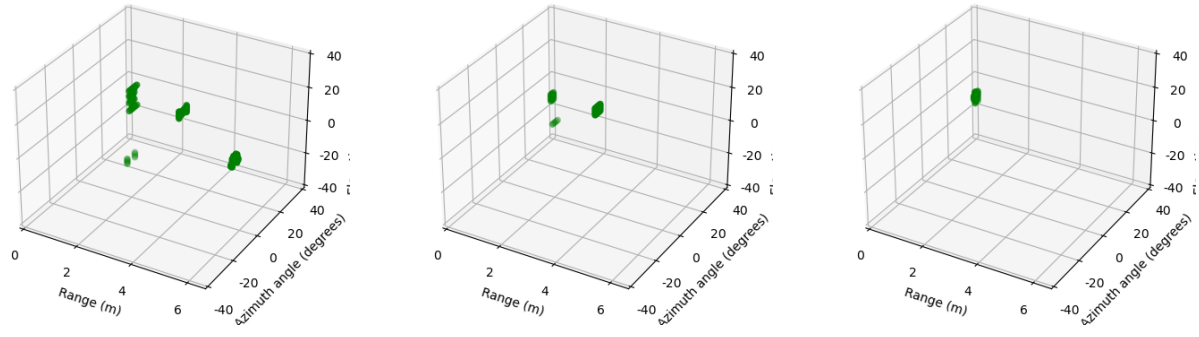

(a) (b) (c)

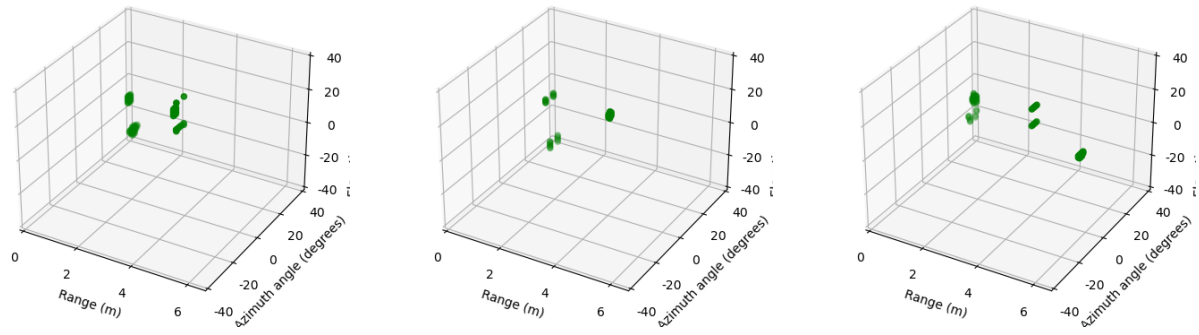

(d) (e) (f)

Figure 51: Point clouds for CA-CFAR for six consecutive frames. Two people present, small scale arm and hand movement combined, empty interior and almost no strong-reflecting materials.

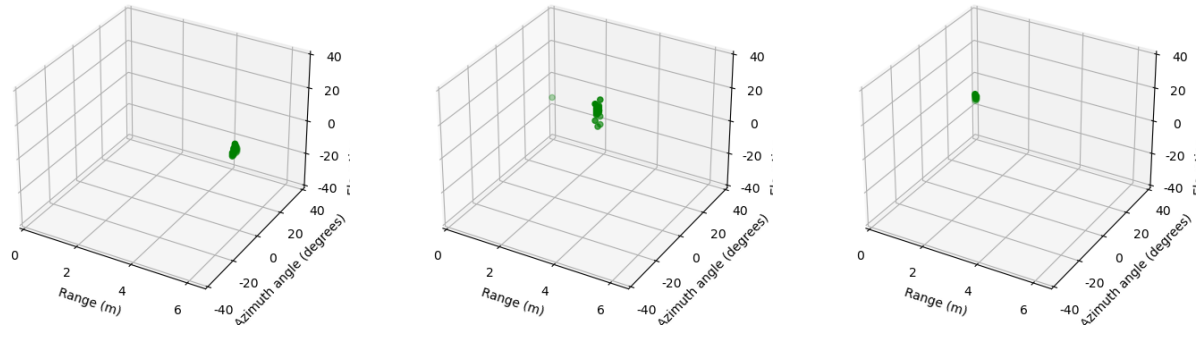

(a) (b) (c)

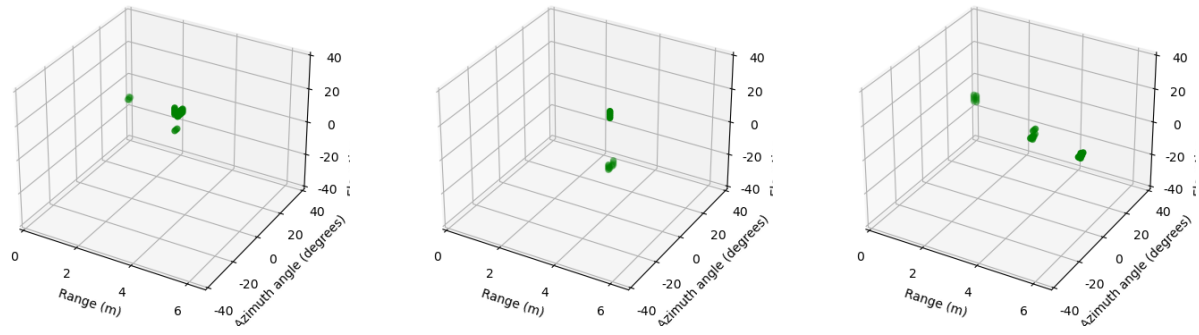

(d) (e) (f)

Figure 52: Point clouds for GOCA-CFAR for six consecutive frames. Two people present, small scale arm and hand movement combined, empty interior and almost no strong-reflecting materials.

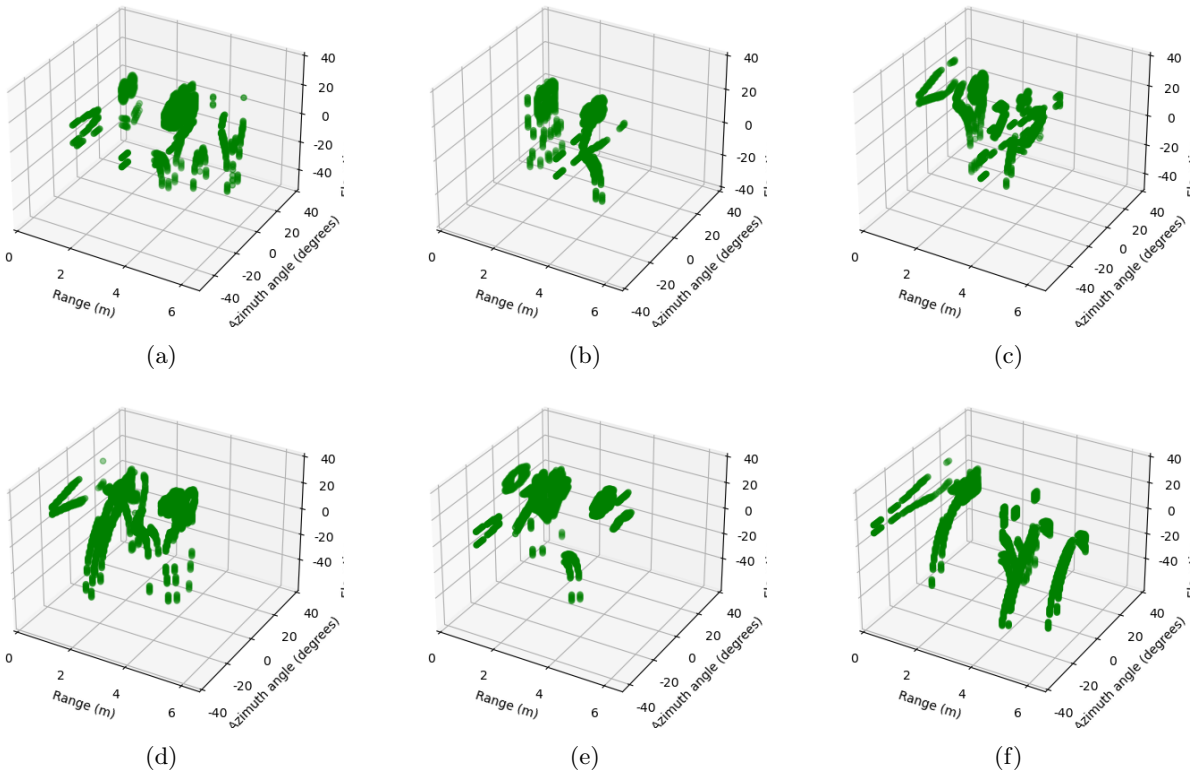

Figure 53: Point clouds for SOCA-CFAR for six consecutive frames. Two people present, small scale arm and hand movement combined, empty interior and almost no strong-reflecting materials.